A Microfluidic System for High-Precision Image-Based Live Cell Sorting Using Dielectrophoretic Forces

DISSERTATION

zur Erlangung des akademischen Grades

"doctor rerum naturalium"

(Dr. rer. nat.)

in der Wissenschaftsdisziplin Bioanalytik

eingereicht an der

Mathematisch-Naturwissenschaftlichen Fakultät

Institut für Biochemie und Biologie

der Universität Potsdam

angefertigt am

Fraunhofer-Institut für Zelltherapie und Immunologie (IZI)

Institutsteil Bioanalytik und Bioprozesse (IZI-BB), Potsdam

von

Marten Tobias Gerling

Potsdam, den 25. Oktober 2022

Ort und Tag der Disputation: Potsdam, 24. März 2023

Selbstständigkeitserklärung

Hiermit erkläre ich, dass ich die vorliegende Dissertation selbständig verfasst und keine anderen als die angegebenen Quellen und Hilfsmittel benutzt habe.

Ferner versichere ich, dass ich diese Dissertation noch an keiner anderen Universität eingereicht habe, um ein Promotionsverfahren zu eröffnen. Ich habe mich auch früher um keine Promotion bemüht.

Abstract

An important goal in biotechnology and (bio-) medical research is the isolation of single cells from a heterogeneous cell population. These specialised cells are of great interest for bioproduction, diagnostics, drug development, (cancer) therapy and research. To tackle emerging questions, an ever finer differentiation between target cells and non-target cells is required. This precise differentiation is a challenge for a growing number of available methods.

Since the physiological properties of the cells are closely linked to their morphology, it is beneficial to include their appearance in the sorting decision. For established methods, this represents a non addressable parameter, requiring new methods for the identification and isolation of target cells. Consequently, a variety of new flow-based methods have been developed and presented in recent years utilising 2D imaging data to identify target cells within a sample. As these methods aim for high throughput, the devices developed typically require highly complex fluid handling techniques, making them expensive while offering limited image quality.

In this work, a new continuous flow system for image-based cell sorting was developed that uses dielectrophoresis to precisely handle cells in a microchannel. Dielectrophoretic forces are exerted by inhomogeneous alternating electric fields on polarisable particles (here: cells). In the present system, the electric fields can be switched on and off precisely and quickly by a signal generator. In addition to the resulting simple and effective cell handling, the system is characterised by the outstanding quality of the image data generated and its compatibility with standard microscopes. These aspects result in low complexity, making it both affordable and user-friendly.

With the developed cell sorting system, cells could be sorted reliably and efficiently according to their cytosolic staining as well as morphological properties at different optical magnifications. The achieved purity of the target cell population was up to 95% and about 85% of the sorted cells could be recovered from the system. Good agreement was achieved between the results obtained and theoretical considerations. The achieved throughput of the system was up to 12,000 cells per hour. Cell viability studies indicated a high biocompatibility of the system.

The results presented demonstrate the potential of image-based cell sorting using dielectrophoresis. The outstanding image quality and highly precise yet gentle handling of the cells set the system apart from other technologies. This results in enormous potential for processing valuable and sensitive cell samples.

Zusammenfassung

Ein wichtiges Ziel in der Biotechnologie und (bio-) medizinischen Forschung ist die Isolation von Einzelzellen aus einer heterogenen Zellpopulation. Aufgrund ihrer besonderen Eigenschaften sind diese Zellen für die Bioproduktion, Diagnostik, Arzneimittelentwicklung, (Krebs-) Therapie und Forschung von großem Interesse. Um neue Fragestellungen angehen zu können, ist eine immer feinere Differenzierung zwischen Zielzellen und Nicht-Zielzellen erforderlich. Diese präzise Differenzierung stellt eine Herausforderung für eine wachsende Zahl verfügbarer Methoden dar.

Da die physiologischen Eigenschaften der Zellen eng mit ihrer Morphologie verknüpft sind, ist es sinnvoll ihr Erscheinungsbild mit in die Sortierentscheidung einzubeziehen. Für etablierte Methoden stellt dies jedoch einen nicht adressierbaren Parameter dar, weshalb neue Methoden zur Identifikation und Isolation der Zielzellen benötigt werden. Folglich wurde in den letzten Jahren eine Vielzahl neuer durchflussbasierter Methoden entwickelt und vorgestellt, die 2D-Bilddaten zur Identifikation der Zielzellen innerhalb einer Probe heranziehen. Da diese Methoden auf hohe Durchsätze abzielen, erfordern die entwickelten Geräte in der Regel hochkomplexe Techniken zur Handhabung der Flüssigkeiten, was sie teuer macht und gleichzeitig zu einer begrenzten Bildqualität führt.

In dieser Arbeit wurde ein neues durchflussbasiertes System zur bildbasierten Zellsortierung entwickelt, das Dielektrophorese zur präzisen Handhabung der Zellen in einem Mikrokanal verwendet. Dielektrophoretische Kräfte werden von inhomogenen elektrischen Wechselfeldern auf polarisierbare Partikel (hier: Zellen) ausgeübt. Bei dem vorliegenden System können die elektrischen Felder durch einen Signalgenerator präzise und schnell ein- und ausgeschaltet werden. Neben der daraus resultierenden einfachen und effektiven Handhabung der Zellen zeichnet sich das System durch die hervorragende Qualität der erzeugten Bilddaten und die Kompatibilität mit Standardmikroskopen aus. Diese Aspekte führen zu einer geringen Komplexität, die es sowohl erschwinglich als auch benutzerfreundlich macht.

Mit dem entwickelten System zur Zellsortierung konnten Zellen sowohl auf Basis einer zytosolischen Färbung als auch auf Basis morphologischer Eigenschaften bei verschiedenen optischen Vergrößerungen zuverlässig und effizient sortiert werden. Die erreichte Reinheit der Zielzellpopulation betrug bis zu 95% wobei etwa 85% der sortierten Zellen aus dem System zurückgewonnen werden konnten. Dabei wurde eine gute Übereinstimmung der ermittelten Ergebnisse mit theoretischen Überlegungen erreicht. Der erreichte Durchsatz des Systems betrug bis zu 12.000 Zellen pro Stunde. Untersuchungen der Zellvitalität deuteten darauf hin, dass das System eine hohe Biokompatibilität aufweist.

Die vorgestellten Ergebnisse demonstrieren das Potenzial der bildbasierten Zellsortierung mittels Dielektrophorese. Die herausragende Bildqualität und hochpräzise aber dennoch zellschonende Handhabung der Zellen grenzen das System von anderen Technologien ab. Daraus ergibt sich ein enormes Potenzial für die Verarbeitung wertvoller und sensibler Zellproben.

Table of contents

1 Introduction

Cells or groups of cells with specific properties are of great interest in biotechnology[1,2] and biomedical research[3–5]. A key requirement in these areas and beyond is the precise, cell-preserving and efficient isolation of cells or cell groups of interest from heterogeneous cell populations. In the field of bioproduction, for example, so-called over-producing cells are specifically desired in order to increase the biomeolecule yield[6,7]. In biofuel production, microalgae with high lipid contents are preferred[8]. For CAR-T cell therapy, T cells need to be isolated from patient blood in order to genetically modify them and return them to the patient later for treatment[9,10]. And in cancer research, circulating tumour cells (CTCs) or immune cells are extracted from liquid biopsies to serve diagnostic, prognostic and drug development purposes[11–16].

Classical approaches for cell separation such as filtration rely on simple cell properties like cell size. Although they are fast and efficient, they are also relatively nonspecific[17,18]. Advanced techniques such as Magnetic Activated Cell Sorting (MACS) select cells using magnetic nanoparticles that are directly bound to the target cells via antibodies[19–21]. The use of surface markers enables more specific cell differentiation, but still relies on a binary separation criterion (i.e., presence or absence of markers)[1]. Due to this poorly differentiated signal processing, cells with multiple markers are difficult to isolate[22,23].

An approach that enables the isolation of individual cells is Fluorescence Activated Cell Sorting (FACS[*]). Here, cells flow through a microchannel one by one and are sorted sequentially. Low-resolution sorting parameters such as scattered light integrated from the whole cell and multi-coloured fluorescence signals form the basis for the sorting decision in this method. These sorting parameters depend on the presence or absence of surface markers as well as the granularity and size of the respective cell. The combination of these parameters with sequential sorting allows the most precise isolation of target cells from a cell sample to date[24–26].

However, it was found that the physiological properties of different cell types are strongly linked to their morphology[27–33] which is an inaccessible parameter for conventional methods described above[34–40]. For example, a higher nucleus-to-cytoplasmic ratio was found in malignant cells[41]. Further examples are the mislocalisation of proteins within the cell in different diseases[42] or the biofuel production capabilities of microalgae in dependence of their lipid content associated to their vesicle size and shape[2,8].

Performing the sorting based on 2D imaging data is therefore advantageous for a more precise differentiation between cell populations. For this reason, new methods emerged in recent years that are capable of analysing and even isolating cells based on image-derived data. Focusing on high throughputs of up to several thousand cells per second, the majority of the current approaches are designed as flow through methods employing high flow velocities of $1\ \mathrm{m\ s^{-1}}$ and more[43–50].

The high flow velocity, in turn, creates enormous demands on image acquisition and data processing, as these have to be conducted within a few microseconds and are correspondingly

---

[*] FACS is a registered trademark of Becton Dickinson. However, it is widely used as a generic term in the field of cytometry and is therefore also used as such here.

technically challenging. Consequently, the systems involve elaborate imaging techniques, multi-stage high-precision flow control mechanisms and high-performance computer systems. As a result, the systems are highly complex, probably relatively expensive and difficult to operate, while still limited in the achievable image quality and depth of analysis[51]. Accordingly, there is a strong demand for simple and cost-effective systems that can be used on-site in any laboratory at any time and still deliver high-quality images and precise cell separation.

A possible approach towards the establishment of such a system are microchannel systems compatible with conventional microscopy equipment. By applying a low flow rate inside the microchannel, these systems could provide high-resolution images without motion blur at low complexity and low cost. In addition, a low flow rate would allow an extended period of time for data analysis, which would also drastically reduce the demands on computing capacity. However, for high cell throughput in such a system, a high cell density is necessary to compensate for the low flow rate. The resulting small distance between the individual cells consequently imposes high demands on the precision of the sorting mechanism to enable individual cell processing.

A promising technique for high-precision cell separation is dielectrophoresis-based cell manipulation. It relies on electric fields emanating from microelectrodes similar to the size of the cells to move cells in a carrier fluid. The technique is well established and, due to its small size, compatible with conventional microscopes, which increases the obtainable image quality and significantly reduces the complexity of the approach as intended[52–56].

In this work, a new low-cost and low-complexity dielectrophoresis-based microfluidic sorting method was developed, enabling cell sorting based on high-quality imaging in continuous flow at low process velocities. The setup is compatible with a standard inverted fluorescence microscope and operated using standard microfluidic and computing equipment.

The prototype was successfully used for colour- and image-based sorting of Jurkat cells based on images taken at up to 60x magnification with a high numerical aperture (NA). In addition to high purity, a high recovery rate was achieved, making the system interesting for working with small and valuable cell samples, such as those frequently encountered in organoid or stem cell research, the investigation of disease models or small tissue biopsies, where throughput is less important than the precise, reliable and gentle processing of small cell numbers with minimal cell loss[57].

Since sorted cell populations are further used in a variety of ways and need to be vital, i.e., undamaged[58,59], the cells sorted within the prototype were examined with regard to their vitality in order to exclude harmful influences by electric fields or fluidic shear stress.

2 Objective of this work

The main objective of this work was to develop a novel dielectrophoresis-based microfluidic continuous-flow system for high-quality image-based cell sorting at low flow rates. A key requirement for this system was its simplicity and compatibility with a standard inverted fluorescence microscope and standard microfluidic and computing equipment to reduce costs and thereby improve accessibility and availability.

The central element of the system was to be a new microfluidic dielectrophoresis-based chip, which was to be designed according to the above requirements and integrated into a fluidic periphery that was also to be constructed. In the course of developing the microchip, a series of preliminary experiments were to be carried out to verify the feasibility of the sorting principle and theoretical relationships such as the deflection efficiency of the electric fields as a function of the flow rate, electrode voltage and electrode arrangement. To enable these investigations, a rapid prototyping process was to be developed first to allow the flexible on-demand in-house production of microfluidic chips with individually required channel geometries and electrode structures.

In parallel to the design of the central microchip, the fluidic periphery was also to be developed. Here, both the (air) bubble-free filling and the stable continuous operation of the system with a constant flow rate over a long period of time needed to be achieved in order to reliably sort samples with large cell numbers needing a long processing time.

Subsequently, the flow behaviour of the cells in the system was to be investigated and characterised. In this course, the individual parts of the system and parameters such as the flow rate, electrode voltage and exposure time were to be optimised for cell sorting.

The next step was to develop a detailed protocol for cell sorting and determine the assembled systems colour-based sorting performance using stained cells of different colours. Additionally, the system's ability to sort cells based on spatial characteristics was to be demonstrated using cells with different staining patterns.

Finally, the vitality of the processed cells was to be examined in order to verify the biocompatibility of the approach.

3 Theoretical background and current state of research

Due to the need to isolate cells for a wide variety of applications, a vast field of different methods and techniques has developed over the years. These range from less complex and unspecific approaches to complex and expensive devices capable of performing detailed analyses. In the following, the technical and theoretical foundations relevant to this work are first explained, before individual methods and techniques relevant to the context of this work are discussed in more detail.

3.1 Isolation, separation and sorting

When it comes to the partitioning of objects in everyday language, the terms *isolation*, *separation* and *sorting* are often used interchangeably. In the context of this work, however, they are intended to describe different processes. Hence, the terms are defined below and then applied accordingly.

Isolation means "Extraction of an individual from a group" and should therefore be used as a generic term for the process in which objects (here: cells) are extracted from a collective (here: mixed population).

Separation describes a (biophysical) division of objects or groups of objects. For the separation of cells, methods such as filtration or inertial microfluidics (see section 3.2.3) are usually used. For these methods, no information processing is required and the configuration of the system does not change over time. For these reasons, *Separation* is a so-called *passive* process.

Sorting, finally, describes a targeted selection of objects and involves temporal changes to the system (for example, switching pumps or electric fields on and off). Since this requires the processing of information, *Sorting* is referred to as an *active* process. Various mechanisms are used in the sorting of cell populations, of which the most relevant are listed in section 3.5.3.

3.2 Microfluidic Flow

Almost all common cell separation and sorting techniques use microchannels of some kind through which the cells flow in a more or less orderly pattern. Since microchannels are also used in this work and special flow conditions prevail in them, these conditions are discussed below.

3.2.1 Types of Flow

In conventional macrochannels and pipes, as they are commonly known from everyday life, inertial forces dominate. Therefore, turbulent flow conditions usually prevail and turbulences in the flow are characteristic that randomly occur and disappear after a short time[60]. Due to this chaotic behaviour, particle trajectories cannot be predicted, making macro channels unsuitable for the targeted handling of objects[61].

In microchannels, on the other hand, a different flow behaviour prevails, as viscous forces predominate here, counteracting the formation of turbulence[62]. For this reason, a laminar flow occurs with no mixing of the individual layers of the fluid. Mass transport without external forces lateral to the direction of flow can therefore only take place by diffusion[63]. A schematic comparison of turbulent and laminar flow is shown in Figure 1.
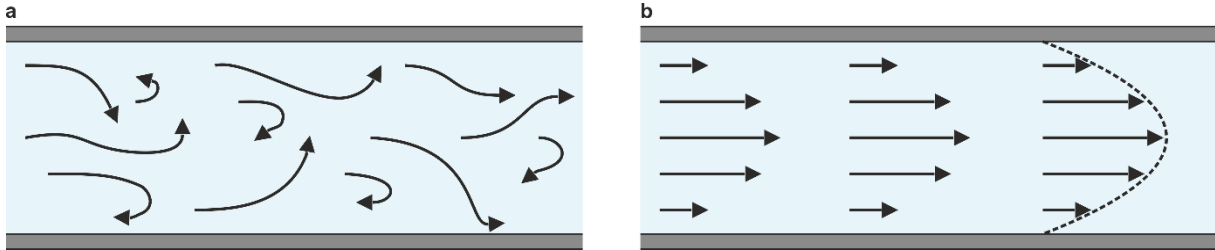
Figure 1: Types of flow. a, In macroscopic channels, turbulent flow with irregular turbulence usually occurs. This leads to mixing of the fluid. **b**, In microchannels, a laminar flow regime generally prevails. Here the fluid flows in an orderly pattern in layers that do not mix. Due to wall effects, a higher flow velocity prevails in the centre of the channel and a parabolic flow profile (dotted black line) develops.

A characteristic feature of laminar flow is the formation of a parabolic flow profile when a liquid is pumped through a microchannel by pressure[63]. This behaviour results from the adhesive forces between the fluid molecules and the channel wall as well as cohesive forces between the fluid molecules themselves. Near the channel wall, the attraction between the liquid molecules and the wall is greater than between the individual liquid molecules, i.e., adhesion is greater than cohesion. This causes a thin layer of fluid to form on the channel wall that does not move (no-slip condition). Consequently, most of the flow takes place in the centre of the channel (see Figure 1) and the parabolic flow profile is established[63,64].

The flow velocity as a function of the channel position $v(r)$ can be calculated for straight circular channels as follows:

$$v(r) = 2 * v_{av} * \left(1 - \frac{r^2}{R^2}\right)$$

(1)

Here v_{av} is the average flow velocity of the liquid in the channel which can be calculated from the volume flow and the cross-sectional area of the channel, R is the channel radius and r is the distance to the centre of the channel[65].

Straight rectangular channels with a high aspect ratio, as used in this work, represent a special case. For such channels, the flow profile can be calculated by

$$v(h) = 1.5 * v_{av} * \left(1 - \frac{h^2}{H^2}\right)$$

(2)

with v_{av} again beeing the average flow velocity, h the distance from the channel centre and H half of the channel height[66]. In the centre of the microchannel (i.e., at $h = 0$), this results in a maximum flow velocity v_{max} of only 1.5 v_{av} as indicated by the formula[67,68], while in circular channels a maximum of 2 v_{av} prevails in the centre[65].

3.2.2   The Reynolds number

To estimate fundamentally whether a fluid will flow laminarly or turbulently, the Reynolds number Re is usually used. This is a dimensionless number and calculated from the density of the fluid ρ, the flow velocity v, the dynamic viscosity η and the characteristic length of the body or channel d:

$$Re = \frac{\rho\, v\, d}{\eta} \tag{3}$$

The dynamic viscosity can be determined from the kinematic viscosity v and the density of the fluid:

$$\eta = v * \rho \tag{4}$$

In pipes or round (micro) channels, the diameter of the pipe is usually used as the characteristic length. In the special case of rectangular channels, as used in this work, the hydrodynamic diameter D_h is applied, which can be calculated from the cross-sectional area A and the perimeter L[63,69]:

$$D_h = \frac{4A}{L} \tag{5}$$

According to J. Rotta, turbulent flow behaviour is to be expected above a Reynolds number of about 2200 and laminar flow below this critical value[70]. It should be noted, however, that this transition between the flow states is not as sharp as the Reynolds number suggests. Rather, other factors such as the surface properties of the channel are involved here, making it more of a transition region where laminar and turbulent flows can alternate[69]. In all experiments in this work, the Reynolds number never reached values above 0.01, so that laminar flow behaviour could be assumed in all cases.

3.2.3 Inertial Microfluidics

Particles in a laminar flow regime follow the streamlines, hence their trajectory can be predicted exactly and calculated as a function of time. If several fluid flows are combined in a microchannel, the particles follow the flow of the medium they were originally introduced into the channel with[71]. Therefore, so-called sheath flows are often used to line up particles of a sample or to keep them distant from the channel walls. This is called hydrodynamic flow focusing and is shown in Figure 2[72].
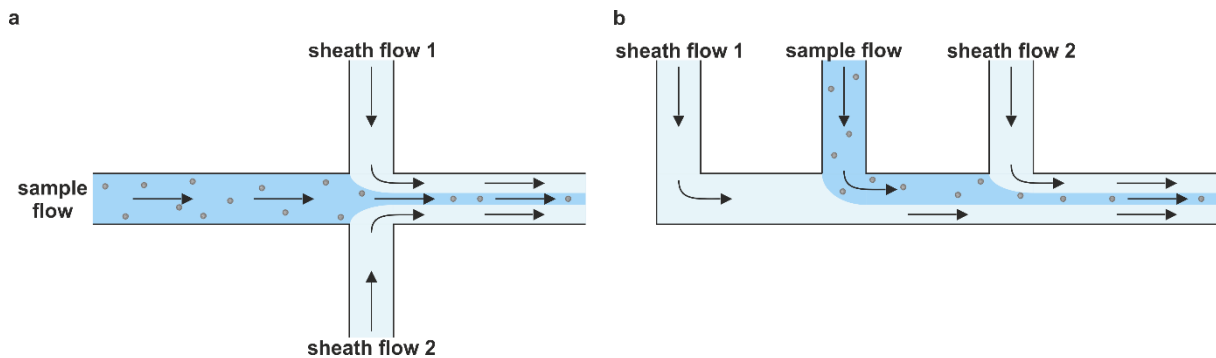
Figure 2: Hydrodynamic flow focusing. a, Top view of the channel. A laminar flowing fluid (dark blue) containing particles (grey) is hydrodynamically focused by two additional flows (light blue) flowing laterally into the channel. The particles follow the flow and arrange in a row. The flow velocity increases according to the increase in volume caused by the additional fluid. **b**, Side view of the channel. Several flows are layered on top of each other using different inlets to achieve hydrodynamic flow focusing.

Particles in a microchannel experience different forces from the surrounding fluid at different positions due to the flow profile, which not only results in a varying flow velocity, but can also lead to a specific arrangement or separation of the particles[73–76]. However, this requires very high flow rates, which were explicitly not used in this work. Since the field of inertial microfluidics is certainly relevant in the area of particle separation, the main effects are still briefly explained below.

If a particle is large in relation to the channel dimensions or if the flow profile in the channel is very steep, the particle is located in areas with different velocities. Accordingly, it moves with a velocity that has a value between the flow velocities at its surface: The side of the particle facing the centre of the channel moves slower than the fluid, while the side facing the channel wall moves faster. This creates shear forces, which can generate a lift force acting towards the channel wall, while wall effects counteract this. As a result, the particle arranges itself at a position where the forces are in equilibrium. For round channels, this equilibrium is at 0.6 times the channel radius, for rectangular channels it depends on the channel dimensions and the flow velocity[77]. In addition, a rotation of the particle can be caused by the acting forces, which in turn can also induce a force at high flow velocities.

Figure 3 shows a schematic representation of the forces. In addition to the hydrodynamic arrangement of the particles, in the case of biological cell samples shear forces can have an influence on cell vitality[78].
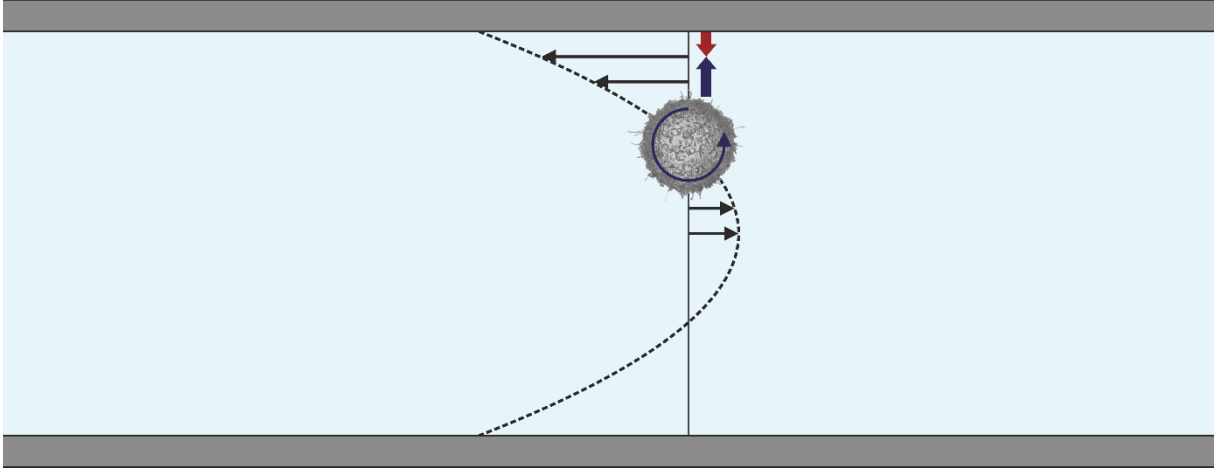
Figure 3: Hydrodynamic forces acting on particles in microchannels. Due to the parabolic flow profile (dotted black line), a cell is exposed to different flow velocities at its surface (black arrows), which deviate from its average velocity (indicated by the vertical black line). This creates inertial shear forces (blue arrow) that can cause the particle to rotate and move towards the wall. Wall effects (red arrow) counteract this movement.

3.3 Dielectrophoresis

3.3.1 Particles in the dielectrophoretic field

Dielectrophoresis (DEP) describes the interaction of (dielectric) particles, located in an inhomogeneous electric field, with the latter[79,80]. This distinguishes DEP from electrophoresis, in which a homogeneous field is present. A particle placed in an inhomogeneous electric field is induced a dipole moment q, which depends on the particle size, its permittivity, and the permittivity of the surrounding medium. If the particle is in an alternating electric field, as is the case in the experiments in this work, a time-dependent component is also introduced[81]. The following can be assumed for the calculation of q:

$$q(t) = 4\pi r^3 \varepsilon_M f_{CM} E(t) \tag{6}$$

Here r is the particle radius, ε_M the permittivity of the surrounding medium and f_{CM} the Clausius-Mossotti factor. This takes into account the (complex) electric conductivities of the particle and the medium:

$$f_{CM} = \frac{\sigma_P^* - \sigma_M^*}{\sigma_P^* + 2\sigma_M^*} \tag{7}$$

With

$$\sigma^* = \sigma + i\omega\varepsilon\varepsilon_0 \tag{8}$$

ε_0 is the dielectric natural constant, ε_P the permittivity of the particle and $\sigma_{P,M}$ the electric conductivities of the particle and the medium, respectively. Furthermore, $i^2 = -1$ applies[82].

Due to the dipole moment, the particle experiences a force along the field lines that depends directly on q and the gradient ∇E of the electric field:

$$F = q\nabla E \tag{9}$$

Therefore, for the time-averaged DEP force acting on the particle, the result is

$$\langle F_{\text{DEP}} \rangle = 2\pi r^3 \varepsilon_{\text{M}} Re(f_{\text{CM}}) \nabla E_{\text{rms}}^2 \tag{10}$$

where rms describes the root mean square value.

The considerations presented here apply to homogenous dielectric particles. However, the calculations (especially equation 7) become much more complicated if the particle is a biological cell, as it is inhomogeneous and the cytoplasm and cell membrane contribute differently to the permittivity[83]. The exact relations have been investigated earlier and will not be discussed in detail here, as the general concepts described remain unchanged[84].

It can be concluded that the strength of the exerted force is directly dependent on the radius of the particle, the gradient and strength of the electric field and the Clausius-Mossotti factor. In the case of the particle radius and the electric field gradient, this relationship is simple: the larger the particle and the steeper the field gradient, the stronger the force exerted. The field strength can be influenced by the applied voltage while the field gradient depends on the electrode shape and arrangement. In the case of the Clausius-Mossotti factor, the correlation is more complicated due to the frequency dependence[85]. Depending on the frequency of the alternating field, the factor can acquire values between -0.5 and 1 and thus influences the strength of the force exerted (see equations 7 and 10). At the same time, this determines the direction of the force: In the case of positive values, it is directed towards the field maximum, meaning that particles in the field migrate towards the electrodes. This is called positive DEP and depicted in Figure 4. In the case of negative values of the Clausius-Mossotti factor, the force acts towards the field minimum and drives particles away from the electrodes. This is called negative DEP[55,80,81].

For the selection of the applied field frequency in this work, various effects of the electric field on the electrodes and cells had to be taken into consideration[83]. For example, field-induced negative effects on the cell near the electrodes are more likely due to the high field strength[86]. Details on this are given in section 3.4.1. The use of a frequency that produces negative DEP is therefore advantageous, as the cells are kept at the greatest possible distance from the electrodes in this way. In the case of cells in standard cell culture medium, this is the case at almost all frequencies as depicted in Figure 5.
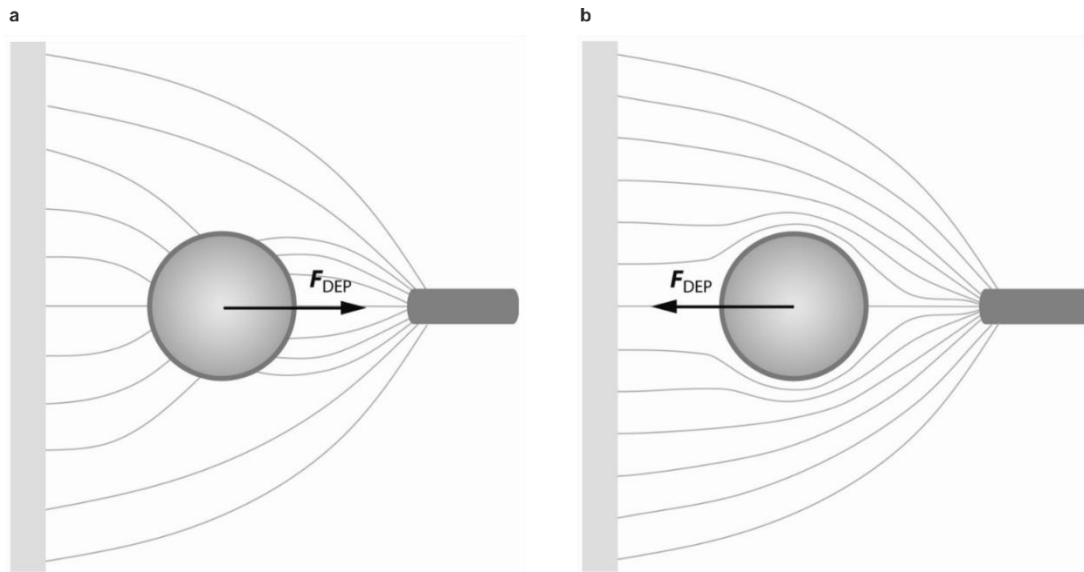
Figure 4: Principles of positive and negative Dielectrophoresis. Particles in an inhomogeneous electric field are polarised. **a**, If the polarisability of the particle is higher than that of the surrounding medium, the particle is driven towards the field maximum by the DEP force (F_{DEP}). **b**, If the polarisability of the particle is lower than that of the surrounding medium, it is forced towards the field minimum. Taken from[87].

In general, a high field frequency helps to reduce negative influences on the vitality of the cells as the membrane potential of the cells is less affected[88,89]. At the same time, it prevents potentially harmful electrochemical effects on the electrode surfaces. In contrast, a low frequency and a resulting minimum of the Clausius-Mossotti factor at -0.5 is advantageous with regard to the absolute DEP-force and the associated strength of cell deflection. According to M. Kirschbaum, a field frequency of 1 MHz was chosen as a compromise for all experiments, since at this value represents the maximum possible field frequency at which the maximum DEP force can be achieved (see Figure 5)[90].
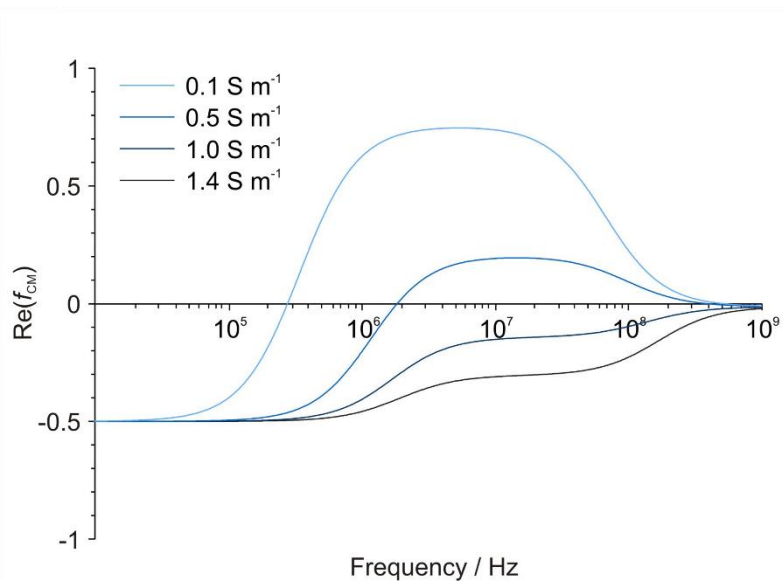
Figure 5: Real part of the Clausius-Mossotti factor for a mammalian white blood cell. Displayed are calculated values for cells in different conductive media. In this work, only cell culture medium with a conductivity of 1.4 S m^{-1} was used. Taken from[90].

3.3.2 Force interactions in DEP microsystems

In this work, DEP was used for particle manipulation in microchannels. The field-emitting electrodes were located at the top and bottom of the microchannel. The forces exerted by the fields on the particles therefore not only pointed away from the electrodes, but also towards the centre of the channel[55,82]. A schematic overview of all relevant forces acting on a particle in the electric field flowing in the microchannel is shown in Figure 6. A particle can only be hindered from moving on if the horizontal component of the DEP force F_{DEP} is greater than the resistance force F_{DRAG} exerted on the particle by the fluid.
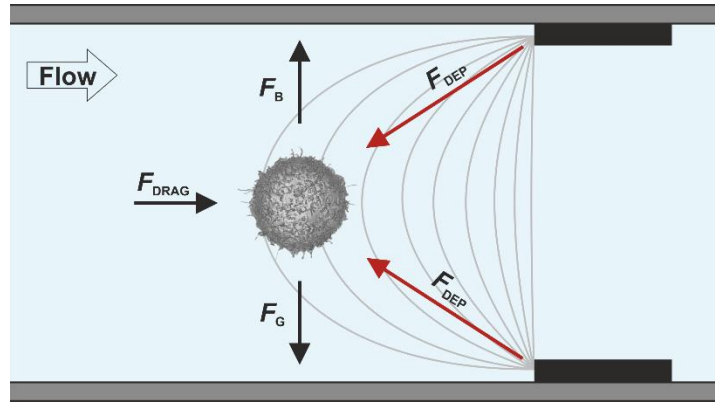
Figure 6: Forces acting on a particle inside a microchannel (side view). A particle suspended in a liquid is carried forward towards electrode structures (black) with the force F_{DRAG} according to the flow velocity. The horizontal component of the force F_{DEP} exerted by the electric field (grey lines) counteracts this force. At the same time, the vertical component of the DEP force acts towards the minimum of the electric field located in the centre of the channel and thus counteracts the buoyancy force F_B and the gravitational force F_G.

For continuous particle manipulation in the flow, not only a simple trapping of the particles in the flow is necessary, but primarily a targeted deflection, i.e.,, a lateral displacement transversal to the flow. For this purpose, long transversing electrode pairs are often used, which are positioned in the channel at an angle to the direction of flow[52,53,91–94]. Hence, not only the ratio of the magnitude of the DEP force and the drag force is decisive for the deflection, but also the angle at which the two forces act in relation to each other.

Here, two extreme cases can occur: With an electrode angle of 0° relative to the channel wall, the two forces do not counteract each other at all, meaning that deflection occurs with any given magnitude of DEP force. With an angle of 90°, on the other hand, the forces oppose each other completely, requiring the DEP force needed for deflection to be at least as large as the drag force. For all angles between 0° and 90°, geometric considerations imply that the DEP force required for deflection is a function of the sine of the electrode angle. Consequently,

$$F_{DEP} = F_{DRAG} * \sin(\alpha) \tag{11}$$

applies with the DEP force F_{DEP}, the drag force F_{DRAG} and the electrode angle relative to the channel wall α. This implies that the flow velocity achievable at full particle deflection scales

with $\sin(\alpha)^{-1}$, as it is linearly related to the drag force. A schematic of the forces is shown in Figure 7a&b.

A particle in the vicinity of the angled electrode experiences a DEP force which is dependent on the distance of the particle from the electrode. If the force is too small to counteract the drag force, the particle is driven closer to the electrode, where it experiences a stronger DEP force due to the higher field gradient. Consequently, a force equilibrium is established between the DEP force and the drag force, in which the particle is kept at a constant distance from the electrode and is deflected. The corresponding diagram is shown in Figure 7c&d. However, if the DEP force directly at the electrode is not strong enough to compensate for the drag force, the particle will break through the field barrier and cannot be deflected.
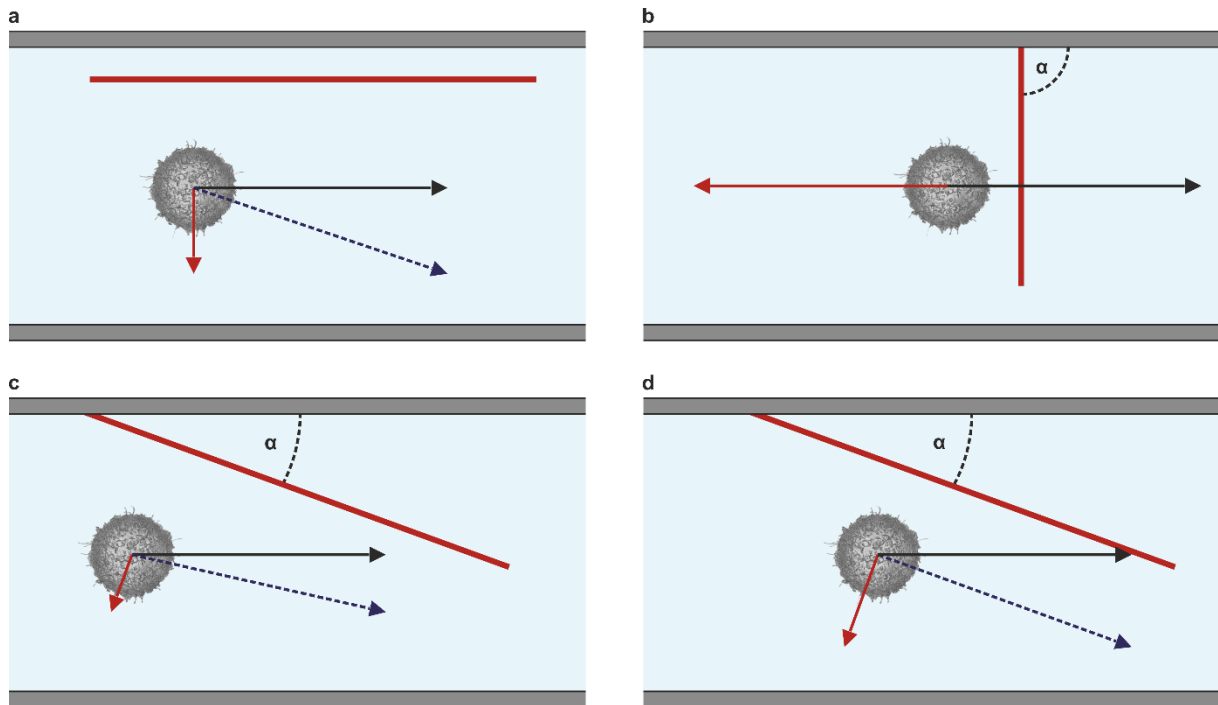
Figure 7: Angular dependence of the DEP deflection (top view). a, A particle inside a microchannel experiences a driving force F_{DRAG} by the surrounding liquid (black arrow). In the case of an electrode (red line) parallel to the channel wall, the DEP force F_{DEP} exerted by the electrode (red arrow) acts on the particle perpendicular to the drag force. Since the two forces do not counteract each other, a deflection (dotted blue arrow) of the particle always takes place if the electrode is active and a negative DEP force is exerted. **b**, In the case of an electrode completely perpendicular to the flow, the DEP force needs to completely counteract the drag force in order to achieve deflection of the particle. **c**, In the case of an angled electrode, the forces partially counteract each other depending on the angle α. The trajectory resulting from both forces points towards the electrode, consequently the particle moves closer towards the electrode and therefore into a region of a higher field gradient. **d**, When F_{DRAG} and F_{DEP} are in equilibrium, the particle is kept at a constant distance from the electrode.

3.4 Cell vitality

Typically, cells of interest are used further after their isolation[28,36]. An important aspect when working with biological cell samples is therefore damage-free handling. Ideally, a cell processed with a (sorting) system behaves exactly the same way as an unprocessed cell does.

In the case of the DEP technology used in this work, the electric fields in particular can influence cell vitality. They not only interact with the charged cell membrane, but also lead to an increase in ambient temperature due to joule heating[95–98]. Hence, both effects are briefly discussed.

3.4.1   Influence of electric fields on the membrane potential of cells

In its physiological state, a biological cell has a membrane potential of approximately -65 mV[99]. This potential is of crucial importance for the function of various membrane proteins of the cell. These include ion channels, pumps, enzymes and transporters[95].

The dipole induced by the electric field generates a voltage drop across the membrane and superimposes the cell's resting potential[100]. This can trigger signalling cascades in the cell and disrupt the function of the cell[98,101].

In addition, the effect of the electric field can lead to a molecular rearrangement of the lipid bilayer, which can result in the formation of temporary pores in the cell membrane. This process is called electroporation and temporarily increases the permeability of the cell membrane for ions and molecules.

This effect is used deliberately, for example to achieve targeted transfection of cells[102]. Short pulses in the range of micro to milliseconds at relatively high transmembrane voltages of 0.2-1 V are commonly used for this purpose[103]. Pores with a size of between approximately 1 nm and more than 1 µm are created, the exact size depending, among other things, on the electric field strength and the pulse duration[96]. The pores created in this way quickly close again, meaning that the cell is usually not permanently damaged.

In the case of particularly strong and/or long-lasting fields however, the lipid membrane can permanently break down, which inevitably leads to cell death[97,102]. It therefore makes sense in the interest of cell vitality to minimise the fields acting on the cell. In the DEP system used here, the cells are inevitably exposed to the electric fields for a relatively long time, with voltages of up to 5 V being applied.

3.4.2   Joule heating

Various (external) influences that have adverse effects on the cellular metabolism or the tertiary structure of proteins can induce a stress response in mammalian cells. These include, for example, glucose deficiency and anoxia, as well as the presence of ethanol, heavy metals or pathogens[104]. Another factor is heat. Since an increase in the ambient temperature by more than 4 °C above the physiological temperature already leads to the denaturation of proteins, it causes the expression of heat-shock proteins in mammalian cells, which serve to stabilise other protein structures and thus make them more resistant. Despite this mechanism, cell damage

cannot be ruled out if a cell is exposed to a significantly elevated temperature for a longer period of time[105].

As the electrodes used in this work are in contact with the cell culture medium, a current flows through this medium. Due to the finite resistance of the medium, a voltage drop occurs and the electrical energy is converted into heat. This is called Joule heating or Ohmic heating[86].

In the present system, this heat is dissipated by thermal conduction through the glass surfaces as well as the liquid flow prevailing in the channel. While heat conduction predominates at low flow velocities, flow-related heat transport is more important at higher flow velocities (above 500 µm s^{-1})[83]. At higher flow velocities in turn, a higher field strength and thus a higher voltage is also required for particle deflection. Since both the heating and the deflection efficiency of particles are quadratic functions of the voltage, the two largely cancel each other out[81]. However, due to the relatively small but constant contribution of thermal conduction to heat dissipation, a minimal temperature increase can be expected at higher flow velocities and voltages. It can be assumed that this increase is in the single-digit degree range above room temperature with the parameters of up to 1 mm s^{-1} and up to 5 V used in this work[83].

3.4.3 Investigation of cell vitality

The individual cells of a cell sample can differ in terms of their vitality status, i.e., regarding their cell division rate, metabolism and motility. In order to determine the vitality of a cell sample, these parameters are examined[89,106]. Although it could be shown that DEP fields can be used for gentle cell handling, this does not allow any general conclusion regarding the cell vitality since the influence depends on the cell type, setup and the field parameters[88–90]. A detailed investigation of the cells processed with a specific system is therefore inevitable. However, the fields do not necessarily induce a binary cell response, i.e.,, do not directly lead to cell death. Simple procedures such as staining with trypan blue or propidium iodide that only roughly distinguish between cells with intact membranes and those with defective membranes, i.e.,, between living and dead cells, are unsuitable for the quantification of cell vitality in this case. Instead, more complex protocols are needed that allow a more precise assessment of cell vitality[106–108].

For the suspension cells used in this work, the investigation of the cell division rate and metabolism was used to determine their vitality.

Determination of the cell division rate

The cell division rate can easily be obtained by counting the number of cells in the sample at different time points. This is an established standard process in every cell culture laboratory, for which various counting chambers are available[108]. One of these chambers with a defined volume is loaded with a sample of the cell suspension and is counted manually under the microscope. The cell concentration of the original sample can then be calculated from the number of cells and the volume of the chamber. Automated systems operate according to the same principle, counting the filled chambers automatically on the basis of a camera image. In all cases, an additional live-dead staining of the cells can be performed to determine their proportion within the sample[107].

Determination of the metabolic cell activity

Determining the metabolic activity of a cell sample is more complex than determining the cell division rate, but commercially available assays are available for this purpose. As a basic principle, molecules are introduced into the cells and metabolised[109]. In contrast to the introduced reactants, the resulting products are fluorescent or coloured, staining the cells or surrounding medium. A quantitative measurement of the staining or fluorescence then allows drawing conclusions about the average cell vitality of a sample, as healthy cells usually show a higher metabolic activity than damaged cells[110]. The various assays available make use of different mechanisms within the cells[111]. Commonly used assays are based on the cell's internal protease activity or the presence of adenosine 5'-triphosphate (ATP) or nicotinamide adenine dinucleotide phosphate (NADPH)[111–114].

Among the NADPH-based assays are tetrazolium assays. For these, differently charged tetrazolium salts are introduced into the cell, where they are converted to coloured formazan by NADPH[115–118]. Subsequent measurement of the absorbance provides information on the cell metabolism and the vitality.

In this work, a 2-(2-methoxy-4-nitrophenyl)-3-(4-nitrophenyl)-5-(2,4-disulfophenyl)-2H tetrazolium, mono-sodium salt (WST-8) based assay was used to determine metabolic cell activity in combination with cell counting.

3.5 Cell isolation techniques

Since the isolation of cells plays an important role in biology, biomedicine and biotechnology, as described earlier, a large number of different methods have developed over time[1,5,40]. Although the various methods pursue the same objective, they differ enormously regarding their mode of operation. For example, there are systems that process cell samples simultaneously (batch method) and systems with a continuous mode of operation[119]. The various concepts also differ, sometimes significantly, in the parameters analysed and the depth of information obtained about the target cells. In addition, differences exist with regard to performance, i.e.,, in terms of the purity of the processed sample, the throughput and the yield[120]. For a comparison of different systems, it is therefore essential that these terms are used uniformly. For this reason, these and some related terms are defined below and used accordingly in this work.

3.5.1 Definitions of terms

The *specificity* describes the ability of a system to correctly distinguish target cells from non-target cells. It is closely linked to the sensitivity, as only both parameters together allow an evaluation of the correctness of the cell identification.

The *sensitivity* describes the ability of a system to identify target cells as such. As described above, it is closely linked to specificity.

The *throughput* describes the cell number of processed cells per time period. It is usually used for characterising continuous flow devices and depends on the flow rate and the density of the cell sample. A new concept suggest that the depth of the analysed data should also be included

in the definition[121]. Following the definition used in electrical engineering, this is intended to allow better comparability of different systems.

The *purity* describes the proportion of target cells in the processed cell sample. Ideally, it is 100%, but due to various influences this is usually not achieved.

The *yield* describes the return of target cells in relation to the target cells present in the initial sample and is influenced by sensitivity, as well as other factors. A high yield is particularly desirable when processing samples with a low absolute number of target cells. The term yield is also occasionally used to indicate the proportion of lost cells in the course of an isolation process.

The *recovery rate* indicates the absolute proportion of (target) cells that can be recovered from the original sample after the isolation procedure. Similar to the yield, this parameter is particularly important for samples with highly valuable cells or a low number of target cells.

The *sorting window* describes the minimum spatial or temporal distance between two cells in order to process them individually and consequently ensure successful separation in active sorting systems. It is characteristic for the system and depends on the used technology. To estimate the sorting success (i.e., the purity after sorting), not only the size of the sorting window but also the variability of the distances between the individual cells as they flow through the system must be taken into account. The exact number of cells being located inside the sorting window at a given time point is statistically distributed and can be determined with Poisson statistics:

$$P_\mu(k) = \frac{\mu^k}{k!} e^{-\mu} \tag{12}$$

Here P is the probability that exactly k cells are located within the sorting window, μ is the mean expected number of cells in the sorting window at any given time and e is Euler's number[122]. For example, for an expected value of $\mu = 1$ (i.e., on average 1 cell per sorting window length), in 26.4% of all observed cases more than one cell is located within the sorting window. This inevitably leads to non-target cells being sorted together with the target cells and the resulting purity being reduced[26,120]. A detailed consideration of the correlations including the consideration of the target cell concentration within the sample is given in the appendix. In summary, these considerations show that the achievable purity must decrease with increasing throughput, provided that this is achieved by densifying the cell population.

The *sorting mode* describes the boundary conditions for the decision-making of the sorting algorithm. Depending on these boundary conditions, the sorting decision of the system and thus the target cell purity can be influenced. Typically, two modes are applied: yield sorting and purity sorting. In yield sorting, all target cells are sorted from the sample, without taking into account cell distances and thus cells flowing in front of or behind the analysed cell. This ensures a high target cell yield, but since non-target cells are also collected, the purity is reduced as described above. In the alternative purity sorting, target cells are only sorted if they are isolated within the sorting window. This ensures a high purity, but in analogy to the purity drop described above, this mode leads to a reduced yield at higher cell densities[26].

3.5.2 Parameters for cell characterisation

Cell populations and individual cells can differ in a wide range of properties. These include cell size, shape and density, mechanical properties such as the deformability of the cell, the presence or absence of specific surface markers, electrophysiological properties such as polarisability, and the size and distribution of intracellular components[29].

These properties can be used to identify and isolate target cells. However, there is a big variation with regard to the achievable differentiability and the analytical effort required for it. Depending on the application, a particular method may be best suited for isolating the target cells. For example, the size of a cell is relatively easily accessible, e.g., through a filtration mechanism[17,18]. A differentiation based on morphologic characteristics such as the nucleus/cytoplasm ratio, on the other hand, allows a finer distinction, but would require a more complex analysis system. In general, the analysis of different properties is often combined in order to achieve better target cell identification[44–46,50].

3.5.3 Methods for isolating cells

The methods and systems available for cell isolation can be roughly divided into conventional methods and microfluidic methods according to their mode of operation. The microfluidic methods in turn can be further divided into active and passive methods. The most important and widely used methods are briefly described below. Particular attention is paid to active microfluidic image-based sorting methods introduced in recent years, as the system presented in this work is related to them.

Conventional methods

One of the simplest and most user-friendly methods for cell separation is density gradient centrifugation. Here, a sample is placed inside a centrifuge tube containing a medium with a continuous or discontinuous density gradient. The gradient can be produced by a variety of established substances[123–125]. As the sample is rotated in a centrifuge, cells migrate outwards due to inertia and separate into layers of equal density. Density gradient centrifugation is a standard procedure in the separation of blood into its components.

Various filtration devices have also been established, in which the cells are separated on the basis of their diameter. Similar to centrifugation, these devices are mostly used for sample preparation prior to experiments, for example to isolate white blood cells (WBCs) from whole blood[126,127].

Some methods require pre-treatment of the cells to label the target cells of the sample. For example, one common approach requires the coupling of magnetic particels (mostly nanobeads) to the target cells. These are kept in place by an external magnetic field as they flow through a column, while the non-target cells continue to flow unimpeded. The target cells can then be flushed out after the field has been switched off, achieving separation by a time shift. This method is called Magnetic Cell Separation or Magnetic-activated cell sorting (MACS)[19–21].

Microfluidic methods

A variety of other separation methods developed with the emergence and rise of microfluidics as a toolbox for the handling of small objects. These can be classified as passive and active systems. While passive methods operate without information processing and configuration change, active methods are characterised by information processing and a configuration change derived from it.

Passive methods

A common method for cell separation in microchannels is the utilisation of inertial forces. In inertial microfluidic systems, cells flowing inside the channels at high flow arrange themselves at different equilibrium positions due to the channel geometry (see section 3.2.3)[67,73,74,77,128]. Basic inherent cell properties such as size, shape, compressibility, and density also play a critical role. This is referred to as field flow fractionation or hydrodynamic spreading. In addition, the concept of inertial microfluidics is also used as a tool in other separation and sorting systems[69,129]. Typically, hydrodynamic focusing is used in these cases to align the cells of a sample (see section 3.2.3).

However, passive separation of the cell population is also possible at lower flow rates. For example, in deterministic lateral displacement (DLD) arrays, obstacles such as pillars in microchannels provide an uneven fluidic deflection of cells of different sizes and thus a separation of the cell sample[130,131].

In many cases, microchannels are combined with other methods to achieve cell separation not by inertial or hydrodynamic forces, but by external forces. In the case of free flow acoustophoresis, for example, sound waves are used. By forming standing acoustic waves (SAWs), the cells arrange themselves at different (lateral) channel positions due to their size, similar to the case of inertial microfluidic devices[132,133]. DEP is also used to arrange cells laterally or vertically due to their diverse interaction with the electric fields and thus to separate them[55,134–137].

Using magnetophoretic effects, magnetically-labelled cells flowing freely in the channel are separated from each other based on magnetic properties and directed to different outlets[14,22]. This method requires a magnetic labelling of the cells and is very similar to the well established MACS described above.

Active methods

To enable active sorting of cells based on a readout, a (usually optical) differentiation between target cells and non-target cells is required. This is usually achieved by labelling the desired cell population. Most commonly, antibodies, aptamers, or peptides are used that are targeted at specific surface markers and coupled to fluorescent dyes or magnetic particles. In the case of antibodies, such a construct is called an immunoconjugate. The target surface markers are mostly biomolecules in the cell membrane, making it possible to draw conclusions about the presence or absence of certain structures based on the observed staining.

While in the case of the methods described above non-labelled or magnetically labelled cells only allow a rough separation of the cells, labelling with fluorescent dyes in combination with an optical system allows a more detailed analysis of individual cells. The evaluation and identification of target cells enabled in this way can in turn be used to control a sorting mechanism and thus establish active cell sorting at the single cell level.

A wide variety of methods can be used as sorting mechanisms. For example, electric fields are utilised to generate DEP forces as described in section 3.3.1, but switched on and off in the case of active sorting[52,53,138,139]. The aforementioned SAWs offer the same capability for active switching[140]. Another possibility to manipulate individual cells in a controlled manner is the use of optical forces[141,142]. In this case, lasers are precisely activated to deflect particles.

A common feature of the given methods is the precise handling of the cells and the simple and fast controllability of the system. However, the underlying physical mechanisms of action provide only weak forces and thus weak deflection of the cells. Consequently, they can only be used at low flow rates and hence only allow a relatively low throughput.

State-of-the-art cell sorting

The most established technique for active sorting of cells today uses electric fields to sort differently charged liquid droplets in which the cells are located. It is named Fluorescence Activated Cell Sorting (FACS)[2,24–26,143]. Since its first publication in 1969, this technique has been continuously improved, but the basic mode of operation has not changed. Figure 8 depicts the schematic mechanism of FACS. In modern FACS devices, the cell sample pre-treated with fluorescent immunoconjugates is passed through a so-called flow cell. In this chamber, the cells are hydrodynamically focused by a sheath flow and guided through one or more laser beams. Two light signals are generated: on the one hand, the cells scatter the laser light due to their optical density, on the other hand, the fluorophores are excited and emit light of defined wavelengths. The light scattering depends primarily (but not exclusively) on the cell size and the complexity of the cell organelles. A detector opposite to the laser source collects the light scattered forward by the cells (FSC) and converts it into an electrical signal from which information about cell size, cell shape and cell spacing can be obtained. The light scattered sideways at a 90° angle (SSC) contains rough information about the internal complexity of the measured cell. The emitted fluorescence light is broken down into spectral bands with the help of dichroic mirrors, each of which is converted into electrical signals by a further detector. These signals contain information about the presence and absence of surface markers due to the coupling by specific antibodies. The information obtained from all detectors is combined to identify target cells.

The analysis region is followed by a nozzle through which the cells are forced together with the liquid stream. A piezo actuator causes the nozzle to vibrate at a defined frequency. This causes the emerging liquid jet to break up into individual drops, each of which containing a maximum of one individual cell. This principle is known as a jet-in-air system.

Immediately before the drop break-off, a voltage is applied to the liquid by an electrode, causing it to become positively or negatively charged. The detached droplet retains this charge, which is applied individually for each droplet break-off. The charge of a droplet depends on whether the system has identified a target cell, a non-target cell or no cell at all in it.

Finally, the individual drops jetted out of the nozzle fall downwards following gravity and the direction of ejection, passing through a static electric field set up between two electrically charged plates. Due to their own charge, the droplets are deflected sideways and subsequently collected in sample vessels. Modern FACS devices are able to distinguish between up to eight cell populations and collect them separately using different charges.
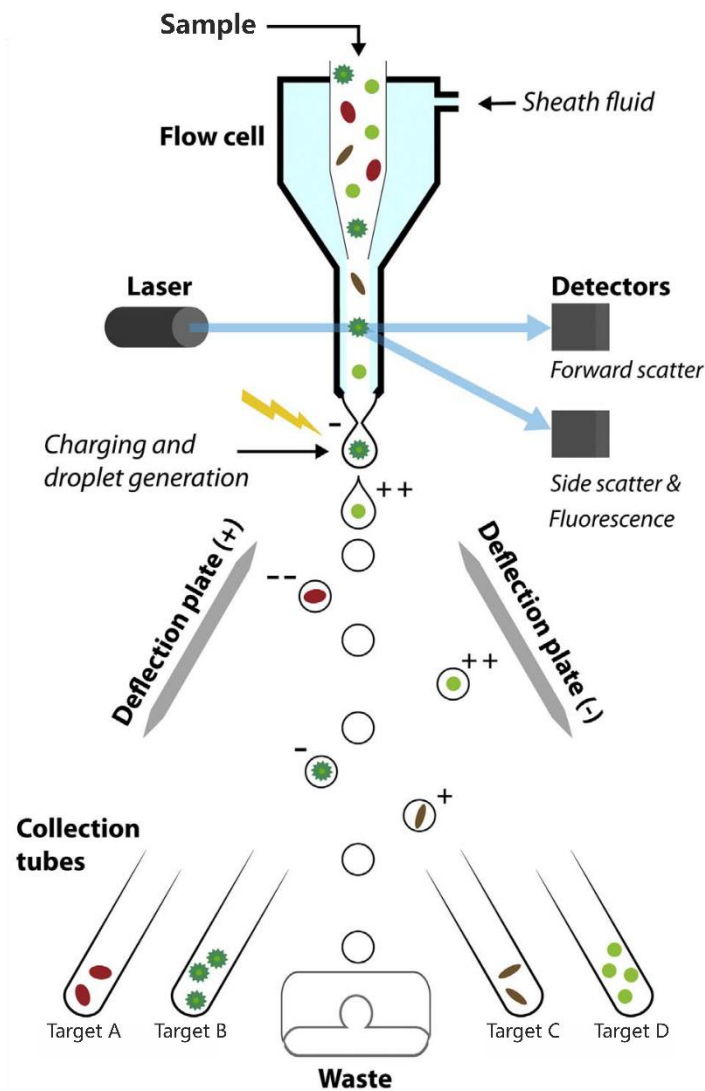
Figure 8: Working principle of a FACS. Pre-treated cells are hydrodynamically focused into a streamline inside the flow cell. The cells then pass through a laser beam, which is scattered by the cells and excites fluorophores. Both the scattered or emitted light is detected. The combined signal is used to identify the target cells. A vibrating nozzle at the end of the flow cell splits the liquid stream into individual droplets, each containing up to one cell. Shortly before the droplet breaks off, it is electrically charged according to the sorting decision. After the break-off, the droplet passes through an electric field in which it is deflected sideways according to the applied charge. Finally, the cells are collected in sample reservoirs. Modified from[2].

Antibody conjugates are available for virtually all relevant surface markers, and their light signals can be precisely separated by up to 17 channels in modern devices[25]. This wide range of applications, together with the high achievable cell throughput of several tens of thousands of cells per second, has ensured that FACS devices are now standard equipment in practically all cell processing research institutions.

Nevertheless, the devices offer potential for improvement: Possible cell damage due to shear stress in the nozzle and during hydrodynamic focusing (as well as due to the charge of the liquid) cannot be ruled out, which is particularly important for sensitive cell samples[78]. Furthermore, due to their high throughput, the devices require a certain minimum amount of sample volume or cells for calibration[35,57].

The biggest disadvantage, however, is the limitation in terms of data depth. Since only the presence and absence of colour information is measured, the spatial distribution of fluorescence within the cell cannot be mapped[30,35]. Possible morphological features such as clustering of proteins or co-localisation of surface markers therefore remain hidden[27,29].

In order to investigate spatial features in cells, the use of imaging technology is unavoidable. Over the course of the last years, first attempts with image-based cell sorting in microchannels have been developed[52,53,139–141]. Until recently, however, the technical possibilities to meet the emerging need for image-based cell sorting at high throughput were constrained by limited computing power, as image evaluation requires complex computational operations in a short time. The rapid development in the field of computer technology and the associated increase in the speed of image evaluation has helped to overcome this problem[144].

Consequently, new sorting systems have been developed in recent years, the two most important being introduced below.

A system called Intelligent Image-Activated Cell Sorting (iIACS), in analogy to FACS, was first presented in 2018[44]. An improved version of the system was published in 2020[45]. The system combines a microfluidic channel for flowing a cell sample with advanced microscope optics, a complementary metal oxide semiconductor (CMOS) camera, a high-end computer network for data analysis and a piezo-activated sorting mechanism. Since this system is also fluorescence-based, fluorescence labelling of the target cells is necessary in advance.

Inside a central, horizontally arranged microchannel, two sheath flows focus the sample cells first horizontally and then vertically. In this way, a continuous flow of cells is achieved in the centre of the channel, with the cells moving at about 1 m s^{-1}.

Immediately after hydrodynamic focusing, the cells pass through two laser beams, which are configured with one laser beam surrounding the other ring-like. Thus, the cells first pass from one side through the outer ring of the first laser, then pass through the second laser, and finally pass through the ring of the first laser again. The light emitted by the fluorescent dyes is collected by a 20x objective (NA 0.75), split and detected by two different systems.

Photodetectors collect the light coming from the two positions of the first laser. The flow velocity of each individual cell is then determined from the ring diameter and the time delay of the two signals.

The light excited by the central, second laser beam is first directed onto a rotating polygon mirror and subsequently onto the sensor of a complementary metal-oxide-semiconductor

(CMOS) camera. A dichroic mirror ensures the extraction of the excitation light from the beam and allows two different wavelength bands (green, 504-543 nm and red 591-800 nm) to reach the camera sensor. Due to its rotation, the polygon mirror causes the image of the cell on the camera sensor to be frozen, i.e.,, it does not move, even though the observed cell continues to flow. With this technique, longer exposure times and thus a better signal-to-noise ratio is achieved without motion blur[145].

A neural network then evaluates the image data and makes a sorting decision. Only a short time window of a few milliseconds is available for this, as the cell under investigation is flowing along the channel at high speed (i.e.,, 1 m s^{-1}). For this reason, a complex network system consisting of nine high-end computers is used for data processing.

Once a cell is identified as a target cell, a piezo-driven push-pull sorter is activated at the end of the microchannel depending on the determined velocity. This creates a flow in a channel intersection that is perpendicular to the direction of flow and deflects the cell sideways. As a result, the target cell is directed into a different outlet than the rest of the cell flow. The mechanism is shown in Figure 9.

The iIACS system is capable of processing several hundred to several thousand particles or cells per second, which is approximately an order of magnitude lower than the throughput of modern FACS devices. The purities achieved are 75% and more, and the recovery rate also amounts to about 75%. Due to the fast-flowing sheath flow and the resulting strong shear forces, cell damage cannot be ruled out since no data on cell vitality has been published.

Moreover, since several trained scientists are needed for the operation and monitoring of the system, it is less user-friendly in direct comparison to FACS. Furthermore, the system is likely to be expensive due to its high complexity.
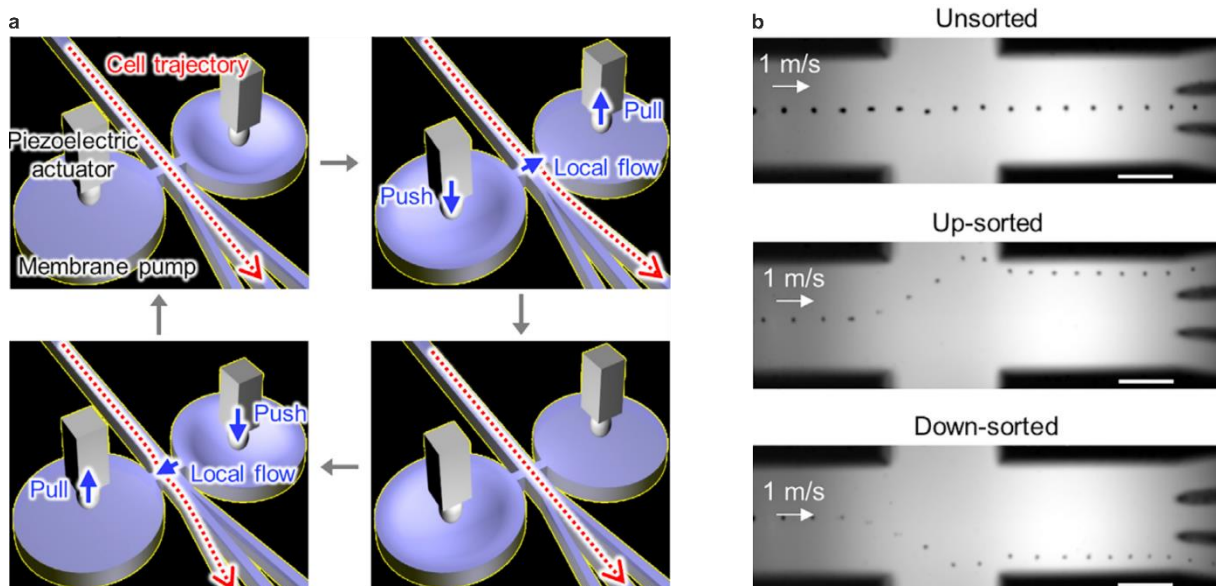
Figure 9: The push-pull sorter of the iIACS (taken from[44]**). a**, Top left: The hydrodynamically focused cells are directed to the central outlet when the sorting mechanism is inactive. Top right: Activation of the sorter generates a local flow and directs the target cell into another outlet. In this process, one membrane reservoir discharges while the other fills up. Bottom right: Subsequent cells are directed back into the middle outlet. Bottom left: The next target cell is deflected by the sorter into the outlet on the other side of the channel. **b**, Microscopic images of the sorting region for the three possible cell deflections described.

A system more similar to FACS than iIACS is the Image-enabled Cell Sorter (ICS), which was first presented in 2022 by Schraivogel *et al.*[50]. The method adopts the fluidics and sorting principle of modern FACS devices, i.e., it consists of a flow cell with a nozzle for droplet generation and sorts the cell sample by charging the droplets and electric fields. However, differences exist in terms of optics and image acquisition. Although laser light is also passed through the sample in ICS and a forward scatter and side scatter signal split into individual wavelengths is measured using photodiodes (PDs) and photomultiplier tubes (PMTs), both the laser configuration and the evaluation of the signals are much more complex.

The system's unique feature is the fragmentation of the excitation laser into an array of 104 adjacent laser spots across 60 µm via an acousto-optic deflector (AOD). Additionally, the individual laser spots are amplitude modulated at different frequencies and a reference laser beam is generated by another AOD. Both the individual laser spots and the reference beam pass through the core stream containing the focused cells in the flow cell and generate a signal. Due to the movement of the cells through the laser array, a profile of the cell along the flow direction is calculated from the temporal sequence of the measured values. The frequency superposition together with the reference beam also allows the determination of the individual signal component of each laser spot by Fourier transformation, thus achieving a lateral resolution of the cell. By combining both measurement results, a two-dimensional image of the cell is created, enabling image-based identification of target cells. This technique is called Fluorescence Imaging using Radiofrequency-tagged Emission (FIRE)[146]. A schematic overview of the process is shown in Figure 10.
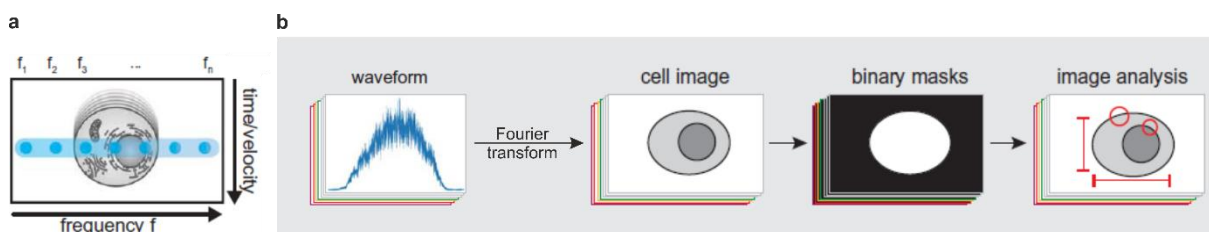
Figure 10: Functionality of the ICS data processing. a, Cells pass through an array of amplitude-modulated laser spots. **b**, The detected waveform-signals for each spot encode the image. Using Fourier transformation, images are generated and subsequently processed to obtain a set of image features that are used for cell classification and sorting (not shown). Modified from[50].

The system can achieve throughputs of up to 15,000 cells s^{-1}. This puts it in the range of current FACS devices and about one order of magnitude above iIACS. However, high purities of up to 96% were shown at only about 4000 cells s^{-1}.

A major advantage of ICS is its user-friendliness, as the basic FACS technique is established. However, this also means that it suffers from the same disadvantages. Furthermore, the image quality is not comparable to that of current fluorescence microscopes and the real time representation of the images is only possible to a small extent due to the limited available time.

4 Materials and methods

4.1 Microfluidic DEP chips and interfaces

The microfluidic chips used in the work consist of two glass slides of different thicknesses (170 µm and 500 µm) and a 35 µm thick polymer spacer in between, which forms the channel structure. On the inside of the glass slides, i.e., on the top and bottom of the channel, there are electrode structures made of platinum. The upper of the two glasses also features holes for the fluidic connection of the chip. The chips were manufactured by the company GeSIM mbh (Radeberg, Germany) according to channel and electrode designs individually created at Fraunhofer IZI-BB. Further information on the design of the microfluidic chips can be found here:[81,147].

Different microfluidic chips were used in the experiments carried out. These differed on the one hand in terms of channel geometry and electrode arrangement, and on the other hand in terms of the interface used and the resulting integration into the microfluidic system. The chip formats and designs used are listed individually below.

4.1.1 Format 1: CeProm chips

In the CeProm format microfluidic chips, the glass/polymer part is bonded to a carrier plate, which provides additional stability. Cutouts in the carrier plate allow microscopic observation of the microchannels. Two printed circuit boards (PCB) glued to the carrier plate are connected to the electrode structures by wire bonding and thus enable the electrical control of the microchip. A photo of a CeProm format chip is shown in Figure 11a. CeProm chips are designed for the use in a specially developed interface. This consists, among other things, of a metal mounting block that is screwed to the carrier plate. A carrier unit made of metal or plastic serves as a receptacle for the tubings used and is attached to the mounting block with the aid of a cover plate. With this configuration, the tubing ends are pressed directly onto the drill holes of the glass chip. A gasket ring around the tubings ensures a reliable sealing. A schematic of the interface is shown in Figure 11b. Figure 15 on page 28 shows a photo of the whole experimental setup.

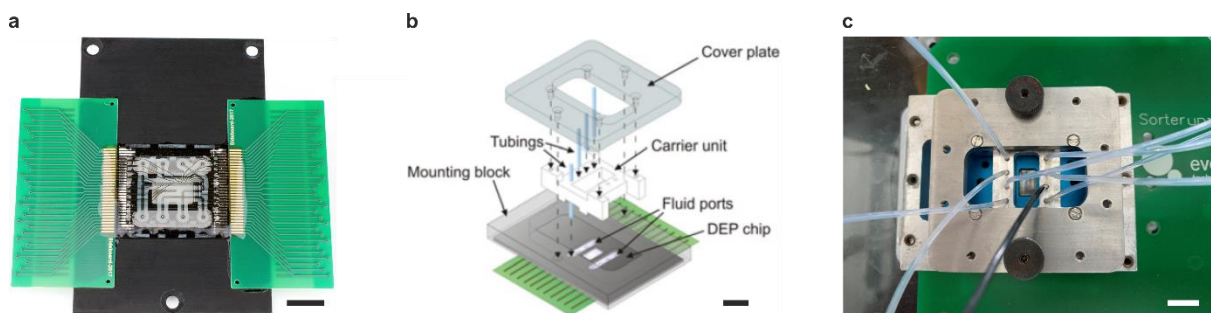**Figure 11: CeProm chip format and associated interface. a**, A microfluidic chip of the CeProm type. **b**, A schematic of the associated interface and the arrangement of the individual components around the chip. **c**, A CeProm chip in the installed state. Most of the microfluidic chip is covered by the interface. The scalebars represent 1 cm. Picture b taken from[90].

While the necessity of the interface limits the flexibility of the chips in CeProm format, it also minimises the dead volume in the system due to the connection principle of the tubing. Therefore, these chips are particularly well suited for experiments with high demands regarding the precision of sample insertion and extraction.

In the context of this work, a new chip design was developed and realised in CeProm format (see section 5.1.1). The microfluidic chip is branded PROC2 and was operated in two configurations. These are shown in Figure 12.

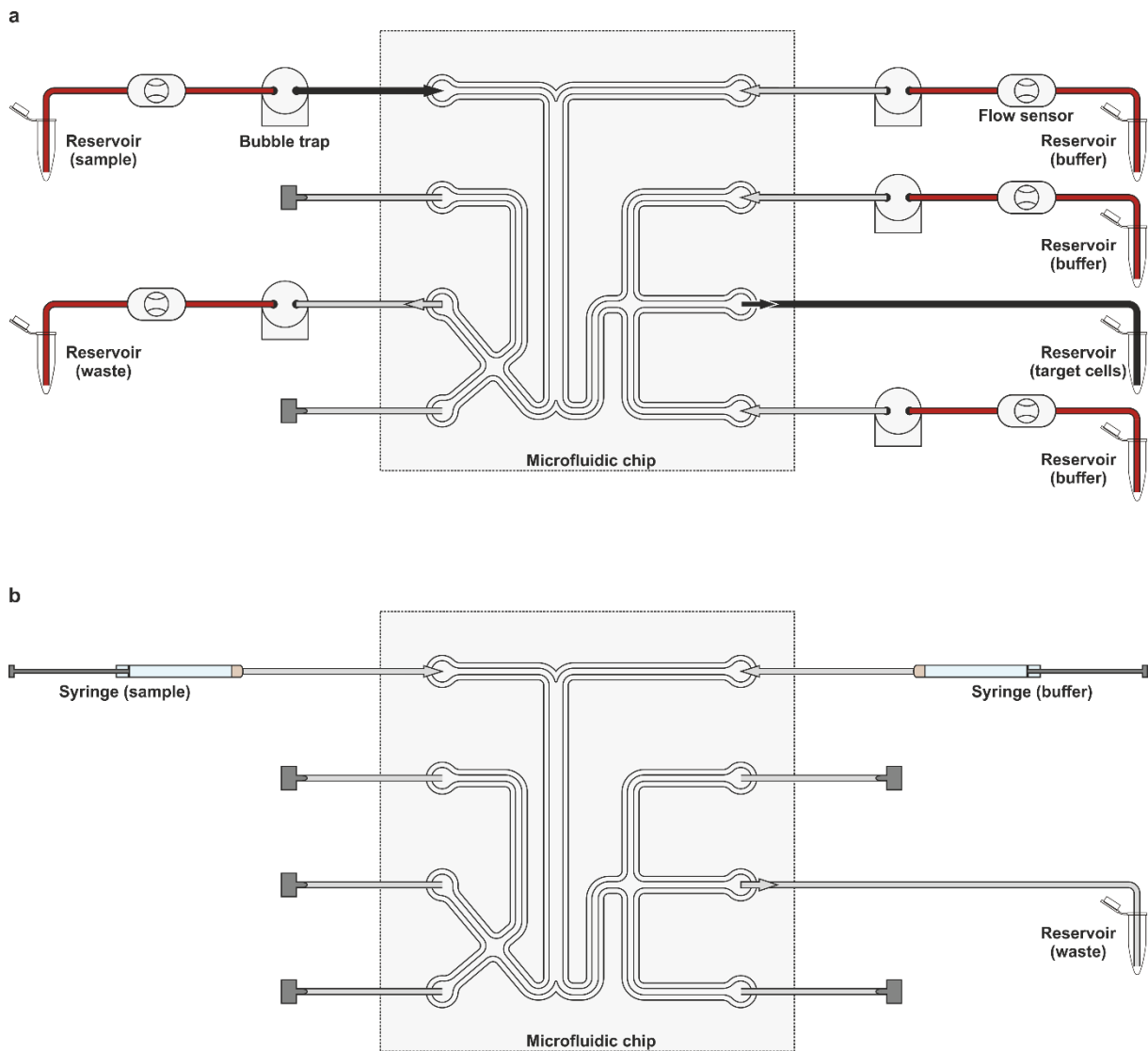**Figure 12: Configuration of the tubing system of the PROC2 chip (CeProm format).** Tubing maps for the configuration for cell sorting (**a**) and the configuration for the preliminary deflection experiments (**b**). The colours indicate the material as well as the inner (ID) and outer (OD) diameter of the tubings: red PEEK, ID 125 µm, OD 0.79 mm; black PEEK, ID 100 µm, OD 1.59 mm; grey FEP, ID 250 µm, OD 1.59 mm.

4.1.2 Format 2: DFC chips

In addition to the CeProm format described above, the chips made of glass and polymer spacer can also be processed into a simpler microchip. In this case, the electrodes are contacted via a pin strip, while fluidic adapters are glued onto the drill holes for the fluidic connection. Chips produced in this way are much more compact and easier to handle, but have a much larger dead volume due to the fluidic adapters. They are more suitable for preliminary tests and for demonstrating proof of principle. A photo of DFC chips is shown in Figure 14 on page 28, the corresponding tubing configurations are shown in Figure 13.
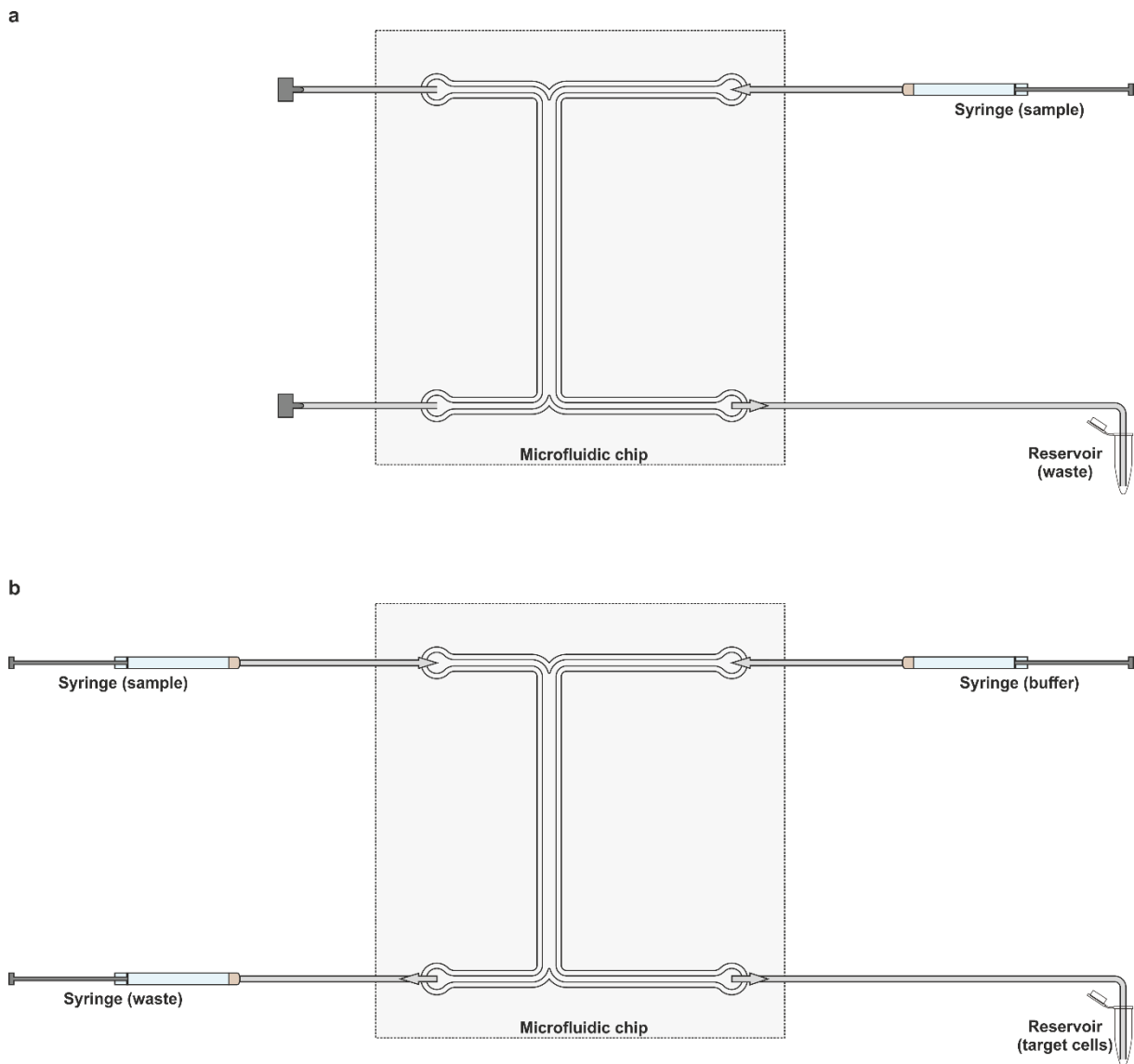
Figure 13: Configuration of the tubing system of the microfluidic chips in the DFC design. Tubing maps for the DFC chip to investigate angle-dependent cell deflection (**a**) and for refractive index-based cell sorting (**b**). The grey lines indicate FEP tubing with an ID of 250 µm and an OD of 1.59 mm.
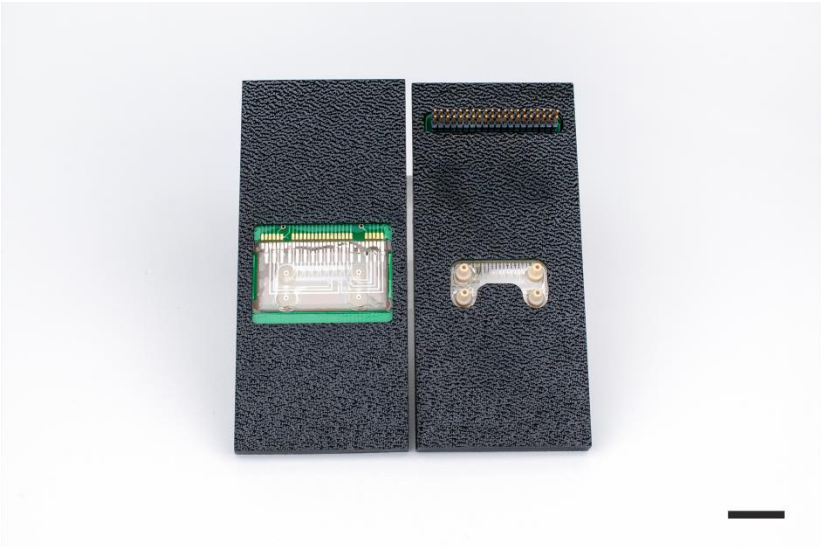
Figure 14: The DFC chip format. The photo shows the top and bottom of two DFC chips. The scalebar represents 1 cm.
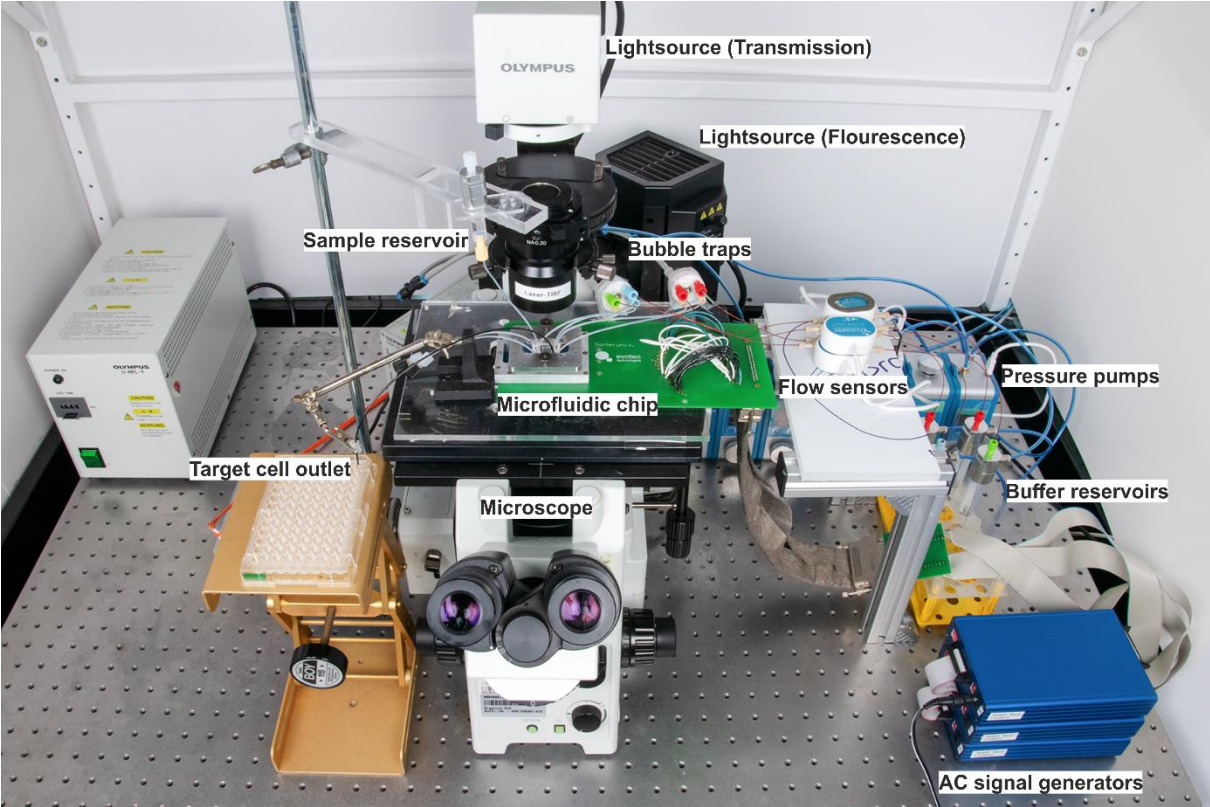
Figure 15: Experimental setup of the microfluidic system.

4.2   Microfluidic tubing

Different tubings were used to connect the microfluidic chips to the other components of the system. These were fluorinated ethylene propylene (FEP) tubing with an inner diameter (ID) of 0.25 mm and an outer diameter (OD) of 1.59 mm (marked grey in Figure 12 and Figure 13), polyether ether ketone (PEEK) tubing with an ID of 0.125 mm and an OD of 0.79 mm (red) and PEEK tubing with an ID of 0.1 mm and an OD of 1.59 mm (black).

4.3   Microfluidic pumps

Two different pump systems were used to control the volume flows within the microsystems. On the one hand, syringe pumps were used for this purpose, in which microlitre syringes are emptied at a defined speed. The glass syringes used had volumes of 500 µL, 1.0 mL & 5.0 mL. On the other hand, pressure-based pumps were used, in which the liquid is forced into the tubing system by means of an overpressure.

4.4   Signal generators

For the control of the electrodes, custom-made electric multichannel signal generators were developed. These can generate individually switchable square-wave signals with a frequency of 10 kHz to 10 MHz and amplitudes of 0 V to 10 V for each pair of electrodes. In this work, the frequency was kept constant at 1 MHz throughout all experiments and only the voltage was varied. The generators were controlled using custom-made software or Python scripts (see section 5.1.4). Data transmission was done using a standard USB connection leading to switching times of less than 4 milliseconds.

4.5   Microscopy and image acquisition

All images and videos of the cell sorting process were taken using custom-made python scripts on a dedicated microscopy setup through a 4x air or 60x oil-immersion objective, respectively. The CMOS camera was operated in global shutter mode. For fluorescence images, a 100 W mercury vapour lamp and various filter cubes were used. The exposure times were varied between 500 µs and 4 ms depending on the experimental conditions.

Preliminary experiments were performed on a separate microscopy setup with a charge-coupled device (CCD) camera and a 20x objective at an exposure time of 1 ms. Images were acquired using the image acquisition software HCImage.

4.6   Data analysis & processing

The collected data was analysed using Microsoft Excel and ImageJ. Graphs were created using OriginPro and CorelDRAW Graphics Suite.

4.7 Sorting algorithms and automated data processing

Several computer scripts written by Neus Godino were used for automated cell sorting. These use Python with various modules. For image adjustments these were *cupy*, and *opencv-python*, for cell tracking and making sorting decisions *numpy*, *time*, *scipy.spatial*, *opencv-python* and *collections*, for visualisation *opencv-python* and the *multiprocessing module*, for post analysis *numpy*, *opencv-python*, *SciPy* and *scikit-image*, and finally for generator control *pyserial*.

A standard desktop computer running Windows 10 was used to execute the scripts. Some processes were outsourced to the dedicated graphics processing unit (GPU).

While the target cell identification in the case of the red/green-based sortings was simply based on a defined colour space, it required a more complex analysis of the image data in the case of the membrane/cytosol-based sortings, since the stained cells fluoresced in a similar wavelength range. First, a pre-selection was made based on the size and shape of the recorded objects, so that only single cells were examined in the second analysis step. Using the images selected in this way, sixteen radially evenly distributed brightness profiles of each cell were then created, the course of which was characteristic of the respective staining. Profiles with a continuous increase in brightness towards the centre of the cell were assumed to be characteristic of cytosol staining and defined as C-type profiles. Profiles with a maximum in outer cell regions and a decrease in brightness to below 90% of the maximum value in the further course were assumed to be characteristic of membrane-stained cells and defined as M-type profiles.

Using about 1000 images of isolated membrane and cytosol stained cells, the distribution of the profile types for the respective staining was investigated. From these data, a sorting criterion was derived whereby a cell had to have three or more M-type profiles to be considered membrane stained. All other cells were classified as cytosol-stained. Exemplary cell images and corresponding brightness profiles for both cases are shown in Figure 16.

4.8 Microsystem filling and cell sorting

Prior to the experiments, all liquid reservoirs (syringes or centrifuge vessels, depending on the experimental set-up) were filled with degassed cell culture medium. For degassing, the medium was ultrasonicated for at least 30 minutes at 45°C at 100% power in degass mode. The entire system was then flushed until no air bubbles remained in the system. Then the cell sample was filled into the designated syringe or reservoir and pumped into the system.

The individual flow rates were set and varied individually for each experiment. In the case of sorting cells in the PROC2 chip, the same flow rates were used for all experiments, if possible, to enable comparability of the individual experiments. The flow rate of the sheath flow was set to 300 µL h^{-1} per inlet for each sorting. The flow rate of the waste was varied between -16 and -18 µL h^{-1}. The flow rates of the buffer and the sample were both varied between 5 and 35 µL h^{-1} so that a combined flow of 40 µL h^{-1} was achieved. This served to adjust the cell density in the main channel and corresponded to a cell velocity of approximately 580 µm s^{-1}. Just like the flow rates, the electrode voltages used were also kept constant. These were 3 V for the first electrode (E1), 3.5 V for the second electrode (E2), 3 V for the electrodes of the sorting array (E3) and 4.5 V for the separation electrode (E4).
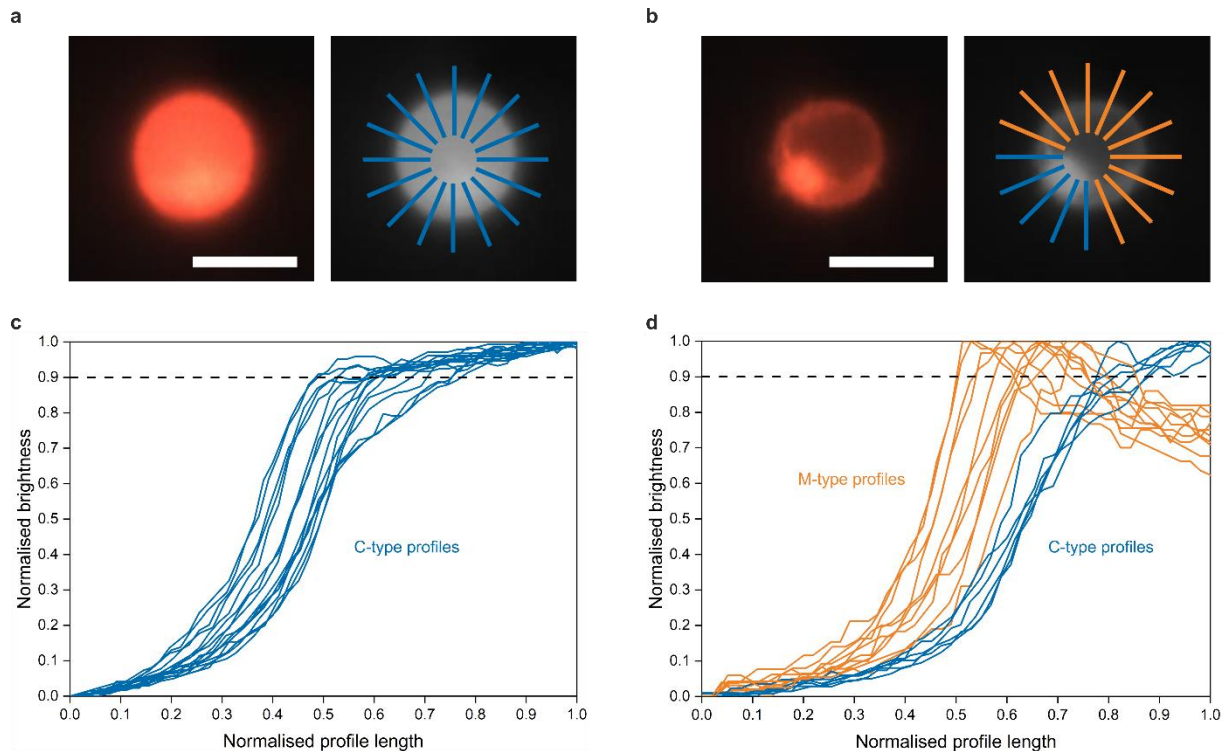
Figure 16: Analysis principle for the membrane/cytosol-based sorting. a, Exemplary image of a cytosol-stained cell (left) and of the same image in greyscale (right). Sixteen brightness profiles are radially evenly distributed over the outer cell border. The image was taken at 60x magnification and 0.5 ms exposure time. Scale bar, 10 µm. **b**, Exemplary image of a membrane-stained cell with corresponding brightness profiles, also taken at 60x magnification and 0.5 ms exposure time. Scale bar, 10 µm. **c**, Brightness profiles for the cytosol-stained cell from **a** (from outside to inside). The gradually increasing brightness towards the centre of the cell is characteristic for cytosol staining. **d**, Brightness profile for the membrane-stained cell from **b**. A large proportion of the profiles show a maximum value in the outer region and a decrease to less than 90% of the maximum brightness towards the cell centre. This is associated with a higher concentration of fluorescence in the membrane and characteristic of membrane-stained cells. Accordingly, these profiles were defined as M-type profiles (marked in orange), while the gradually increasing profiles were defined as C-type profiles (marked in blue). After testing various classification criteria, those cells were classified as membrane-stained that had at least three or more M-type profiles among the sixteen profiles. In collaboration with Neus Godino.

4.9 Cell culture

4.9.1 Cultivation of Jurkat cells

Human T lymphocytes of the Jurkat cell line were cultured in T25 cell culture flasks at 37 °C and 5% in RPMI 1640 cell culture medium supplemented with 10% fetal calf serum, 1% stable L-glutamine and 1% penicillin-streptomycin.

4.9.2 Preparation of conditioned cell culture medium

To prepare the conditioned medium, three T75 cell culture flasks were incubated with 50 mL cell suspension each in the incubator at 37 °C and 5% CO_2. The initial concentration of the cell suspension was $6.5*10^4$ cells mL^{-1}. After four days, the three T75 cell culture flasks were centrifuged at 100 g for five minutes and the supernatant was collected and sterile filtered. Two portions of the filtered liquid were aliquoted with one portion of fresh cell culture medium (see previous section) and 1% pyruvate and stored at -20 °C.

4.9.3   Cell staining and sample preparation

Prior to experiments, the cells were labelled with several fluorescent dyes. For a red cytosol staining, between 0.1 and 2 µL of a 2 mM solution of Calcein red-orange in Dimethyl sulfoxide (DMSO) was added to 1 mL of the cell sample with a concentration of ca. $5*10^5$ cells mL^{-1}. For a green cytosol staining, 2 µL of a 2 mM solution of Calcein in DMSO was added to 1 mL of the cell sample. For a blue DNA staining, four to eight drops of Nuc-Blue staining solution were added to 1 mL of the cell sample. For a red membrane staining, 2 µL of a 1.4 mM solution of Octadecyl-rhodamine (R18) in DMSO was added to 1 mL of the cell sample.

After an incubation period of 90 minutes at room temperature in the dark, the membrane-stained cells were washed twice and centrifuged at 100 g for three minutes each time. For cytosol- and DNA-stained cells, the cells were allowed to sediment and staining medium was carefully replaced with fresh medium, adjusting the cell concentration to approximately $8*10^5$ cells mL^{-1}.

Finally, 750 µL of the stained cell sample was mixed with 250 µL of a 32% w/w aqueous solution of Iohexol, a common reagent in cell separation[26] to prevent cell sedimentation, resulting in a final Iohexol concentration of 8%.

4.10 Automated cell counting

For automated cell counting, cells collected from the system were transferred to a standard 96-well plate (if not already collected in a plate). The 96-well plate was then imaged on an automated live cell imaging system at 4x magnification using three colour channels. The colour channels used were red (excitation 575/28 nm), green (ex. 475/28 nm) and blue (ex. 395/25 nm). Exposure times were between 200 ms and 500 ms for the red and green channel, and between 200 ms and 800 ms for the blue channel, respectively. In the case of colour-based sorting, the cells were automatically detected by the system and assigned to the red target or green non-target population based on their fluorescence signal. This assignment was visually checked and verified on a random basis. In the case of morphology-based sorting, the images were evaluated by visual inspection following assignment of the cells to one of the two classes.

4.11 Viability tests

4.11.1 Determination of cell viability

A Jurkat cell suspension with a cell concentration of $1*10^6$ cells mL^{-1} was divided into two aliquots of 1.5 mL each. One aliquot was stored in a 5 mL reaction tube at room temperature while the second aliquot was flushed through the microfluidic system (PROC2 chip). The flow rates used were 25 µL h^{-1} (sample inlet), 5 µL h^{-1} (buffer inlet), 10 µL h^{-1} (waste outlet) and 300 µL h^{-1} (sheathflow). For the sheath flow, the conditioned cell culture medium was used in this experiment (see section 4.9.2). Furthermore, the same electrode voltages were used as in the case of sorting cells (see chapter 4.8).

Due to the sheath flow in the system, the cell concentration of the second aliquot after passing the system was significantly lower than in the original sample. To compensate for this dilution effect and to adjust the cell concentrations of the aliquots, the first aliquot stored at room

temperature was also diluted with conditioned cell culture medium. The final cell concentration of both samples was approximately $4*10^4$ cells mL^{-1}.

Then 1.1 ml of each sample was mixed with 110 µL of the reagent of a cell proliferation assay. 110 µL of this mixture was added to each of 8 wells of a 96-well plate and incubated for three hours at 37°C and 5% CO_2. Subsequently, the absorbance at 450 nm was determined for each well using a photometer and the values of the wells of each sample were background-subtracted and averaged.

The rest of both samples was incubated in T25 cell culture flasks at 37 °C and 5% CO_2 and used to repeat the measurements on the two following days.

4.11.2 Determination of cell growth

Parallel to the absorbance measurements, the cell concentration of both samples was determined. For this purpose, two Luna Cell Counting slides were filled with 100 µL of each sample. The filled chambers were photographed at 10x magnification in phase contrast on the second microscopy setup, resulting in 20 images per sample.

Using a Python script written by Neus Godino, the cells were automatically detected and counted. The results of this process were visually validated. Based on the size of the image section and the known height of the counting chamber used, the cell concentration was determined.

4.12 Fabrication of bubble traps & sample reservoir

A Computer-aided design (CAD) was created for each of the self-made components. The components were milled from Poly(methyl methacrylate) (PMMA) and were manually finished. The dimensions of the components are shown in Figure 17.
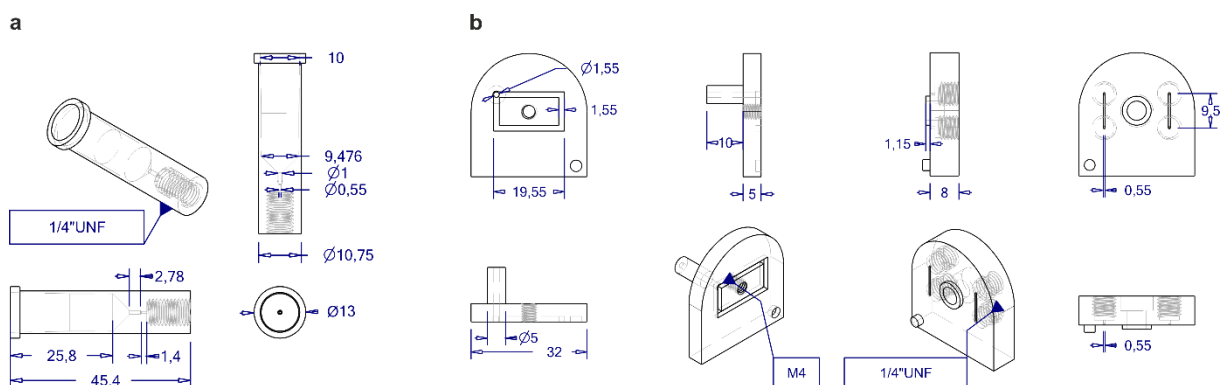

Figure 17: Dimensions of the self made components. Dimensions in mm for the sample reservoir (**a**) and the bubble traps (**b**). In collaboration with Erik Hahn.

4.13 Rapid prototyping

During the development and optimisation of the rapid prototyping process, a large number of parameters were tested. The protocol described here lists the optimised final parameters used to produce microfluidic chips at Fraunhofer IZI-BB.

4.13.1 Substrate cleaning

The substrates (slides with dimensions 75 x 38 x 1 mm) were cleaned with a Hellmanex III solution (2% in H_2O), ethanol and ultrapure water as well as an ultrasonic bath. The cleaning protocol consisted of the following steps:

- 10x washing with ultrapure water,
- 15 min ultrasonication at 100% in ultrapure water,
- 10x washing with ultrapure water,
- 15 min ultrasonication at 100% in ultrapure water,
- 10x washing with ultrapure water,
- 15 min ultrasonication at 100% in Hellmanex solution,
- 10x washing with ultrapure water,
- 15 min ultrasonication at 100% in ultrapure water,
- 10x washing with ultrapure water,
- 15 min ultrasonication at 100% in ultrapure water,
- 10x washing with ultrapure water,
- 15 min ultrasonication at 100% in ethanol, followed by storage in ethanol.

4.13.2 Metallisation

The purified substrates were activated for 2 minutes in an O_2 plasma. A Thermal Resistance Evaporation System was used to evaporate a 5 nm layer of chromium and a 200 nm gold layer.

4.13.3 Photolithography

For the application of the positive photoresist a spincoater was used. The substrates were spin coated at 2000 rpm and an acceleration of 4000 rpm s^{-2} for 30 seconds. For a subsequent softbake step, they were placed onto another glass slide (75 x 75 x 1 mm), and baked for 2 minutes at 100 °C on a hot plate. The structuring of the photoresist was carried out with a laser exposer with the following parameters: Writemode III, laser power 25 mW, exposure time per pixel 100 %, energy mode 1 x 1. The photoresist was developed in the immersion bath for 20 s (developer diluted 1:4 in H_2O). The etching steps were also carried out in immersion baths for 200 s (gold) and 10 s (chromium). Between each development and etching step, the substrates were rinsed with water. For the removal of the remaining photoresist and the final cleaning of the substrates, they were immersed in NaOH (3%) for 5 min and then dried with N_2 or stored in ethanol (>99.9%).

4.13.4 Assembly

A biocompatible double-sided adhesive was cut using a cutting plotter to create the channel structure. The holes for the fluidic connections were drilled into the slides with a handheld drill at 5000 rpm equipped with a diamond drill head (diameter 1.6 mm). PMMA blocks were milled and glued to the holes with the biocompatible double-sided adhesive. For electrical contacting, angled pin bars were glued to the already joined chips using silver conductive lacquer and ultraviolet (UV) adhesive. The UV adhesive used was irradiated for 3 min with a UV lamp to cure the adhesive. The entire assembly of the chips from individual parts was done by hand.

4.14 Cell deflection experiments

On the second microscopy setup, the deflection behaviour of the electrodes at different voltages and flow rates was investigated using syringe pumps instead of pressure-based pumps. Images were taken in phase contrast mode at 20x magnification and 1 ms exposure time. Subsequently, the images were analysed using ImageJ, Microsoft Excel and manual counting. Fit curves were generated using OriginPro based on the error function

$$y = A * \text{erf}\big(k(x - x_0)\big) + y_0 \tag{13}$$

For a better fit, two auxiliary points were used: 0% deflection at 0 V and 100% deflection at 7 V.

5 Results

The aim of the work was to develop a novel DEP -based microfluidic system for image-based sorting of cells. In the following, the collected results are divided into four individual sections. These are (i) the development of the microfluidic chip and its mode of operation, (ii) the results of various sorting experiments under different conditions, (iii) the investigation of cell vitality and (iv) various preliminary experiments. The latter include the characterisation of the cell flow through the system and the development of the peripheral fluidic components.

Chapter 5.1 first presents the design of the central microfluidic channel and the operation of the newly developed DEP-based sorting principle. The Python scripts, which are crucial for the functionality of the system, are also discussed here.

The sorting performance of the system is presented in chapter 5.2. Here, the influence of different sorting principles, different image information as well as different magnifications on the effectiveness of the sorting is investigated and the results are compared with theoretical calculations.

Chapter 5.3 shows the results of the vitality studies carried out.

Chapter 5.4 covers preliminary tests and shows results collected during the characterisation of the microfluidic system. Here, the deflection of the cells by the electric fields is presented as a function of various parameters, as well as the influence of the electric fields on the cell velocity and position.

Finally, the functioning of the bubble traps and the sample reservoir is explained in chapter 5.5.

5.1 The microfluidic system

The microfluidic system developed in this work consists of several subunits that fulfil different tasks. The central, newly developed components are explained below.

5.1.1 Microfluidic chip design

The central element of the system developed in this work is a microfluidic chip that had to be integrated into an existing interface. This interface defined a series of framework conditions. In addition to the materials used, these include in particular the external dimensions and the basic structure of the chip. For details on the interface, see section 4.1.1.

Essentially, the microfluidic chips consist of two glass plates of different thicknesses, which are separated by a 35 µm thick polymer spacer that forms the microchannel. In addition, there are congruent electrode structures made of platinum on the inside of both glasses, which can be used to generate the electrical fields required for DEP. A glued-on metal plate with slots for microscopy increases the stability, reduces the risk of breaking and dissipates the heat generated during experiments.

While the total available chip area was limited due to the interface, both the channel structure as well as the shape and arrangement of the electrodes could be designed relatively flexibly.

Based on theoretical and practical considerations, as well as preliminary experiments (see chapter 5.4), a chip design was created.

The channel structure consists of a 650 µm wide channel that extends over the entire length of the microchip. On one side of this channel, it splits into two smaller channels, each 300 µm wide, leading to two of the eight inlets and outlets of the structure. While one of the two inlets is intended for the introduction of the cell suspension, additional cell culture medium can be pumped into the channel through the second inlet. By varying the two flow rates applied to the inlets, the cell density and thus the average cell distance in the central channel can be varied without the need to change the sample. The central channel also ends in two narrow channels that lead to two different outlets. They are intended for the extraction of the target cells and waste cells. In both channels, a symmetrical sheath flow can be created by two additional inflows that flow crosswise into these two channels. This increases the flow volume and thus the flow velocity and, especially in the case of the target cells, ensures that the cells are flushed out quickly and reliably from the system. A schematic of the channel structure is shown in Figure 18.
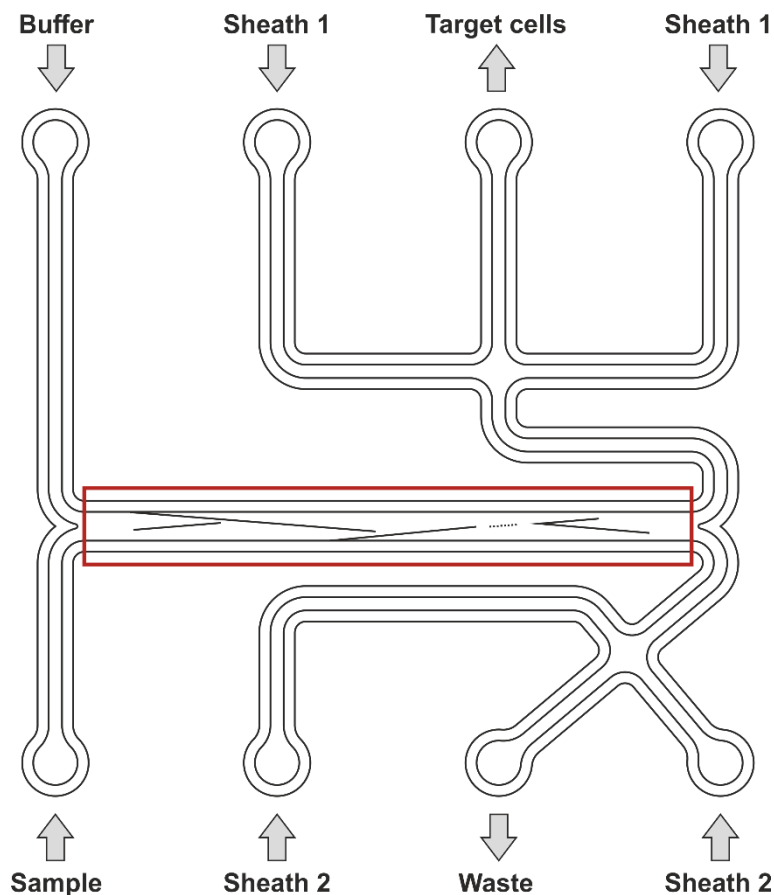
Figure 18: Overview of the channel structure of the PROC2 chip design. The cell sample and a buffer solution are introduced into the chip through the two narrower channels on the left in variable proportions. While flowing through the central channel (red rectangle), sorting takes place. At the end of the central channel, it branches into two channels. The target cells are diverted into one of the branches and are expelled from the chip with the help of a sheath flow. Waste cells leave the chip through the other channel; a sheath flow can also be applied here as needed.

The arrangement of the electrodes along the central channel was chosen to meet various requirements. First, the cells flowing into the channel must be deflected in such a way that they are lined up in a kind of pearl-chain configuration. This is to be ensured by electrodes E1 and E2. Electrode E0 is used to pre-focus the cell sample in case of a possible inverted operation of the chip, where the entries of sample and buffer are swapped. Adjacent to the focusing electrodes is a 200 µm long area without electrodes. This is intended for interference-free imaging of the cells flowing through it. Immediately following this is an array of eight individual short electrodes (labelled E3). It is used for sorting target cells and is described in detail in section 5.1.3. After the sorting array, there is another 200 µm long electrode-free area for any necessary post-sorting imaging, before a separation electrode (E4) further separates sorted and unsorted cells and directs them to the different outlets. A microscopic image of the central channel is shown in Figure 19.

The electrode structures extend over the entire length of the central channel. The reason for this extension is the optimisation of the throughput: for this purpose, the highest possible flow velocities are necessary in the system. Since the deflection of the cells depends, among other factors, directly on the angle at which the electrodes are tilted relative to the direction of flow of the liquid, it is desirable to have the smallest possible angle (see sections 3.3.2 and 5.4.2). However, reducing the angle while maintaining the channel width requires a longer electrode structure and thus a longer channel. As a compromise, an electrode angle of 5° was chosen to make the most efficient use of the limited space available on the microchip.

Figure 19: Microscopic image of the PROC2 main channel. Electrodes are labelled according to the main text. The scale bar represents 500 µm.

5.1.2 Microfluidic periphery

Outside the microfluidic chip, the fluids used were passed through standard microfluidic tubing (see chapter 4.2). A distinctive feature are the pressure-based pumps, which are used instead of the conventional syringe pumps. These regulate the flow rate by applying air pressure to a reservoir. A flow sensor built into the supply tubing measures the actual flow rate, based on which the pumps automatically adjust the pressure. The advantages of these pumps for the developed system are the simplified bubble-free filling, the easier exchange of the liquids used and the larger volume that can be used with the same flow accuracy compared to conventional syringe-based pumps (up to 50 ml). In this way, long experimental times of up to nine hours could be realised (data not shown).

Other special elements developed during the development of the system are so-called bubble traps and a unique sample reservoir. These are addressed separately in chapter 5.5.

5.1.3   Functionality of the microchip and dielectrophoretic sorting principle

For the functionality of the microfluidic chips, the electrode structures described are essential in addition to the fluidic components mentioned. In order to generate the electrical fields necessary for interaction with the cells flowing through the channel, the individual electrodes can be selectively controlled and assigned a square-wave potential of up to 10 volts peak-to-peak. For this purpose, proprietary signal generators were used (see chapter 4.4).
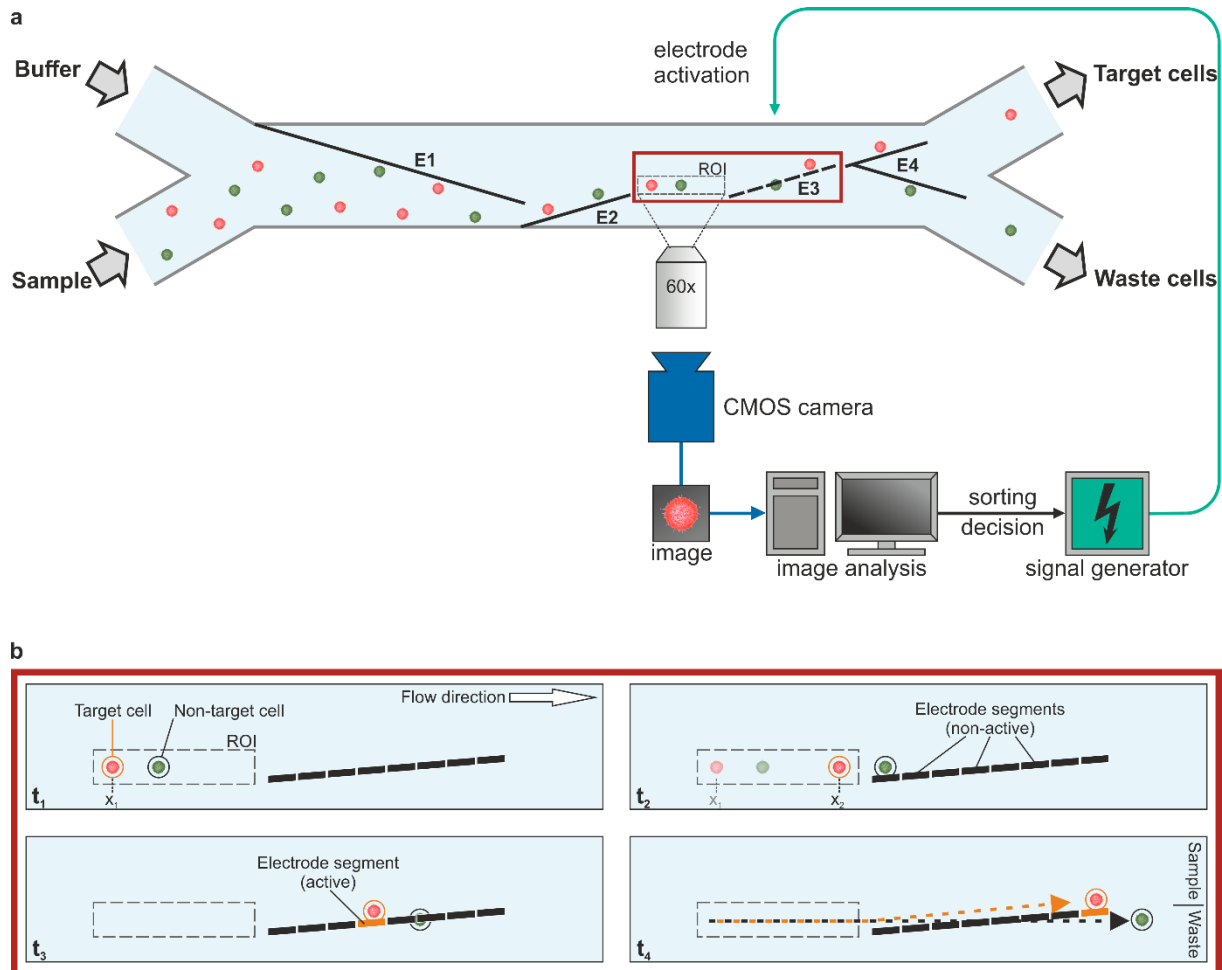

Figure 20: Schematic overview of the DEP sorting principle. a, Top view of the microchannel. Both bottom and cover glass of the channel are equipped with congruent electrode structures (black lines). Cells flowing through the channel can pass through them unhindered as long as no voltage is applied. As soon as a voltage generates an electric field between the electrodes, this acts as a barrier for the cells and they are deflected from their original trajectory. A cell sample containing target and non-target cells (shown in red and green) is introduced into the channel through the sample inlet. Buffer is simultaneously pumped into the channel through the second inlet, preventing contamination of the target cell outlet with debris from the sample inlet. The electrode pairs E1 and E2 deflect the cells so that they flow through the ROI (red rectangle) in a pearl chain configuration. Here, a CMOS camera takes pictures of the cells, which are searched for target cells by an algorithm. The flow velocity of detected target cells is determined from the images, which is then used to selectively switch the eight individual electrodes of the sorting array E3 on and off. After the sorting process, the two cell populations are further separated by electrode E4. Target cells are directed into the target cell outlet from where they are brought into a sheath flow, while non-target cells are removed by the waste outlet. **b**, Schematic of the ROI and operation of the sorting array E3 (red rectangle). t_1: Non-target cells and target cells reach the ROI one after the other in a pearl chain configuration. t_2: The position of the target cell is tracked over several images and time points and its speed is calculated. Non-target cells can pass through the inactive electrodes of the sorting array unimpeded. t_3: Based on the calculated velocity of the target cell, individual electrodes of the sorting array are sequentially activated and the target cell is deflected. t_4: Subsequent electrode segments are sequentially activated to achieve complete separation of the cells.

For the sorting of cells, electrodes E1 and E2 are permanently supplied with voltage as default, so that cells flowing through the channel take on the above-mentioned pearl chain configuration and flow successively through the free area (region of interest, ROI) next to electrode E2. Here, a high-performance camera takes several images of each cell flowing through the channel via high-resolution microscope optics (up to 60x magnification). These images are analysed by an algorithm that essentially distinguishes between target and non-target cells and determines the velocity of the target cells. Details of the algorithms used can be found in chapter 4.7.

Based on the computer-assisted evaluation, a sorting decision is made automatically and the electrodes of the sorting array E3 are switched on and off. The activation is sequential and coordinated with the calculated velocity of the cells, so that only the part of the array on which the target cell is located is active. In this way, the length of the sorting window can be minimised. The operation principle of the sorting array is shown in Figure 20. In order to reliably flush the cell populations sorted in this way into the two different outlets, electrode E4 is also permanently active to ensure further separation of the cells. While non-target cells are flushed directly out of the chip through the waste outlet, the target cells are first introduced into a sheath flow, which is then used to drive them out of the chip. For details on the sheath flow configuration, see Figure 12 on page 26.

5.1.4 Python Scripts

For the sorting mechanism described above, an automated image evaluation and generator control is essential. In the context of this work, various modifications of a Python script were used, all of which were written by Neus Godino. The basic version of the Python script used can be divided into three main functional blocks: (i) frame reading, (ii) frame analysis (including cell detection, cell tracking and sorting decision) and (iii) generator control. Frame reading and generator control are relatively simple processes that hardly require any adjustments between experiments. The frame analysis, on the other hand, is the largest and most complicated part of the script. This module also had to be repeatedly adapted to the respective experimental conditions, which is why it is discussed in more detail below.

The first step of frame analysis is cell detection. The script searches for cells in a given ROI based on colour and/or brightness values. Each cell found in this way is assigned an identification number (ID) and a value for its size, position and time point of the frame acquisition. The values are stored in a database.

The script repeats this process for each frame. Cells that have already been found in previous frames are not assigned a new ID, but the database entry is extended by the new position values. This is called cell tracking. As soon as a cell can no longer be tracked, for example because it flows out of the ROI, the flow velocity of the cell is calculated using the stored data.

Simultaneously, the sorting decision is made based on the collected data and cell classification. In the case of sorting membrane-stained cells, classification is done using the brightness profiles of several radial profiles (for details see chapter 4.7). In the case of sorting red and green cells, however, the sorting decision is made automatically during tracking, as only target cells of the corresponding colour are tracked. Based on this sorting decision and the calculated cell velocity, the electrodes of the sorting array are then switched sequentially. For the position-based sorting

(see section 5.2.5), the ROI was located above the electrodes, eliminating the need for a velocity calculation.

Parallel to the sorting process, the analysed frames are displayed on the screen in real-time with different overlays. The overlays include the analysed ROI, the cell IDs and a red highlight of active electrodes (see Figure 22 on page 44). In another parallel operation, all frames are compressed into a video and saved. In addition, the saved parameters of the tracked cells including the calculated flow velocity are stored in a text file.

Before the respective script is executed, various parameters can be set for the sorting process. With regard to image acquisition, these include the size of the observed and analysed frame sections, the frame rate and exposure time of the camera as well as the displayed and analysed brightness range. With regard to sorting, the target cell colour as well as a delay factor can be set to optimise the sorting process. In addition, the voltages applied to the electrodes can be set separately for each electrode.

For the analysis of the sorting process, another script was developed that allows re-evaluation of videos recorded during live sorting. With this script, the proportion of (in-) correctly deflected (target) cells was determined by automatically counting all cells present in the video in the area behind the sorting array (E3) and assigning them to a population based on their colour. The delays in the execution of the script due to the higher performance requirements are not relevant, as the analysis did not have to take place in real time.

5.2 Sorting performance of the microfluidic DEP chip

5.2.1 The velocity-based sorting principle

In a first series of experiments, the function of the proposed velocity-based sorting principle described above was investigated. For this purpose, a cell sample was prepared as described in section 4.9.3, consisting of 10% red stained target cells and 90% green stained non-target cells. This cell sample was flushed through the system at a flow rate of 40 µL h^{-1} and passed through the ROI, which was located immediately in front of the eight electrodes of the sorting array. At 6.4x magnification, several images of each cell were taken as they flowed through the ROI. These images were analysed in real time by a Python script. The script identified target cells by their colour and stored the time of the image acquisition as well as their respective position. From this data, the velocity of each target cell was then automatically determined and its position at each point in time could be predicted. This prediction was used to selectively activate the electrodes of the sorting array individually as soon as the target cell was anticipated at the corresponding electrode. No analysis of the non-target cells took place during the experiment, meaning they were not included in the decision-making of the sorting algorithm. Consequently, the system was operated in "yield sorting" mode (see section 3.5.1).

While unsorted cells were extracted through the waste outlet, all sorted, i.e., deflected, cells were brought into the sheath flow through the target outlet, flushed out of the system and collected into a 96-well plate. The collected cells were then counted automatically using an automated live-cell imaging system and the target cell concentration achieved determined on the basis of their colour (see chapter 4.10). This experimental procedure was repeated on several days with different cell concentrations and thus different throughputs, sorting for at least half an hour at each condition.

In addition, not only the area of the ROI but also the area along the sorting array was observed and recorded on video throughout the experiment. The recording of the experiment allowed a subsequent evaluation of the sorting process. In this way, the correct functioning of the sorting principle could be verified. An image sequence of a sucessful sorting of a target cell is shown in Figure 22 on page 44. Furthermore, with another Python script, the proportions of true positive cells (i.e., correctly deflected red cells), true negative cells (correctly undeflected green cells), false positive cells (incorrectly deflected green cells) and false negative cells (incorrectly undeflected red cells) could be automatically determined on the basis of the cell position behind the sorting array.

The target cell purities determined from the extracted cells ranged from 93% at approximately 2200 cells h^{-1} to 71% at approximately 8500 cells h^{-1}. The determined values decrease towards higher throughputs (i.e., cell densities) and thus essentially follow the theoretically possible purity, which is determined by the stochastic occurrence of single or multiple cells on the sorting electrodes (see Poisson statistics in the appendix).

The evaluation of the videos showed a similar result, here the overall purities were slightly lower on average (between 91% at approx. 2200 cells h^{-1} and 68% at approx. 8500 cells h^{-1}). The entire data set is shown in Figure 21.

Based on the percentage of correctly sorted cells determined in the videos and the number of collected cells counted in the well plate, the rate of recovered cells could be determined. In the case of the velocity-based yield sorting described here, 1177 of 1277 sorted target cells were recovered, resulting in a recovery rate of approximately 92%.
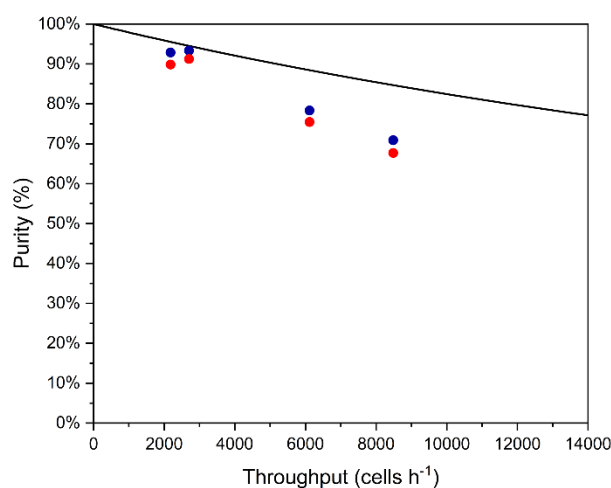

Figure 21: Results of the velocity-based sorting at 6.4x magnification. Determined target cell concentrations after flushing the cells out of the system are shown in blue, concentrations determined from the video data are shown in red. The black line shows the theoretical optimum according to Poisson statistics.
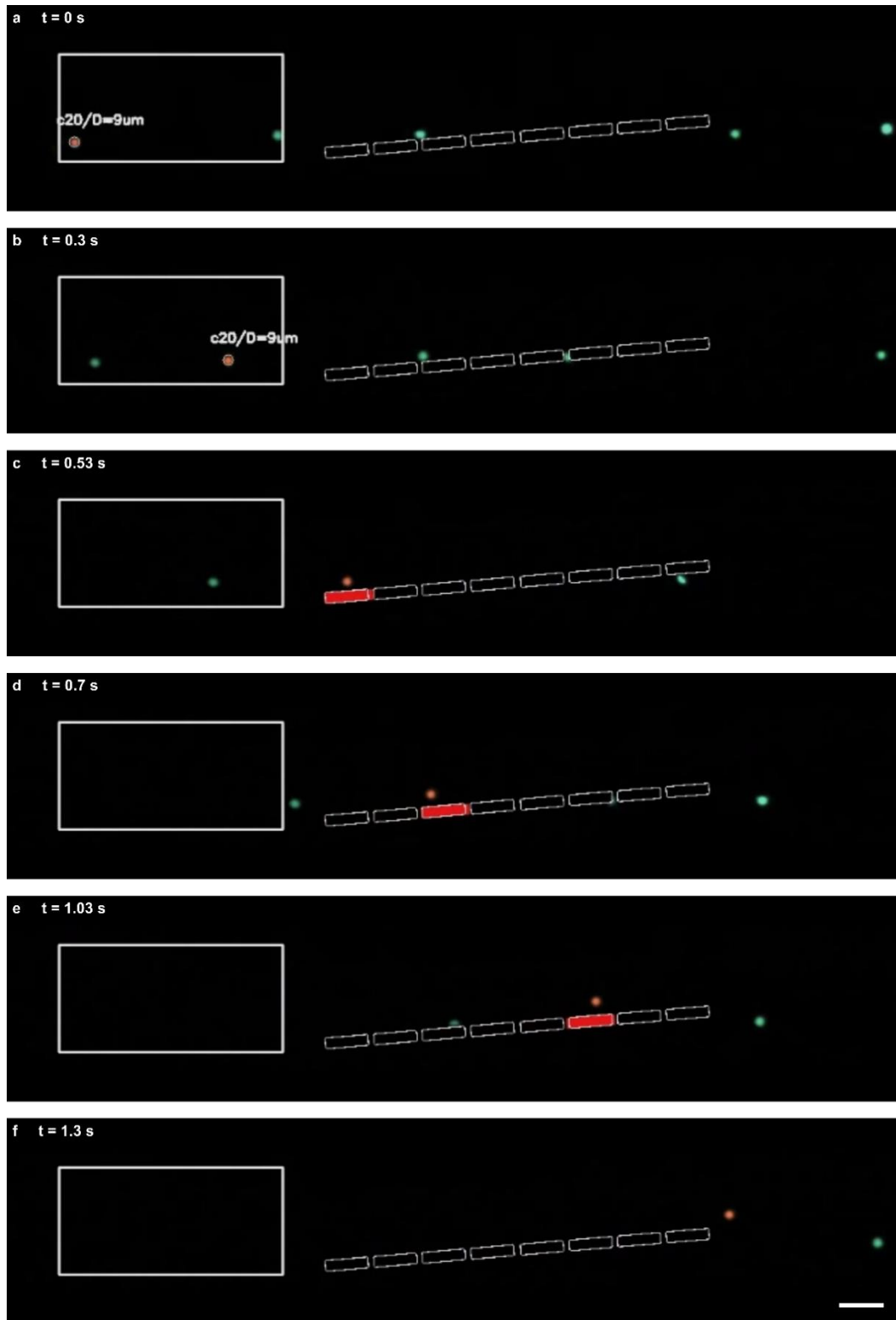
Figure 22: Real-time images of the velocity-based sorting process. The figure shows post-processed individual frames from a video recorded during cell sorting. **a**, A Python script detects a target cell (red) at the left edge of the ROI (large white rectangle). The individual electrodes of the sorting array (small white rectangles) are inactive so that non-target cells (green) can flow through unhindered. **b**, The target cell is detected at several positions of the ROI and its respective position as well as the recording time of the frame are saved. Non-target cells are ignored. **c**, Based on the position data, the velocity of the target cell is calculated and as soon as the target cell is suspected there, the first electrode segment is activated and coloured red in the video. **d** & **e**, Further electrode segments are activated one after the other, the previous segments are switched off as soon as the target cell is expected at the next electrode. **f**, Arriving at the end of the electrode array, target cells and non-target cells are fully separated. The scale bar represents 50 µm.

44

5.2.2 High-resoultion colour- and velocity-based sorting

In order to fully utilise the possibilities of image-based sorting, more detailed imaging of the cells to be sorted is highly demanded. For that, the previously conducted experiment was repeated at 60x magnification. Due to the high magnification, the reduced field of view allowed observation of only the ROI but not the sorting array. Consequently, a subsequent analysis of the sorting process based on video data was not possible.

Again, a cell sample was prepared, consisting of 10% red stained target cells and 90% green stained non-target cells and flushed through the system at a flow rate of 40 µL h^{-1}. In this case, target cells were again automatically identified and sorted by their colour using a Python script. As before, only target cells were analysed and tracked and the system was operated in "yield sorting" mode.

All sorted cells were collected in a 96-well plate, counted automatically and the target cell concentration was determined. Exemplary images of a cell sample sorted and counted in this way before and after the sorting process are shown in Figure 23. The experiment was repeated on several days with different cell concentrations (i.e., different throughputs), sorting for at least one hour at each condition.

Depending on the throughput, different target cell purities were achieved. These ranged from 95% at approximately 2000 cells h^{-1} to 72% at approximately 12000 cells h^{-1}. The values determined drop off towards higher throughputs and thus essentially follow the theoretically possible purity determined according to Poisson statistics. With one exception, the data points all lie slightly below this curve. An overview of all purities achieved as a function of the respective throughput is shown in Figure 23.
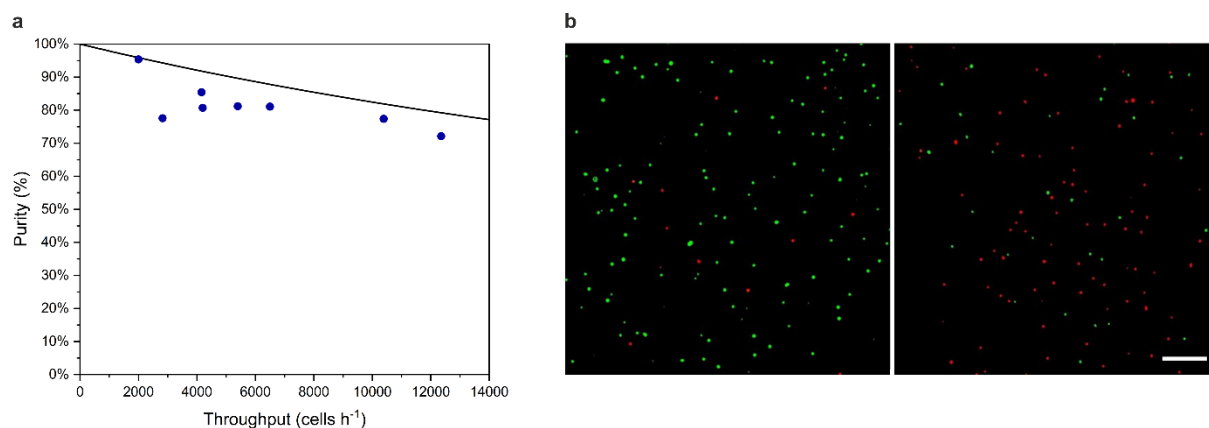

Figure 23: Evaluation of the colour- and velocity-based sorting performance at 60x. a, Determined target cell concentrations of the cell suspension after colour-based sorting at 60x magnification. The black line indicates the theoretically achievable purities according to Poisson, while experimental results are shown as blue dots. **b**, Exemplary images of a cell suspension before (left) and after (right) sorting for red stained cells by the developed system at a throughput of approximately 12000 cells h^{-1}. The length of the scale bar is 200 µm.

5.2.3 High-resoultion morphology- and velocity-based sorting

The next step was to demonstrate the system's ability to sort cell samples based on their morphological characteristics instead of pure colour information. For this purpose, a sample

was prepared with 10-20% target cells stained with a membrane stain and 80-90% cytosol-stained non-target cells, both stained with the same colour (red). In addition, the target cells were cytosol stained in green and the nuclei of the non-target cells were stained in blue for better differentiation in the analysis step after sorting. However, these additional stains were not considered in the sorting decision, which was only based on the light emitted by the cells in the red spectral range. Hence, a differentiation was only possible on the basis of morphological information. Details on the sorting decision and the cell staining are described in chapter 4.7 and section 4.9.3, respectively. The algorithm used was adapted accordingly, but the observed ROI remained the same as in the previous experiment.

Again, the cells were flushed through the system at a flow rate of $40\,\mu L\,h^{-1}$, analysed automatically and the electrodes were switched automatically. However, in addition to simply identifying the target cells and determining their velocity, the algorithm in this case also examined whether non-target cells or other contaminants appeared in the immediate vicinity of the target cells. Target cells that were too close to these other objects were excluded from the sort, i.e., it was a "purity sort" (see section 3.5.1).

The target cells were flushed from the system as described above, but in this case were classified user-based on their green and blue staining. This experiment was also repeated several times on different days for at least half an hour at different throughputs. The purities achieved are listed in Table 1. Again, a decrease in purity with increasing throughput was observed. Only the data point with 61% purity at a throughput of 1491 cells h^{-1} clearly deviates from this trend and the other values.

Table 1: Experimental data of the morphology-based real time cell sorting.

Throughput (cells h^{-1})	Processed cells		Target cell concentration		Enrichment factor
	overall	target	initial	final	
1206	1069	214	20.0%	83.0%	4.1
1491	1341	108	8.1%	61.0%	7.6
2789	1229	248	20.2%	82.2%	4.1
3960	3467	240	6.9%	82.6%	11.9
7692	6902	645	9.3%	76.5%	8.2

5.2.4 Practical application of DEP-based sorting

Together with the Biomedical Optical Microscopy, Nanoscopy and Interferometry Research Group (OMNI Group) of Natan T. Shaked at the University of Tel Aviv, DEP-based sorting was used to separate cancer cells from a mixed cell population. For this purpose, a previously designed DEP microchip with a different electrode configuration was combined with an interferometric phase microscopy system developed by the group.

The interferometric method used is known as quantitative phase microscopy. Its special feature is that the images taken with it are holograms. From these holograms, the 2D distribution of the projected refractive index can be determined and thus intracellular structures (e.g. the cell's

nucleus) become visible without staining. Although the method is label-free, staining of the cells was implemented to enable subsequent validation of the sorting experiment.

The automatic analysis of the holograms obtained from the cells flowing through the chip was not performed by a Python script as usual, but by a Matlab script written by Matan Dudaie. Before the experiments, this script was trained using machine learning based on pure and known cell samples so that it could distinguish cancer cells from healthy blood cells. In addition to classifying the cells, the script also controlled the signal generators and thus the sorting process.

The DEP chip used for the experiments featured a channel structure and electrode arrangement that deviated from the geometry described in section 5.1.1, so that the sequential sorting principle could not be applied. Instead, a V-shaped electrode was used for sorting together with one electrode to the right and one to the left. However, upstream focusing electrodes were also present in this microchip. A schematic of the microchip used is shown in Figure 24.

In the experiments conducted, cell mixtures of HT29-GFP cells (colon adenocarcinoma, GFP expressing), SW-480 (colon adenocarcinoma), SW-620 (metastatic stage of colon adenocarcinoma from the lymph node) on the one hand and erythrocytes, monocytes, lymphocytes and granulocytes from a blood sample on the other hand were pumped through the microchip at up to 20 µL h^{-1}. The sorting was evaluated using the video recordings of the sorting process. A label-free classification with an accuracy as high as 98.9% for cancer cells from blood cells was achieved. With the DEP chip used, 69.2% of the identified target cells were correctly sorted.
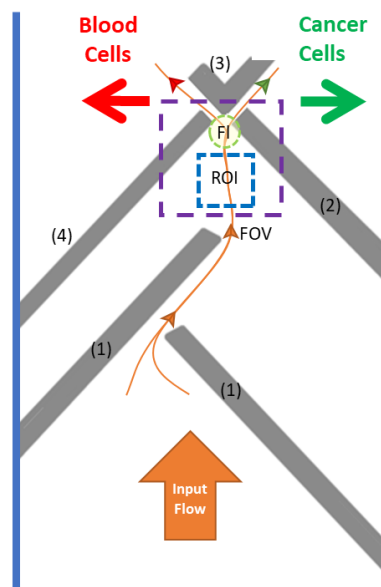

Figure 24: Overview of the DEP microchip used for holography-induced sorting (schematic, not to scale). Cells flowing through the channel (blue lines) are deflected by two electrode structures (1) and brought into a pearl-chain configuration. They then enter the ROI (blue rectangle) within the field of view (purple rectangle) one after the other. Depending on the sorting decision based on the images taken here, either electrode (2) or electrode (4) is activated to deflect the cells to the left or right. Deflected cells are further separated from each other by the permanently active v-shaped electrode (3). Fluorescence images from the FI-labelled region can be used to monitor the label-free real-time classification process. Taken from[148].

5.2.5 Colour- and position-based sorting

The mode of operation of the sorting algorithm described in section 5.1.3, in which the cell position is predicted from the calculated velocity of the respective cell, is potentially inaccurate due to this prediction. In order to detect any errors resulting from this, the experiment was repeated, but the ROI was changed so that in this case it extended over all eight electrodes of the sorting array at 6.4x magnification. Based on the camera's image information, an electrode of the array was activated whenever a red target cell was located directly on one of the electrodes. The python script was adapted accordingly. Green non-target cells were ignored, the system was operated in yield sorting mode.

Again, a cell sample with 10% target cells (red) was flushed through the system at 40 µL h^{-1} and sorted. The extracted cells were counted automatically and the achieved target cell concentration was determined. The recorded videos were automatically evaluated and the proportion of true positive cells, true negative cells, false positive cells and false negative cells was determined.

This experiment was repeated on several days at different throughputs, sorting for at least half an hour at each condition.

Depending on the throughput, target cell purities between 88% at approximately 650 cells h^{-1} and 76% at approximately 6000 cells h^{-1} were obtained. The values determined scatter relatively strongly, but are all slightly below the theoretically possible purity according to Poisson statistics.

The evaluation of the videos showed similar results, but the values determined are less scattered. In addition to this, the purities are higher on average (between 95% at approx. 650 cells h^{-1} and 72% at approx. 6000 cells h^{-1}). With one exception (97% at approx. 2400 cells h^{-1}), however, all the values achieved in this case are also below the theoretically achievable values. The entire data set is shown in Figure 25.

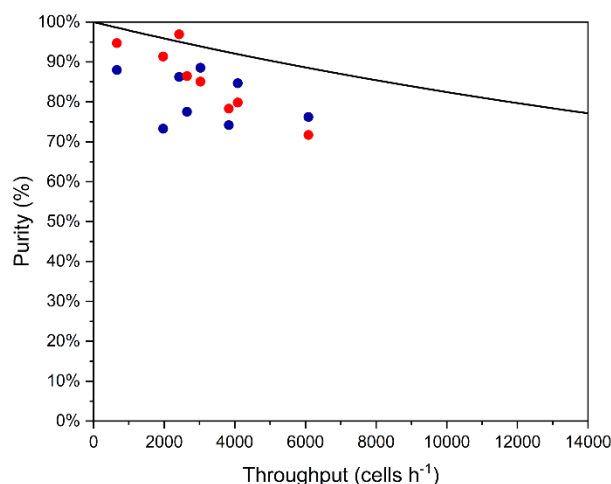The recovery rate in this series of experiments was approximately 76% (1708 of 2250 sorted target cells).

Figure 25: Experimental results of the position-based sorting at 6.4x magnification. Determined target cell concentrations after flushing the cells out of the system are shown in blue, concentrations determined from the video data are shown in red. The black line shows the theoretical optimum according to Poisson statistics.

5.3 Viability studies

The target cell population obtained by cell sorting is usually further utilised, for example in (bio-) production processes or therapeutic applications. In some cases, cultivation of the obtained cells may be necessary as well. It is therefore of high importance that the cells are not damaged and vital after the sorting process.

In order to test the biocompatibility of the system, a cell population was divided into two samples one of which was flushed through the system with active electrodes at 40 µL h^{-1}. The other sample was stored simultaneously at room temperature and served as a reference sample. Both samples were then incubated for two days. The cell count of each sample was determined on the day of the experiment as well as on the two following days. In addition, a WST-8 based cell viability assay was performed on both samples on each day. Details of this process are given in chapter 4.11. The entire experiment was carried out a total of three times within a few weeks.

The averaged results of all investigations are shown in Figure 26. The determined absorbance of all samples, normalised to the cell number, showed comparable values across all measurements with a slight increase over the observed days. While the cell count of the reference samples increased over the days, the growth of the sorted samples stagnated during the first 24 hours. However, these samples also showed a strong increase in cell count between the respective second and third measurement.
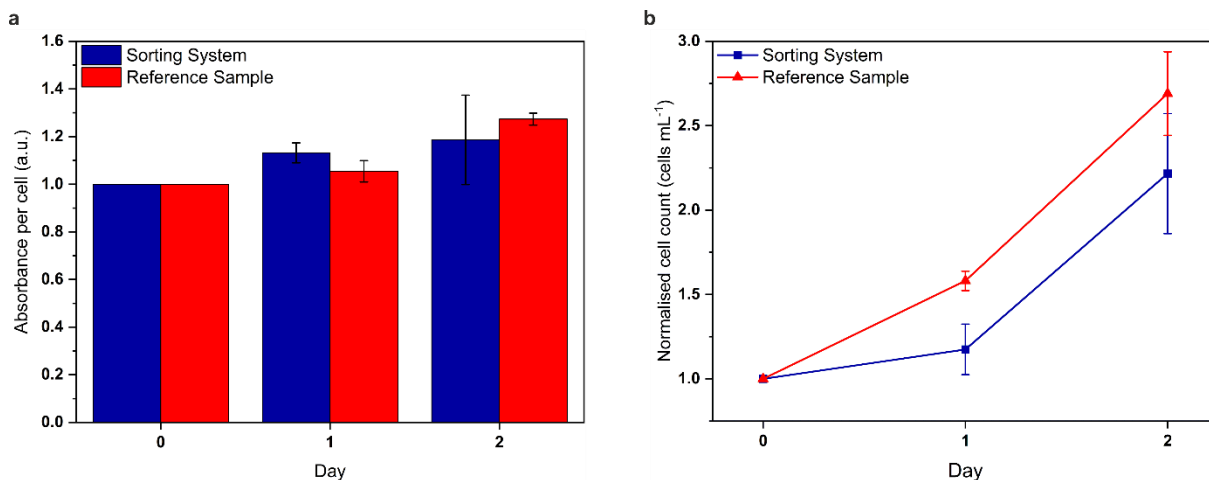

Figure 26: Cell viability of processed and unprocessed cell samples. a, Photometrically determined and normalised absorbance per cell after treatment with a commercially available tetrazolium salt-based cell viability assay over the course of two days. The blue data set shows the measurement results of a sample flushed through the system under standard sorting conditions, the red coloured data the measurement values of the reference sample. This sample was not processed in the microfluidic system, but otherwise treated in the same way. **b**, Normalised cell growth of the two samples shown in **a** over the course of the two days of experimentation. Results in collaboration with Nina Hupf.

5.4   Preliminary experiments

Before the final microfluidic chip design was completed, some theoretical assumptions such as the angle-dependent cell deflection efficiency were verified. For this purpose, a rapid prototyping procedure was first established, which allows the production of custom chips. In addition, existing chips were used for these experiments.

Before the final microchips were used for sorting cells, several characterisation experiments were carried out on them. These included the investigation of the flow behaviour of the cells within the central channel and the interaction of the cells with the deflection electrodes. The influence of the DEP electric fields on the velocity distribution and the resulting position of the cells inside the channel was investigated. In addition, combinations of flow rates and electrode voltages were tested to find parameters that allowed stable operation of the system.

5.4.1   Rapid prototyping

The creation of a microchip design is labour-intensive and time-consuming. In addition, the production takes a relatively long time and is carried out by external partners. Within the scope of this work, it was therefore not possible to test and optimise the design in several iterations. Instead, specific aspects regarding the channel or electrode structure were to be investigated in the short term before the final chip design was completed and commissioned.

To meet this challenge, a rapid prototyping process was established in-house. In this process, two microscopy slides were first cleaned and vapour-deposited with a gold layer. A layer of photoresist was applied by spin coating and a baking step, and then exposed using a laser direct writer. The exposure was carried out according to a self-created CAD pattern in order to produce specific electrode structures. Subsequently, the electrode structures were produced from the gold layer in a wet chemical etching process. In a next step, several holes were drilled in one of the slides for the subsequent connection of the fluidics. In parallel, a channel structure was cut out of a biocompatible double-sided pressure sensitive adhesive (PSA) using a cutting plotter. This was used to join the two slides and create a microchannel. In the final step, fluidic and electrical interfaces were attached to the microchip. A schematic overview of the rapid prototyping process is given in Figure 27 and a picture of a finished chip is shown in Figure 28 on page 52.

During the development of the process, the individual process steps and process parameters were optimised. These included (i) the cleaning protocol for the microscopy slides; (ii) the vapour deposition time for the application of the gold layer; (iii) the duration and speed of the spin coating; (iv) the duration and temperature of the baking steps; (v) the duration and strength of the laser exposure; (vi) the dwell times of the slides in various etching and cleaning solutions; (vii) the drill head, speed and feed rate during drilling; (viii) the handling of the slides and the adhesive during assembly; (ix) and the fabrication and application of the fluidic and electrical interfaces.

The microchips produced in this way were subsequently used to answer initial questions in preliminary experiments.
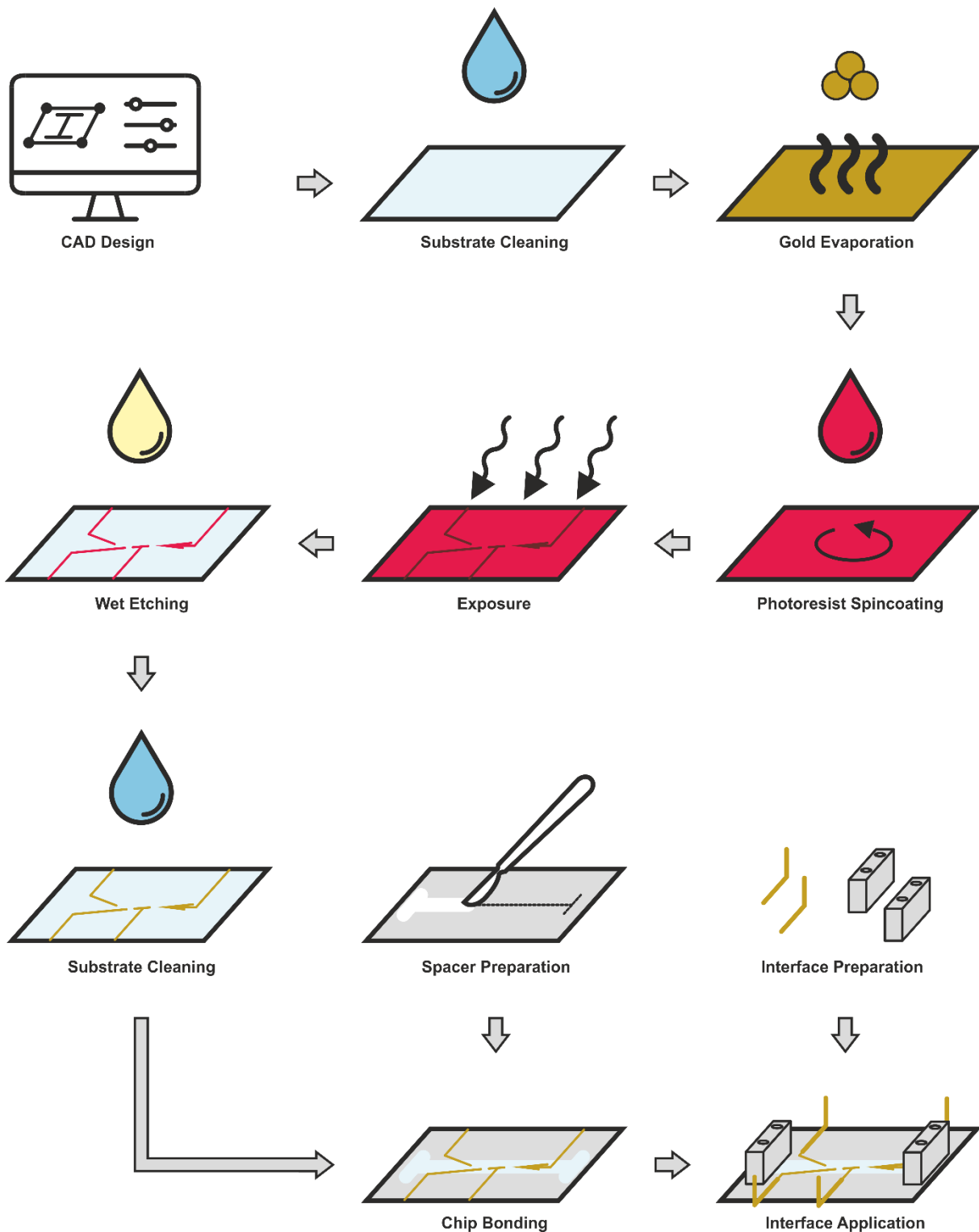
Figure 27: Schematic overview of the rapid prototyping process. Depicted are the individual process steps established in the context of this work.
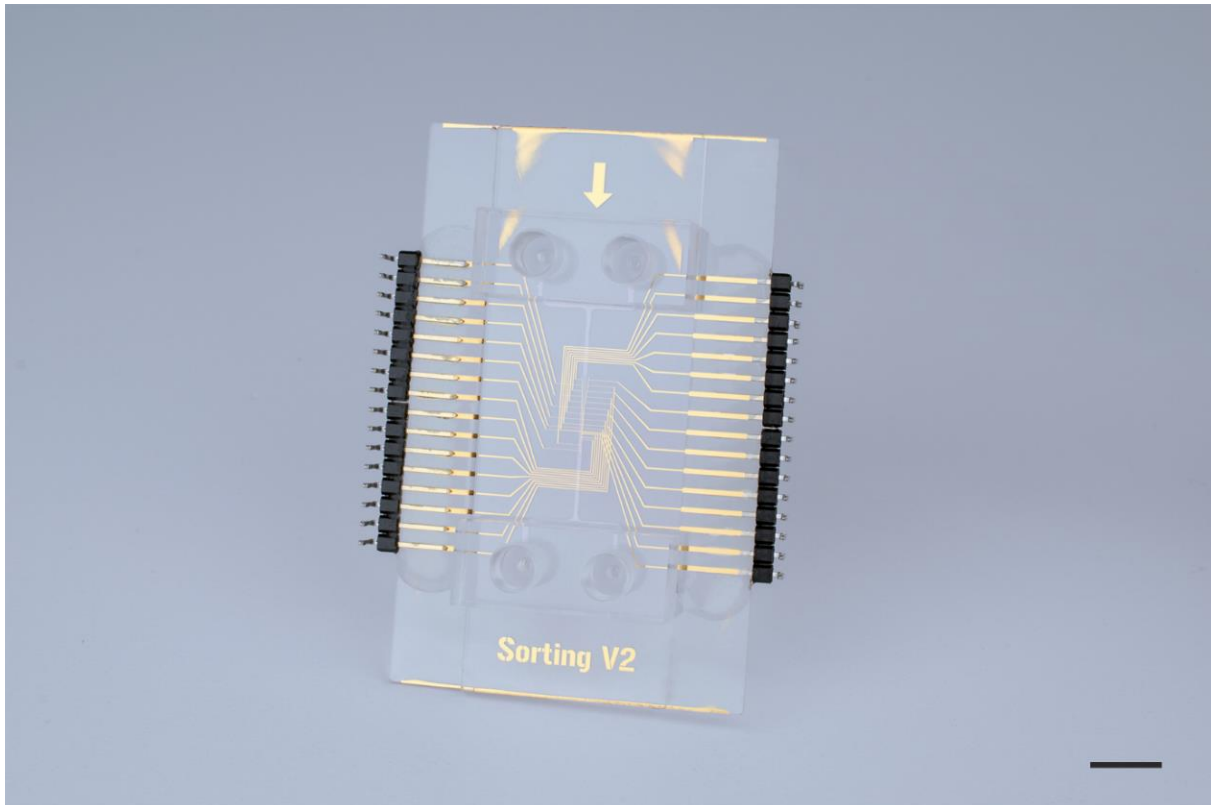
Figure 28: Photo of a microchip manufactured using the rapid prototyping process. The characteristic features of the chip are 1 mm wide and 50 µm high microchannels, up to eight individual inlets and outlets, sub 25 µm electrode structure sizes and up to 16 individually controllable electrode pairs. The scale bar depicts 1 cm.

5.4.2 Cell deflection as a function of electrode voltage and electrode angle

Particles flowing through the microfluidic chips experience various forces (see section 3.3.2). These are essentially the drag force caused by the fluid flow and the DEP force exerted by the electric fields on the electrodes. Due to the fact that the electrodes are positioned at an angle in the channel, the DEP force partially counteracts the drag force, which means that only a portion of the force is available for the actual deflection. This implies that the deflection should be more effective at low electrode angles, as less force is "lost". To test these assumptions, an existing microchip was used with electrodes positioned at angles of 3°, 8°, 15°, 22° and 45° in its channel. Polystyrene beads with a diameter of 10 µm were flushed through the channel, which was approximately 35 µm high and 700 µm wide, at fixed voltages between 1 V and 5 V, and the flow rate was increased until the particles broke through the electric field barriers. The maximum possible flow rates determined with complete cell deflection are shown in Figure 29.

5.4.3 Cell deflection as a function of electrode voltage and flow velocity

Cells that are not sufficiently deflected by the electric fields during their flow through the central channel, or even break through them, can have a negative impact on the functioning of the system. For example, they may collide with other deflected cells, flow past the ROI or end up in the incorrect outlet. To ensure reliable and stable operation of the microfluidic system, it was therefore of high importance to find a parameter combination with regard to the applied flow rates and electrode voltages at which the cells could be deflected reliably.
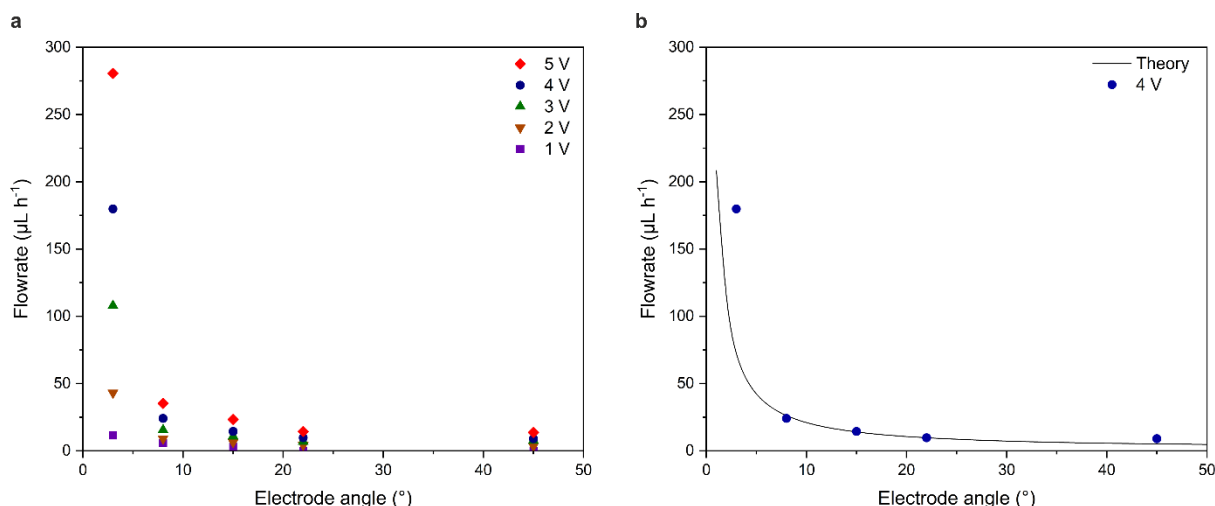
Figure 29: Maximum flow rates by electrode voltage. a, Maximum possible flow rates with complete cell deflection determined at angles of 3°, 8°, 15°, 22° and 45° and voltages between 1 V and 5 V without particles breaking through the DEP field barriers. **b**, Measurement data at 4 V from **a** with theoretically expected possible flow rates (black line). For the theoretical calculation, a $\sin^{-1}$ dependence of the flow rate on the electrode angle was assumed on the basis of geometric considerations and the measured value at 15° was selected as the starting point for the fit.

For this purpose, cells were flushed through the central channel. The flow rate was varied between $10\,\mu L\,h^{-1}$ and $50\,\mu L\,h^{-1}$ and the electrode voltage between 1 V and 5 V. Using a camera, images of the flowing cells were taken in an ROI behind the last focusing electrode (E2). These images were then used to manually count the proportion of passing cells that were above the electrode, i.e., that were deflected. Figure 30 on page 54 shows exemplary images of correctly deflected cells as well as cells broken through the fields and the location of the ROI. In this way, a "deflection efficiency" could be determined for each combination of voltage and flow rate tested. This experiment was carried out on several days for each combination of flow rate and voltage a total of three to five times. The results of all test days were averaged and are shown in Figure 31 on page 54. The overview shows an increased deflection with higher electrode voltage and a decreased deflection with higher flow rate. While the increase along the voltage tends to be sigmoidal, the decrease along the flow rate appears exponential.

In order to determine the electrode voltage required for complete deflection of the cells at each flow rate, the deflection efficiencies determined were plotted separately for each flow rate and fitted with the error function (see chapter 4.14). The fits are shown in Figure 32 on page 55 and the corresponding parameters of the error function are listed in Table 2 on page 56. Using the determined error functions, the electrode voltage required for sufficiently reliable deflection of the cells could then be determined. A 99% deflection was assumed to be sufficient. The minimum voltages determined in this way are also listed in Table 2.
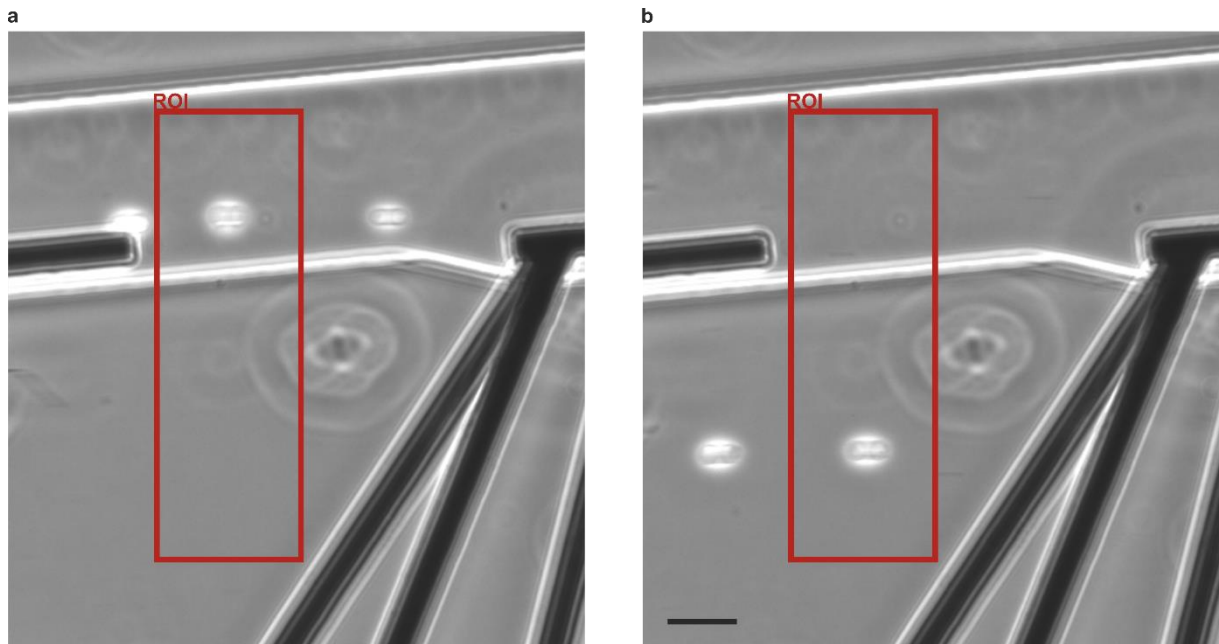
Figure 30: Comparison of correctly and incorrectly deflected cells. a, The cells (white objects) flow through the image from left to right, being deflected to the top by the electrode E2 (black line, see Figure 19). **b**, Cells flowing through the system are not deflected sufficiently, thus breaching the field barrier and appearing below the electrode structure. Based on their respective position within the ROI (red rectangle), each cell can be assigned to one of the two groups. The scale bar corresponds to 50 µm. Results in collaboration with My Vu.
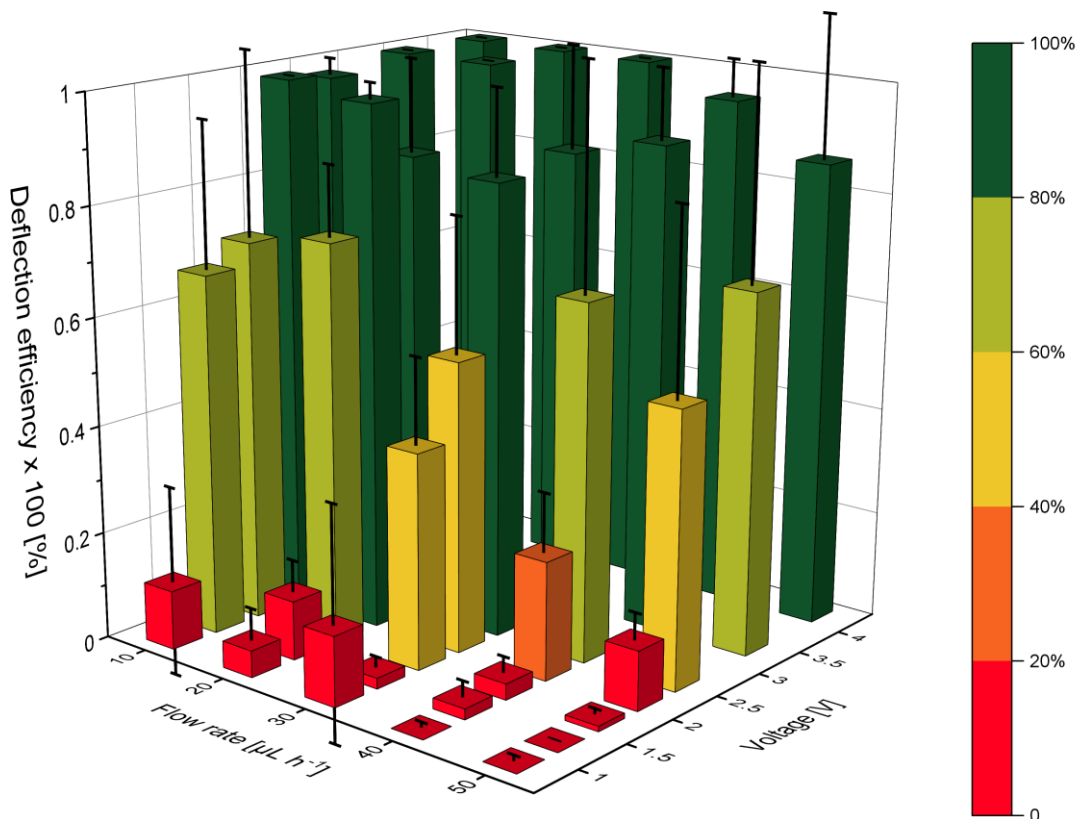

Figure 31: Cell deflection efficiency as a function of flow rate and electrode voltage. The column height corresponds to the mean value of several measurement results for the respective parameter combinations, the error bars show the standard deviation. Results in collaboration with My Vu.
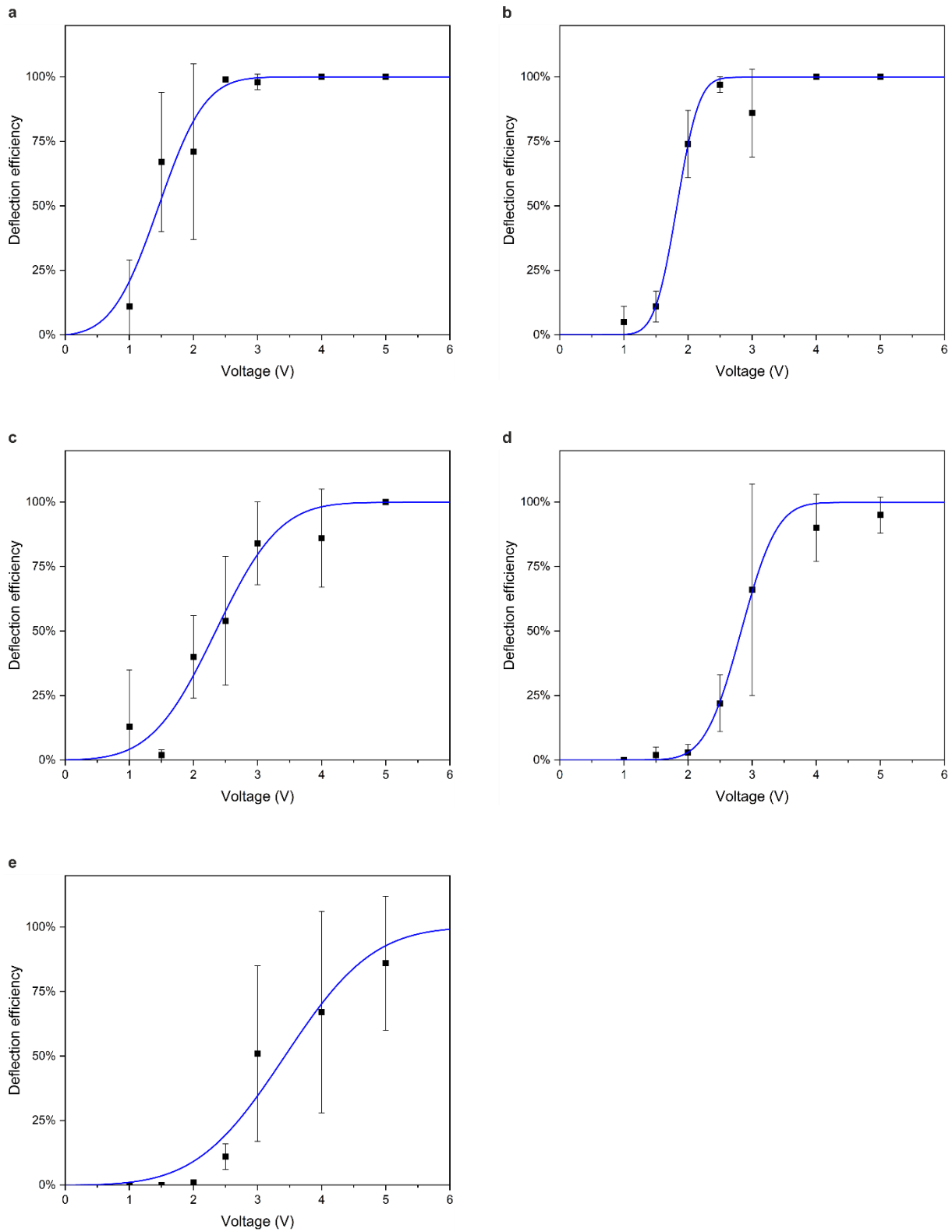
Figure 32: Cell deflection efficiency as a function of electrode voltage. The data points listed show the averaged deflection efficiency and its respective standard deviation for different flow rates: **a**, 10 µL h^{-1}, **b**, 20 µL h^{-1}, **c**, 30 µL h^{-1}, **d**, 40 µL h^{-1}, **e**, 50 µL h^{-1}. For each flow rate, a fit curve of the data was created using the error function, shown in blue. Results in collaboration with My Vu.

Table 2: Parameters of the error function used to fit the data for the tested flow rates. $v_{99\%}$ indicates the voltage required for 99% deflection efficiency calculated from the fit. Results in collaboration with My Vu.

Flowrate [µL h^{-1}]	A	k	x_0	y_0	$v_{99\%}$ [V]
10	0.5026	1.48843	1.21569	0.49702	2.79
20	0.499	3.10157	1.5248	0.49945	2.48
30	0.50019	1.07074	1.96112	0.49889	4.20
40	0.49924	1.90444	2.36609	0.49938	3.88
50	0.50079	0.78615	2.86064	0.49911	5.94

5.4.4   Cell velocity distribution as a function of the flow rate

The natural size distribution of a cell population leads to different flow rates of the individual cells due to the parabolic flow profile in microchannels (see chapter 3.2). To characterise this velocity distribution, red stained cells were pumped through the chip at different flow rates. Inside the ROI, the velocity of the cells was determined and saved as in a sort. The same python script as in section 5.2.1 was utilised for this. However, no sorting of the cells took place, but electrodes E2 and E3 were active to bring the cells into a pearl chain configuration and guide them towards the ROI. Figure 33 shows the cell velocities determined at different flow rates. A linear increase in the mean cell velocity with an increase in the flow rate is clearly visible. At the same time, the standard deviation of the cell velocity also increases. However, the coefficient of variation decreases and remains constant from a flow rate of approximately 40 µL h^{-1}.

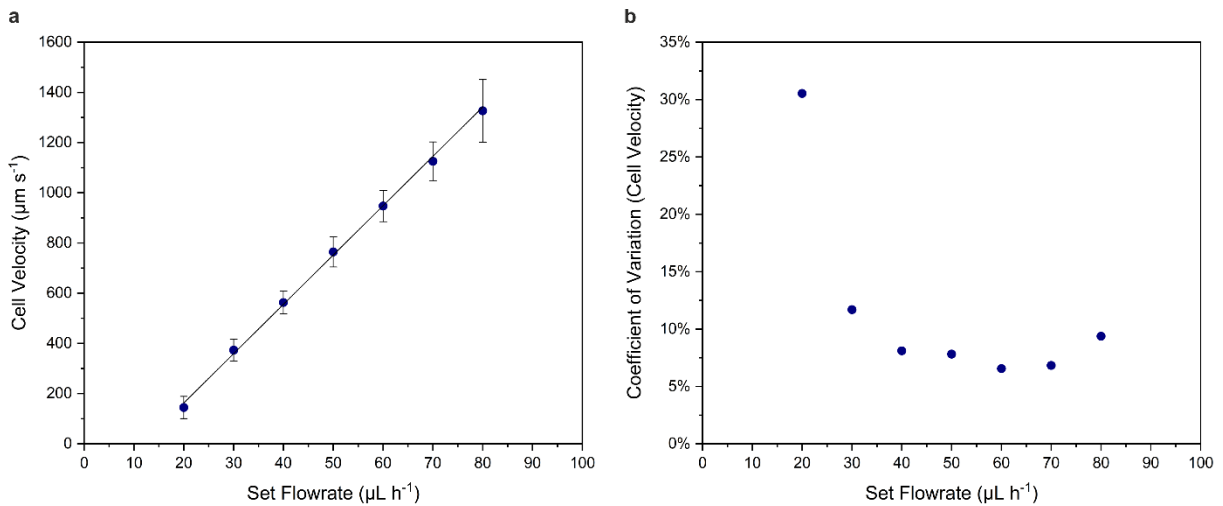**Figure 33: Velocity distributions of cells in the microchannel with active electrodes. a**, Determined cell velocity as a function of the applied flow rate. The blue points are experimental results, the error bars indicate the standard deviation. The black line shows a linear fit with R^2= 0.9962. **b**, Change of the coefficient of variation of the cell velocity with increasing flow rate.

5.4.5 Influence of DEP forces on the focal plane of the cells

As described in section 3.3.2, the forces acting on the cells flowing along the electrodes not only have a force component that drives the cells away from the electrodes, but also a component that drives the cells towards the centre of the channel. To demonstrate the benefit of this effect for the image acquisition, cells were pumped through the system at a flow rate of 40 µL h^{-1}. A voltage of 3.5 V was applied to electrodes E1 and E2. Transmitted light images were taken of all cells in the ROI area at 60x magnification. The focal plane of the microscope optics was adjusted in such a way that, according to the experimenter's assessment, most of the cells were sharply imaged.

In the next step of the experiment, the electrodes were switched off so that no more interaction of the cells with electric fields could take place. Again, images of the flowing cells were taken, while the set focal plane remained unchanged. Exemplary images of cells at both experimental conditions are shown in Figure 35 on page 58. It is clearly visible that in the case of the active electrodes, most cells had a common focal plane. In the case of the inactive electrodes, however, the focal plane varied significantly between the different cells.

5.4.6 Influence of DEP forces on the velocity distribution of the cells

The previously shown results indicate that the interaction with the electric fields changes the vertical position of the cells in the channel. Due to the flow profile prevailing in microchannels (see chapter 3.2), this also suggests a change in their respective velocity. To verify this, the previously conducted experiment was repeated with red stained cells. The colouring of the cells allowed tracking of the individual cells as they flowed through the ROI. Based on the position data obtained in this way, the velocity of each individual cell could be determined using the frame repetition rate. The determined cell velocities for both experimental conditions are shown in Figure 34. A shift of the average velocity of the cells towards higher values is clearly visible. The results also show a narrowing of the distribution in the case of the active electrodes.
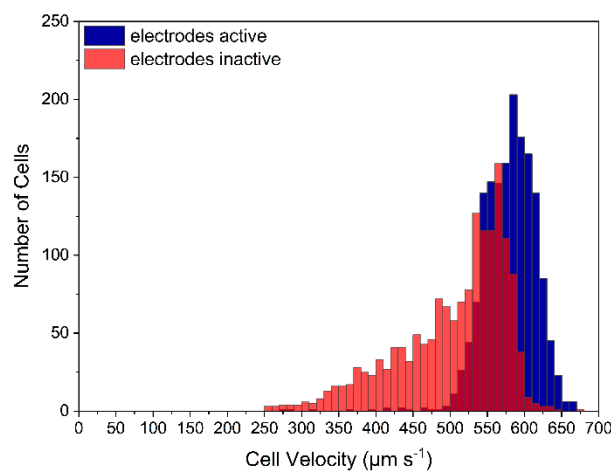

Figure 34: Cell velocity distribution depending on electrode activity. Cell velocity data from cells flushed through the microchannel in the absence of the electric field are shown in red. Data from dielectrophoretically guided cells flushed through the system with active electrodes and the same flow conditions is coloured blue.

Based on the recorded cells in Figure 35, it can also be seen that cells in a similar focal plane also flowed through the channel at a similar velocity. The white numbers in the image indicate the average measured velocity of the respective cell.
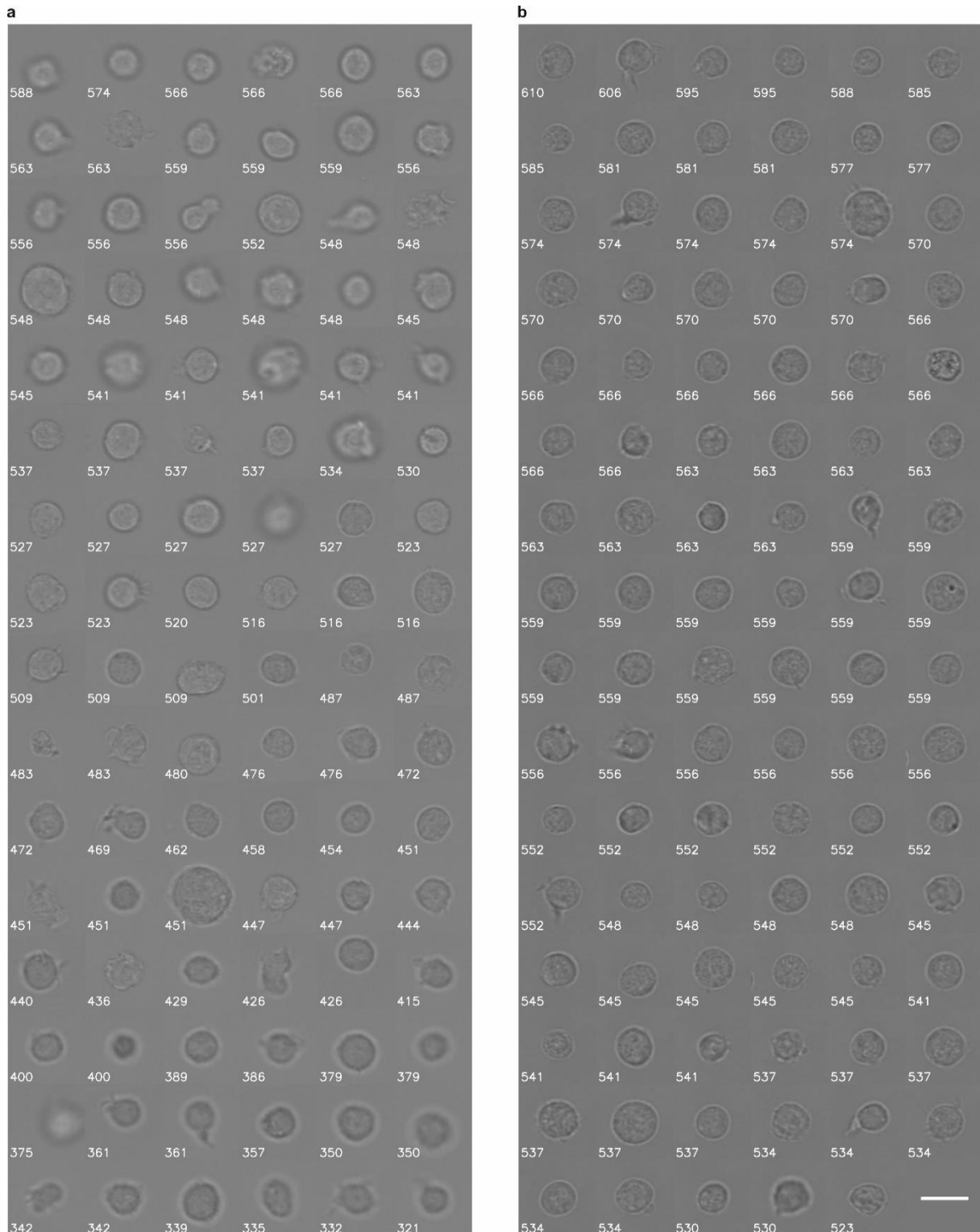
Figure 35: Influence of dielectric field forces on the focal alignment of cells. a, Representative selection of images of cells passed through the channel with inactive electrodes. The images are arranged by the respective determined cell velocity, which is given in white and in $\mu m\ s^{-1}$ for each cell. **b**, Representative selection of cells and their corresponding velocities in $\mu m\ s^{-1}$ that were flushed through the channel with active electrodes under otherwise identical conditions. The scale bar represents 20 μm. Results in collaboration with Neus Godino.

5.5   Fluidic Interface

5.5.1   Bubble Traps

A critical prerequisite for the functioning of the entire microfluidic system is the absence of air in the system, as its compressibility could cause it to interact with the pressure-based pumps and thus influence the volume flows. Air bubbles in the central channel could even directly influence the flow direction of the cells, as they represent an impenetrable obstacle for the cells.

In order to remove any air bubbles that may be present from the system and to rule out these effects, bubble traps tailored to the system were developed in addition to the measures listed in chapter 4.8 (degassing the liquids, thorough rinsing during experiment preparation). In these components, the liquid is guided along a membrane made of polytetrafluoroethylene (PTFE), through which any air bubbles are sucked out by the use of a vacuum.

Bubble traps are commercially available and widely used in microfluidics. Although the specific design of the fluid channel varies from manufacturer to manufacturer, the traps usually feature a meandering channel with a large diameter (up to a few millimetres) to increase the residence time of the fluid on the membrane and maximise the removal of air bubbles. However, for the system developed in this work and the cell suspensions flowing in it, these commercially available components are not suitable, as sedimentation is to be expected to a high degree due to the low flow velocity and thus a large part of the cell sample would be lost in the bubble traps. For this reason, bubble traps with a much smaller channel diameter and an overall shorter channel were developed and made of PMMA. The dimensions were chosen so that the commercially available polymer membranes could also be used for the self-developed traps. Figure 36 shows the two halves of the self-made bubble trap. Due to the short channel length required, it was possible to pass two parallel streams through the same bubble trap, saving space and material. In the system, each fluid stream was passed through a bubble trap before entering the microfluidic chip.

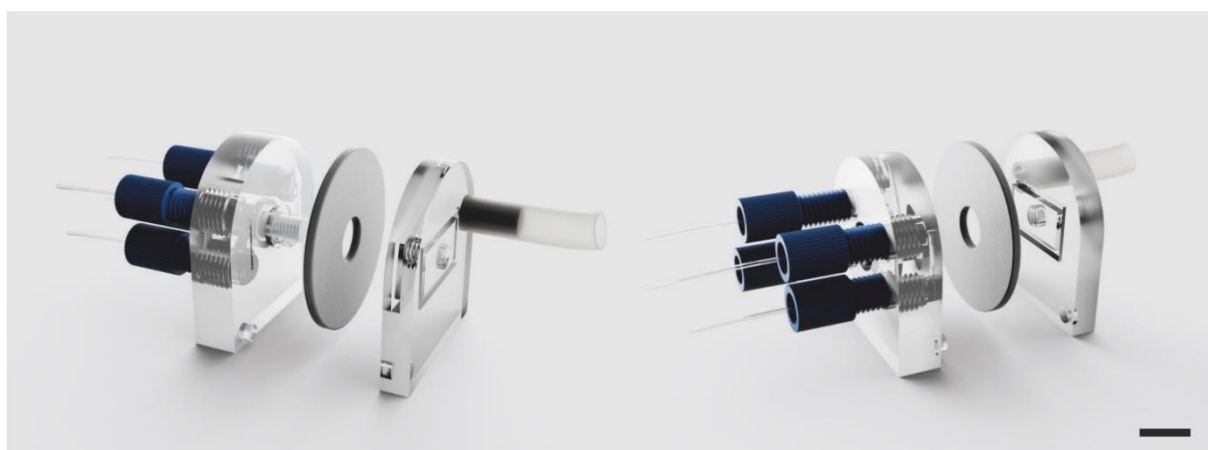**Figure 36: Rendering of the self-made bubble trap.** The device is made of two PMMA halves with a PTFE membrane in between. One half contains fluidic connections and a microchannel to guide the cell suspension along the membrane. The other half has a larger channel and a tubing connector allowing negative pressure to be applied to the other side of the membrane. The scale bar corresponds to 1 cm. In collaboration with Erik Hahn.

In experiments with built-in and active bubble traps, a significantly faster bubble-free filling of the system could be observed. No air bubbles appeared in the system over the course of the experiments.

5.5.2 Sample reservoir

Typically, standard reaction vessels are used for the operation of the pressure-based pumps. A microfluidic tube is immersed in these and the fluid is then pumped into the tube against gravity by using overpressure, as described in chapter 4.3. In the case of using cell suspensions, however, this means that the flow must be fast enough to drag the cells along. Although measures were taken by means of additives (see section 4.9.3) to equalise the density of the cell suspension and the surrounding medium, this could not be ensured due to the low applied flow rates. Consequently, it was assumed that cells remained at the bottom of the reaction vessel due to cell sedimentation. To circumvent this problem, a sample reservoir was made of PMMA, in which the microfluidic tube reached the liquid from below. This was to ensure that sedimenting cells fell into the tube and thus entered the system safely. The manufactured sample reservoir is shown in Figure 37.

The outer diameter corresponds to that of commercially available 1.5 mL reaction vessels, the inner diameter is slightly smaller due to the wall thickness required for PMMA. The walls of the reservoir are straight, only the bottom of the vessel converges at an angle towards the centre, where a 500 µm diameter hole is located through which the cell suspension is fed into the tube. The tube can be connected to the reservoir from below using a standard UNF thread (1/4″-28). In experiments conducted using this reservoir, a constant flow of cells into the system over several hours was observed.
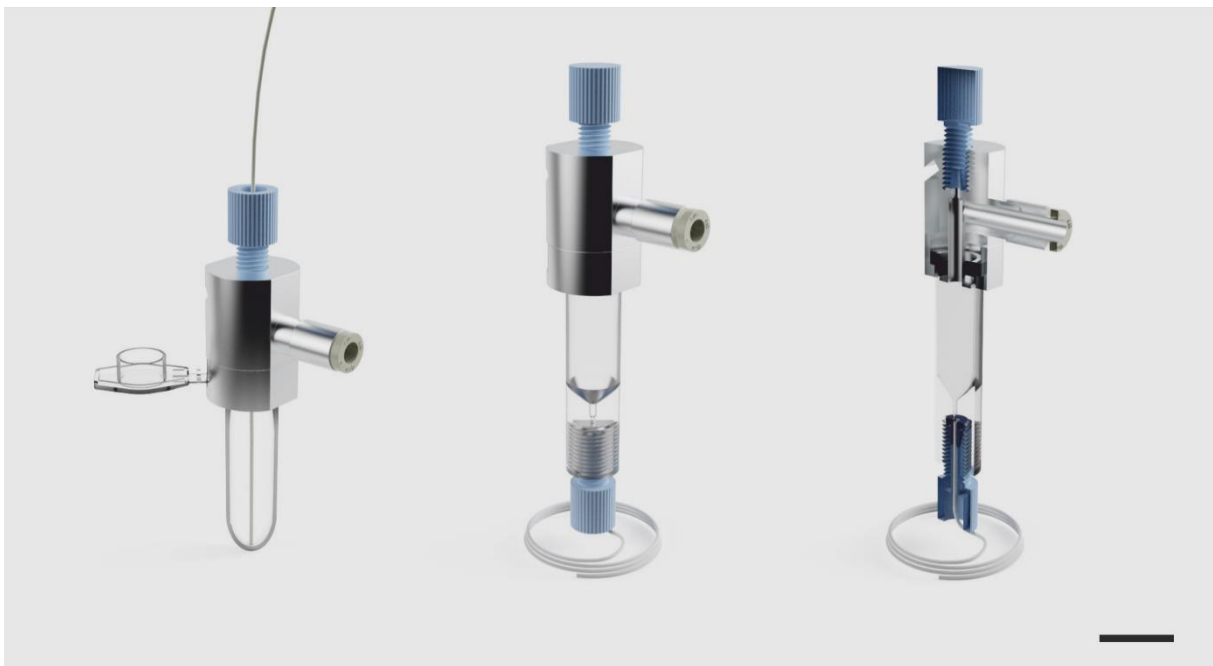

Figure 37: Rendering of the self-made sample reservoir. Contrary to the conventional configuration with standard reaction vessels (left), in the case of the self-developed sample reservoir (centre & right) the fluid is dispensed from the bottom of the reservoir instead of the top. The scale bar represents 1 cm. In collaboration with Erik Hahn.

6 Discussion

The identification and sorting of cells with specific physiological properties from inhomogeneous cell populations is a key requirement in biotechnology, biomedicine and research. Since these properties are closely linked to the morphology of the cells, but are inaccessible to conventional methods like FACS, a high demand for image-based cell sorting methods exists. For broad applicability, high demands are placed on the sorting performance of the system, including achievable purity, recovery rate and throughput. To date, however, there is a lack of simple and cost-effective solutions, which significantly limits the accessibility and availability of image-based cell sorting for laboratories.

In this work, the potential of a low-cost and low-complexity DEP -based microfluidic system for high-quality image-based cell sorting in continuous flow at low process velocities was demonstrated. The developed system is characterised by its compatibility with standard microscopic, microfluidic and computational equipment and the resulting image quality and flexibility regarding the analysis method. In addition, it is characterised by the low flow velocity of the cells and the precise cell handling using DEP. These characteristics set it apart from complex high-throughput systems.

The properties and limitations resulting from the specifications of the system are discussed and evaluated in the following based on the results of this work.

6.1 Dielectrophoretic cell handling

The entire handling of the sample flowing through the channel in the system is controlled by the well established DEP technique[52,53,149]. This includes cell alignment in a pearl chain configuration to analyse the cells consecutively, velocity focusing and elevation to the optical focal plane, and finally stepwise sorting. The DEP forces are exerted by electrodes on the channel surfaces, allowing great freedom and precision with regard to individual cell handling elements. All electrodes are operated by a single generator, which is controlled via USB using a standard PC. This makes the system simple, robust and reliable compared to other systems that rely on sheath flows, sometimes combined with other technologies, for these purposes.

In addition, the use of DEP technology enables short switching times of a few milliseconds. Other systems that use, for example, hydrodynamic flows to influence cell movement, such as syringe-assisted pumping or electrokinetic mobilisation, usually suffer from slower reaction times[140,150,151].

Alongside these advantages, however, DEP technology has one major limitation: the use of DEP requires low flow velocities of the cells, as the DEP forces are relatively weak and the precise handling of cells within the microchannel is based entirely on the equilibrium between hydrodynamic and DEP forces. However, the DEP forces cannot be increased infinitely, as this would result in enhanced electrode degradation and stronger joule heating. In addition, the output of the generators is limited to a maximum of 10 V.

6.1.1 Sorting Mechanism

For efficient cell sorting, it is crucial that the individual cells are sufficiently separated from each other. The distance needs to be larger than the sorting window of the sorting mechanism and is statistically distributed (see appendix). For efficient sorting and high throughput, the smallest possible sorting window is beneficial.

The use of stepwise-arranged microelectrodes for the handling of single cells with relatively small individual electrodes (50 µm) in relation to the cell size enables highly precise handling of the cells. This results in an extremely small sorting window, allowing operation with high particle densities. For the future, it is also conceivable that the electrodes can be shortened from 50 µm to the actual size of the cells of about 10 µm. This contraction could reduce the sorting window by a factor of 5. However, this also places high demands on the precision of the sorting algorithm, the determination of the cell velocity and the electrode activation to ensure a reliable sorting process.

Other systems using a variety of sorting techniques such as optical tweezers, acoustic sorters or (piezo-triggered) flow-based mechanisms feature similar sorting windows of one to several cell diameters[43,44,140,142]. Established droplet-based sorters and similar systems have significantly larger sorting windows of several to hundreds of cell diameters[25,26,50].

However, a high precision does not necessarily result in a high achievable throughput. With optical tweezers, for example, the force that can be achieved for particle manipulation is limited. The technology consequently only functions at low flow velocities, limiting the throughput. This restriction also applies to the DEP technology used in this work as mentioned above.

6.2 Sorting Performance

The sorting performance of different systems can essentially be compared based on the parameters throughput, target cell purity and cell recovery rate. Maximising one parameter is usually at the expense of another, as can easily be seen from the decrease in purity with increased throughput (see appendix).

Depending on the requirements of the particular experiment, the importance of the parameters mentioned may vary. For example, in a (coarse) enrichment of target cells in a large sample volume, high throughput may be more important than optimising purity down to the last percent. A comparison with various other systems is given below, taking these parameters into account

6.2.1 Throughput

Established cell sorting systems achieve a throughput of several thousand cells per second[25,26]. This makes them suitable for processing cell samples with high cell numbers and volumes (typically hundreds of thousands to several million individual cells in a few millilitres of sample), as they are common in cell culture laboratories and research. Image-based systems inspired by these methods achieve similar throughputs, albeit at the expense of other aspects such as image quality[44,50].

In comparison, the throughput of approximately 1-3 cells per second in the system presented in this work is very low despite the precise cell handling. Although other systems that rely on similarly precise handling of cells with low forces operate at the same order of magnitude (1-5 cells per second)[142], an increase in throughput is required for a broad application in the future.

Besides the already mentioned reduction of the sorting window, this could be achieved by two additional improvements.

Firstly, the image acquisition itself could be improved. With stronger illumination (e.g., lasers) and higher detector sensitivity (e.g., monochrome camera, binning etc.) it is certainly possible to reduce exposure times by a factor of 3 to 5 and work with correspondingly higher flow velocities (and higher flow rates) without major loss in image quality. In order to enable a higher flow rate, a redesign of the microchannel and the electrode layout would be inevitable, as smaller electrode angles would be required.

Also within the scope of possibility, although more difficult to implement, would be a parallelisation of the system, i.e.,, the operation of several channels in parallel. However, this would involve more complicated changes regarding image acquisition.

Overall, an increase in throughput by an order of magnitude seems feasible.

6.2.2 Purity

In addition to the throughput already mentioned, the achievable purity of the target cells is also decisive for the applicability of a sorting system. To investigate this, a sorting process using cytosol-stained cells and a colour-based evaluation was established and then transferred to a morphology-based sorting.

Target cell populations of up to 95 % purity could be achieved, depending on the sorting mode and algorithm used. With these values, the system introduced is on a par with other systems such as the iIACS and the ICS[43,45,50,140,142].

The sorting performance remained constant regardless of the configuration of the system (i.e.,, no difference was found between velocity-based or position-based sorting at 4x or 60x magnification, respectively). This implies that the physical sorting process itself always worked reliably, which underlines the robustness of the system. The small deviations in the purities achieved can be attributed to the functionality of the algorithm (for example, the specificities of the different analysis scripts differed by up to 4%). However, practically no differences were found in the results of yield and purity sorting, indicating that no compromises need to be made on these parameters, regardless of the method chosen. This can again be explained by the length of the sorting window, as the cells can basically always be separated properly.

In all cases, the sorting performance of the system decreased towards higher throughputs, i.e.,, lower cell distances, which corresponds to the theoretical expectation derived according to Poisson statistics. The observed minor deviations between the expected and achieved purities can essentially be attributed to the fact that some simplifications were made in the theoretical approach. For example, physical duplicates (i.e., cells sticking together) were not taken into account.

6.2.3 Recovery rate

Overall, not only the purities but also the cell numbers determined using the live cell imaging system correspond to the data obtained from the videos taken during the sorting process. On average, 85% of the sorted cells could be recollected from the system. With this recovery rate, the system ranks just above other systems such as iIACS and in the range of typical FACS sortings[26,45]. The observed loss of approximately 15% of sorted cells can be caused by several factors.

One possibility is the adhesion of the cells to the outlet tubing[26,152]. This happens primarily when cells are transferred from channels or tubes with a large diameter into channels or tubes with a (significantly) smaller diameter. In the developed system, the cross-sectional area of the outlet channel on the chip and that of the outlet tubing are similar, but the aspect ratio changes significantly (from a 300 µm * 35 µm channel into a tubing with 50 mm radius).

Possible solutions to avoid adhesion include coating the tubing with protein[26], using a tubing with a larger diameter or applying a sheath flow[152]. Protein coating was not performed and larger diameter tubing was not an option as flushing out the cells would have taken a disproportionate amount of time. While a sheath flow was used, it was only applied in one plane (i.e.,, 2-dimensional). Consequently, it cannot be assured that this prevented adhesion. A combination of larger tubing diameter and faster sheath flow could be a solution, as this would allow greater distances to the tubing wall to be achieved with a similar rinsing time. However, this would result in higher shear forces, which are unfavourable.

Furthermore, this approach is not useful in the area of the open end of the tube from which the sample drips into the target cell reservoir. Here, a periodic droplet formation and detachment takes place, resulting in a liquid movement on the cross-sectional area of the tubing. Therefore, cell contact with the tubing cannot be ruled out and as a result, cell adhesion to the tubing cannot be excluded.

Another possible explanation for the measured cell loss apart from adhesion effects is that not all cells in the well plate were detected, as a threshold value had to be set for the automatic detection. Although the results of the automated image analysis were randomly verified, minor deviations with regard to the total number and the calculated recovery rate cannot be ruled out. An alternative manual counting could provide better and more accurate results, but is not feasible as it is too time-consuming. Furthermore, automated cell counting is a common approach also performed by other groups[45].

6.3 Image acquisition & image quality

Image-based sorting requires a sufficiently good image quality of the cells to be sorted. This is dependent on the magnification, resolution and exposure time.

However, due to the high flow rates mentioned above and the high cell throughput in other systems, these are limited in terms of image acquisition, so that not all of these requirements can be optimally fulfilled. For example, the high flow velocity of the cells in the iIACS system means that the cells would only be visible on the camera sensor for less than a millisecond, meaning that the exposure time could be approximately 1 ms at maximum. However, with this exposure time, extreme motion blurring would occur, making the captured images practically unusable for evaluation. Only with an exposure time in the nanosecond range a sharp image

could be expected, but the brightness would in turn be very low. In order to still achieve sufficiently long exposure times, Isozaki *et al.* use a rotating polygon mirror to "freeze" the cell on the camera sensor and avoid motion blur[45]. In this example, sufficient image quality is consequently only possible with great effort. Despite this effort, the image can still only be captured with a 20x lens with low NA, reducing both magnification and resolution.

In the case of the ICS by Schraivogel *et al.* no camera is used at all, but the image is calculated from the signals of a laser dot array. Since in this case the resolution depends on the distribution of the laser spots (104 laser spots across 60 µm), this also results in reduced resolution and thus reduced image quality[50].

With the system developed, it was possible to obtain images of unprecedented quality in image-based cell sorting by using high-resolution lenses with high magnification and high NA (up to 60x magnification and 1.4 NA). Due to the low flow velocity of the cells, exposure times in the millisecond range could be realised without motion blur. The automatic vertical arrangement of the cells in a common focal plane by the DEP forces contributed to the high quality of the images despite the shallow depth of field at high magnifications. Other systems use complex sheathflow architectures and other elements such as acoustic focusers to achieve this focusing, making them more complicated in direct comparison to the system presented here[44,45,50,140].

The combination of outstanding image quality and simple technology sets the system clearly apart from all other systems known to date. This is achieved by using established standard microscopy equipment, which also provides a high degree of flexibility regarding the imaging technique. Besides frequently used methods such as transmitted light, phase contrast or (multicolour) fluorescence imaging of a wide range of excitation and emission wavelengths, the use of less common imaging techniques such as polarisation, dark field or Raman microscopy is also possible as Nitta *et al.* have already shown[48]. Although various adjustments would have to be made to the microscopy setup, such as replacing optical components, light sources and detectors, no changes would be required to the microfluidic system itself.

Furthermore, the large field of view together with the low flow rate could be utilised as it allows repeated images of the same cell even at moderate frame rates[51]. To benefit from this, a light sheet illumination of the microchannel is another conceivable imaging technique, which could enable confocal imaging of the cells[153,154]. Depending on the properties of the light sheet, this could even be used for z-stacking or, in combination with induced rotation of the cells, also for 3D imaging of the cells, thus making accessible completely new sorting criteria.

In this work, the flexibility of the set-up was impressively demonstrated by combining the microfluidic system with quantitative phase microscopy[148]. In contrast to the analysis method presented in this paper, the technique works label-free and accordingly features a dedicated analysis script. The data analysis is relatively complex and more computationally intensive than both the colour-based and morphology-based analysis used in this work. The longer computing time of approximately 100 ms required for the evaluation at a relatively low frame rate of approximately 10 ms was provided by a low flow rate of the cells. While the microfludic system itself was set up on site within a few hours and did not require any changes, the generator control had to be integrated into the analysis script of the phase microscopy setup. This was possible quickly and easily since the signal generator can be controlled via USB and the corresponding communication protocols can be easily integrated into existing analysis programmes.

The successful combination of both systems shows how flexible the imaging technique can be adapted to the user's requirements and demonstrates the versatility of the microfluidic DEP sorting approach.

6.4 Image analysis

Depending on the microscopy method used, the underlying data and the desired depth of analysis, image analysis algorithms of varying complexity are required to interpret the image data and derive a sorting decision. Complex analyses usually require more extensive data management and handling[43]. If the sorting decision also has to be achieved in a short time, the capabilities of a standard PC can quickly be exceeded. Especially in systems operating at a high flow rates, only a short time window remains for the evaluation of the collected image data, as the cells quickly complete the distance between the analysis and the sorting area. While image acquisition takes relatively little time, image analysis is often a limiting factor in cell sorting.

Examples are the iIACS system and the optical force sorting system developed by Lee *et al.*, which each require about 30 ms for evaluation, or the cytometry-like deformability-activated sorting device by Choi *et al.*, which requires 100 ms[45,47,142].

Accordingly, the computing power must either be enormously high, as in the 9-PC network of the iIACS system, or only a limited depth of analysis is possible, as in the ICS system, which does not use optical imaging but calculates the images from an electrical signal in order to arrive at a sorting decision quickly enough. A third option is to maximise the time between image capture and sorting (e.g. 3.2 cm between the image acquisition and sorting in the iIACS system).

However, a longer channel also imposes high demands on cell handling, as the cells are required to maintain a constant velocity over the entire distance, i.e., they need to remain in the same flow regime. A long channel is therefore not without disadvantages and can also increase the complexity of the system. The iIACS system, for example, uses an acoustic focuser to guide the cells over the long distance.

In the present system, the long analysis time is not the result of the channel length, but of the low flow velocity (i.e., a few hundred µm per second). This means that even with a short distance between the analysis and sorting region, the cells need a relatively long time span of several hundred milliseconds for this distance, which is available for image analysis. This enables the use of complex analytical algorithms such as advanced deep learning algorithms even with average standard computing equipment.

To a certain extent, the distance in the developed system can also still be adjusted by changing the position of the image acquisition area relative to the sorting electrodes. Since the cells guided by the microelectrodes are kept in a constant focal plane and maintain a constant velocity, no further need for additional control of velocity and trajectory is required and the shift of the ROI is easily possible.

Furthermore, the relatively long frame acquisition and processing times allow the use of a conventional CMOS colour camera and the inclusion of debayering and on-line dynamic range colour adjustment processes for each frame. The resulting data set is of high quality and contains more information than data generated with monochrome cameras or no camera at all[47,50,142].

However, this comparison raises the question of the added value of such a high quality data set, as image-based cell sorting obviously works in the other systems with lower quality data to derive the sorting decision. For example, Isozaki *et al.* claim that the image quality they have achieved is sufficient to sort cells based on fluorescence in situ hybridisation (FISH)[45,155,156]. The effort and the long analysis time are therefore only worthwhile if additional information can be derived from the data. It remains to be seen whether questions arise that can only be answered with the help of the image quality of the system developed in this work.

6.5 Cell vitality

For further use of the cells, which usually follows sorting, it is essential that the cells are vital and have not been damaged during the sorting process. Existing systems for cell sorting often focus on high throughputs. In FACS instruments, for example, the cells are hydrodynamically focused with sheath flows and as a result high flow velocities of up to 1 m s^{-1} prevail within the microchannels as described above. This imposes high shear forces on the cells, which are potentially cell-damaging[78].

Accordingly, it can be assumed that this effect also occurs in other systems that operate at high flow rates, such as iIACS and ICS[45,50]. However, viability measurements have not yet been performed on cells processed with these systems.

At lower flow rates of approximately 10 cm s^{-1}, though, the cells survive the sorting process essentially unharmed, as demonstrated for the Surface acoustic wave actuated cell sorting (SAWACS) (i.e.,, 93% vital processed cells vs. 97% in a reference sample)[140]. Yet, also in this case, only a relatively simple (i. e. inconclusive) distinction between living and dead cells was made using calcein staining.

The flow velocities prevailing in the system developed in this work lie between one (sheath flow) and three (central sorting channel) orders of magnitude below the aforementioned values. Transferring the results here as well, cell damage due to shear forces seems rather unlikely. Moreover, in the presented system, the cells are kept continuously in (conditioned) cell culture medium and are also flushed out in this medium, which contributes to the preservation of cell viability.

However, the DEP system operates with electric fields that can damage the cell membrane and cause Joule heating (see section 3.4.2). The cells are exposed to electric fields with electrode voltages of up to 5 V for a relatively long time of several seconds, but are always deflected towards the field minimum where the field strength is significantly lower. The heat introduced into the system by the fields via joule heating has not been investigated but must be taken as present based on previous studies[83]. Since heating was assumed to be in the single-digit degree range[83] and the ambient temperature of the system was at room temperature (i.e., approx. 22 °C), it is not expected that critical temperatures above 37 °C were reached.

Nevertheless, especially due to the difficulty in quantifying the interactions of the cells with the electric field, an investigation of the cell vitality also appeared to be reasonable for the present system. Since cell vitality is not a binary parameter, a cell proliferation assay was performed in combination with cell counting instead of live-dead staining to determine gradual differences in vitality. This was relatively complex and time-consuming, but allowed a more detailed statement about the condition of the cells after sorting.

The high viability rates of the processed cells compared to standard cell cultures demonstrate the biocompatibility of the presented approach at this stage and indicate the gentleness of the electric field exposure in the setup. Consequently, it can be assumed that neither the electric fields themselves nor the occurring joule heating have a negative influence on the cells. However, these results remain valid only as long as no changes are made to the system. With regard to the flow velocity, a certain tolerance certainly exists, since no cell damage could be observed even in faster flowing systems[140]. This does not apply to the influence of the field strengths and the associated joule heating, so repeated investigations would be necessary whenever the voltages or frequencies are changed.

In addition, it should be noted that the overall cell numbers studied were low, leading to potential inaccuracies in cell number determination. By normalising the measured absorbance to the cell number, this error could have been transferred to the determined metabolic activity per cell. The results must consequently be considered with caution and, if necessary, the experiments should be repeated with higher cell numbers and an optimised protocol. An additional living-dead staining of the processed cells would ensure better comparability with other set-ups.

Taken together, the results of the conducted experiments indicate the gentleness and biocompatibility of the set-up, making it particularly interesting for processing vulnerable (i.e., shear-sensitive) and valuable cells.

6.6   System stability

High-throughput systems need only a short time to sort a cell sample. For example, a FACS can sort several milliliters of sample per minute[26]. In contrast, at slower flow rates, such as in the present system, a sorting operation can take several hours, since only a small amount of sample can be processed per time unit (several tens of microliters per hour). Therefore, for a reliable sorting of cells, not only a reliable function of the sorting mechanism, but also a stable operation of the system over a long period of time, i.e., the entire sorting process of a sample, is of utmost importance.

To ensure this stability for the developed system, custom made bubble traps were developed. These not only enabled efficient bubble-free filling of the system, but also prevented the formation of new air bubbles during the sorting process. The traps did not require any maintenance other than occasional replacement of the membranes, and thus did not increase the complexity of the system. The sample reservoir, which was also custom-made, allowed samples to be easily introduced and exchanged in the system. Furthermore, the reservoir ensured a constant and reliable flow of cells into the system.

Together with the employed pressure-based pumps, the devices allowed stable operation of the system over several hours and ensured high reliability of the DEP-based sorting system.

6.7 System operation & development

Existing systems for (image-based) cell sorting range in usability from established end-user devices (FACS, ICS) to extremely complex systems that require several trained scientists to operate (iIACS)[44]. In the latter case, the system consists of complex sheathflow architectures for cell focusing, multiple high-performance computers for image processing, an acoustic focuser for position control of the cells downstream, and a sensitive sorting mechanism. Hence, there are several different systems in one setup, which all need to be monitored. The high complexity of these systems is usually accompanied by a high price.

In contrast, other systems are less complex and easier to operate, like the piezoelectric actuator based user-freidnly technique of Lee *et al.*[43]. However, these simple systems often only provide fluidics and rely on established techniques for the imaging process. In addition, peripheral equipment such as pumps and computational equipment are required. In addition to their compatibility with standard microscopy equipment and the resulting flxibility with regard to imaging techniques, these simple systems offer further advantages such as the capability to handle small sample volumes of a few µL[43].

The system presented in this work is also characterised by its simplicity and user-friendliness. It is compatible with standard microscpy equipment and all components are controlled by standard computing equipment. In addition to the handling of small sample volumes (less than 100 µL), it features several other properties that are beneficial for the handling of cell samples. For example, the cells are in a (conditioned) cell culture medium during the entire sorting process, which is convenient for the further cultivation of the cells after sorting.

In addition, the system allows a detector calibration and gating strategy development outside of the fluidic system, without flushing cells through the system as required by ICS or FACS. This is possible since the images taken of cells in the microchannel are largely identical to images taken in standard culture devices (e.g. well plates or Petri dishes) with the same camera parameters. Exemplary images of cells recorded in the channel and in a 96-well plate are shown in Figure 38 on page 70. This procedure prevents cell stress and cell loss in the fluidic system, an advantage worth mentioning, especially for samples with a low cell number.

As a result, the system is particularly interesting for applications with small or sensitive samples with low cell volumes that are not suitable for standard flow cytometers and related systems.

While the operation of the system is simple, the installation of the system requires experience and training. The interface shown in section 4.1.1 consists of many individual parts that need to be correctly assembled and aligned. A part of the interface is also placed directly on the chip, increasing the risk of shattering. This topic thus offers room for improvement, for example by developing or adapting a more fail proof interface such as presented by Kortmann *et al.*[157,158].

The development of microfluidic chips also requires expertise. Although the design of new channel and electrode structures can be implemented in a few days to a few weeks, the production of the microchips by a specialised company takes about 3-6 months. Therefore, while it is possible to respond precisely to different user requirements, the timeframe required to do so is far greater than for other processes such as Polydimethylsiloxane (PDMS) molding, which is often used in microfluidics[159]. The rapid prototyping process developed in the context of this work can only compensate for this disadvantage to a limited extent.

The main reason for the lengthy production process is the complexity of the microchips. They contain several layers of electrode structures that have to be applied to glass substrates in laborious etching processes before they can be bonded using a spacer to form a microchannel. In addition, the electrical and fluidic contacting has to be applied manually.

Due to the complex manufacturing process, such a microchip is also expensive (i.e., several hundred euros) and thus has to be used several times in order to amortise depending on the application. This is associated with a number of problems, as, for example, cell debris can cause clogging after prolonged operation. Disposable chips, as often used in microfluidics, would therefore be advantageous, even if they have drawbacks in terms of sustainability[160].
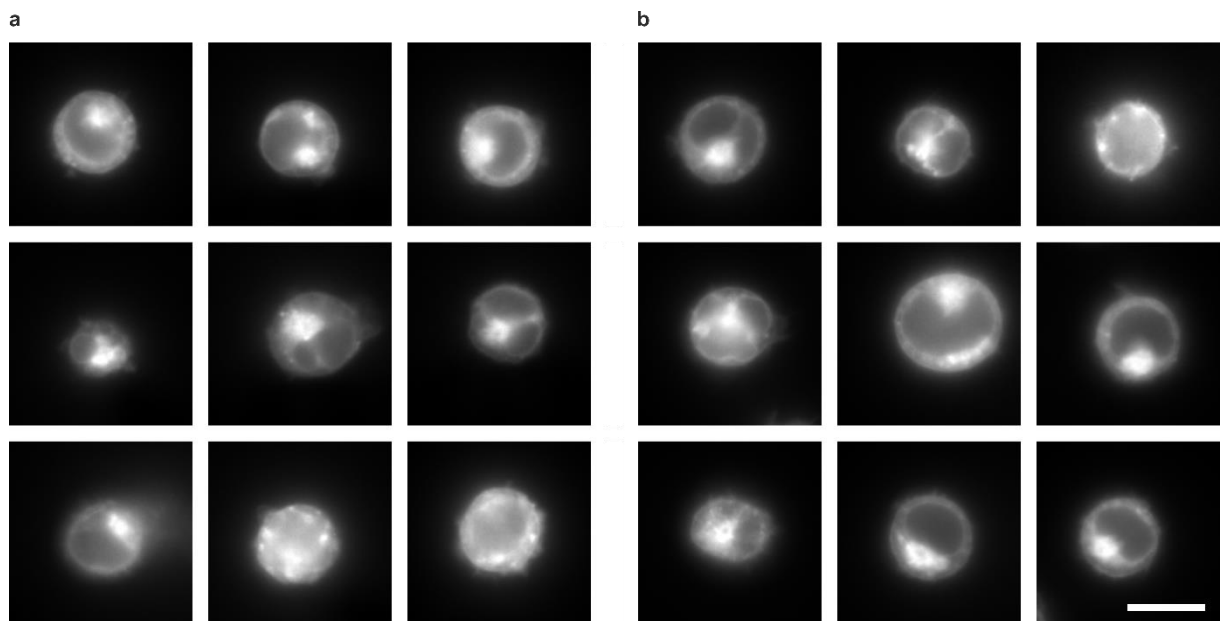
Figure 38: Comparision of micrographs of membrane-stained Jurkat cells. a, Micrographs of the cells flowing (at ca. 500 µm s^{-1}) inside the microfluidic channel. b, Micrographs of the cells on a standard microscope slide. Images were taken with a 40x immersion oil objective and 500 µs exposure time. The scale bar represents 10 µm. In cooperation with Neus Godino.

7   Conclusion

In this work, the possibility of sorting cells image-based using DEP forces was demonstrated. The achieved sorting performance in terms of purity and recovery rate is comparable to other, partly established, systems. However, the high image quality and flexibility of the system are currently achieved at the expense of throughput. Consequently, the achievable throughput is much lower than in other systems, despite precise cell handling and a correspondingly small sorting window. Although the throughput could be increased, the DEP-based sorting will not match the values of an iIACS or an ICS system. The image quality of the developed DEP-based system is superior, but it remains to be seen which advantages will result from this in the long term.

A major advantage of the system is its flexibility with regard to the optical components and the image acquisition method employed, as it is compatible with virtually any microscopic imaging technology. An equally large degree of flexibility is provided with regard to the analysis algorithm used. Due to the low flow velocity and flexible positioning of the image acquisition relative to the sorting array, long iteration times and thus also complex analysis procedures can be implemented.

Based on initial investigations, the biocompatibility of the system can be classified as high since potentially cell-damaging influences of the electric fields could not be found. In fact, due to the low shear forces and gentle cell handling, the system seems particularly suitable for sensitive, rare and valuable cell samples.

In addition to these aspects, the system is characterised by its considerable user friendliness. As it consists of only a few special components, it is also relatively inexpensive compared to complex cell sorting set-ups, even if the microchips used are not disposable.

Although these characteristics set the system apart from the other systems, it is not in direct competition with them. Rather, it represents a complementary approach to image-based cell sorting that covers open niches in existing systems, such as particularly high image quality and exceptionally gentle cell handling.

To further demonstrate its broad applicability, the system could be combined with various other image analysis algorithms and techniques. This would allow the system to evolve from a prototype to a flexible device for image-based cell sorting, significantly lowering the financial barrier and increasing accessibility to image-based cell sorting. In the long term, this could lead to the approach becoming an interesting alternative for smaller laboratories and working groups beyond core facilities.

References

1. Mattanovich, D. & Borth, N. Applications of cell sorting in biotechnology. *Microb Cell Fact* **5**, 12 (2006).
2. Pereira, H. *et al.* Fluorescence activated cell-sorting principles and applications in microalgal biotechnology. *Algal Research* **30**, 113–120 (2018).
3. Gu, Y. *et al.* Machine Learning Based Real-Time Image-Guided Cell Sorting and Classification. *Cytometry* **95**, 499–509 (2019).
4. Brasko, C. *et al.* Intelligent image-based in situ single-cell isolation. *Nat Commun* **9**, 226 (2018).
5. Wyatt Shields IV, C., Reyes, C. D. & López, G. P. Microfluidic cell sorting: a review of the advances in the separation of cells from debulking to rare cell isolation. *Lab on a Chip* **15**, 1230–1249 (2015).
6. Brezinsky, S. C. G. *et al.* A simple method for enriching populations of transfected CHO cells for cells of higher specific productivity. *Journal of Immunological Methods* **277**, 141–155 (2003).
7. Hinterkörner, G. *et al.* Improvement of the energy metabolism of recombinant CHO cells by cell sorting for reduced mitochondrial membrane potential. *Journal of Biotechnology* **129**, 651–657 (2007).
8. Jung, J. *et al.* Label-free non-invasive quantitative measurement of lipid contents in individual microalgal cells using refractive index tomography. *Sci Rep* **8**, 6524 (2018).
9. Wang, Z., Wu, Z., Liu, Y. & Han, W. New development in CAR-T cell therapy. *J Hematol Oncol* **10**, 53 (2017).
10. Levine, B. L., Miskin, J., Wonnacott, K. & Keir, C. Global Manufacturing of CAR T Cell Therapy. *Molecular Therapy - Methods & Clinical Development* **4**, 92–101 (2017).
11. Harouaka, R., Kang, Z., Zheng, S.-Y. & Cao, L. Circulating tumor cells: Advances in isolation and analysis, and challenges for clinical applications. *Pharmacology & Therapeutics* **141**, 209–221 (2014).
12. Stiefel, J. *et al.* Characterization of a novel microfluidic platform for the isolation of rare single cells to enable CTC analysis from head and neck squamous cell carcinoma patients. *Engineering in Life Sciences* **22**, 391–406 (2022).
13. Watanabe, M. *et al.* Multicolor detection of rare tumor cells in blood using a novel flow cytometry-based system: Multicolor Detection System of CTCs. *Cytometry Part A* **85**, 206–213 (2014).
14. Chen, P., Huang, Y.-Y., Hoshino, K. & Zhang, X. Multiscale immunomagnetic enrichment of circulating tumor cells: from tubes to microchips. *Lab Chip* **14**, 446–458 (2014).
15. Jin, C. *et al.* Technologies for label-free separation of circulating tumor cells: from historical foundations to recent developments. *Lab Chip* **14**, 32–44 (2014).
16. Li, P., Stratton, Z. S., Dao, M., Ritz, J. & Huang, T. J. Probing circulating tumor cells in microfluidics. *Lab Chip* **13**, 602 (2013).
17. De Giorgi, V. *et al.* Application of a Filtration- and Isolation-by-Size Technique for the Detection of Circulating Tumor Cells in Cutaneous Melanoma. *Journal of Investigative Dermatology* **130**, 2440–2447 (2010).
18. Dolfus, C., Piton, N., Toure, E. & Sabourin, J.-C. Circulating tumor cell isolation: the assets of filtration methods with polycarbonate track-etched filters. *Chin J Cancer Res* **27**, 9 (2015).
19. Schmitz, B. *et al.* Magnetic activated cell sorting (MACS) - a new immunomagnetic method for megakaryocytic cell isolation: Comparison of different separation techniques. *European Journal of Haematology* **52**, 267–275 (2009).

20. Grützkau, A. & Radbruch, A. Small but mighty: How the MACS®-technology based on nanosized superparamagnetic particles has helped to analyze the immune system within the last 20 years. *Cytometry* **77A**, 643–647 (2010).

21. Miltenyi, S., Müller, W., Weichel, W. & Radbruch, A. High gradient magnetic cell separation with MACS. *Cytometry* **11**, 231–238 (1990).

22. Plouffe, B. D., Murthy, S. K. & Lewis, L. H. Fundamentals and application of magnetic particles in cell isolation and enrichment: a review. *Rep. Prog. Phys.* **78**, 016601 (2015).

23. Zborowski, M. & Chalmers, J. J. Rare Cell Separation and Analysis by Magnetic Sorting. *Analytical Chemistry* **83**, 8050–8056 (2011).

24. Hulett, H. R., Bonner, W. A., Barrett, J. & Herzenberg, L. A. Cell Sorting: Automated Separation of Mammalian Cells as a Function of Intracellular Fluorescence. *Science* **166**, 747–749 (1969).

25. Perfetto, S. P., Chattopadhyay, P. K. & Roederer, M. Seventeen-colour flow cytometry: unravelling the immune system. *Nat Rev Immunol* **4**, 648–655 (2004).

26. Cossarizza, A. *et al.* Guidelines for the use of flow cytometry and cell sorting in immunological studies (second edition). *Eur. J. Immunol.* **49**, 1457–1973 (2019).

27. Moore, M. J., Sebastian, J. A. & Kolios, M. C. Determination of cell nucleus-to-cytoplasmic ratio using imaging flow cytometry and a combined ultrasound and photoacoustic technique: a comparison study. *J. Biomed. Opt.* **24**, 1 (2019).

28. Levsky, J. M. Single-Cell Gene Expression Profiling. *Science* **297**, 836–840 (2002).

29. Altschuler, S. J. & Wu, L. F. Cellular Heterogeneity: Do Differences Make a Difference? *Cell* **141**, 559–563 (2010).

30. Boutros, M., Heigwer, F. & Laufer, C. Microscopy-Based High-Content Screening. *Cell* **163**, 1314–1325 (2015).

31. Moor, A. E. *et al.* Global mRNA polarization regulates translation efficiency in the intestinal epithelium. *Science* **357**, 1299–1303 (2017).

32. Butler, G. S. & Overall, C. M. Proteomic identification of multitasking proteins in unexpected locations complicates drug targeting. *Nat Rev Drug Discov* **8**, 935–948 (2009).

33. von Erlach, T. C. *et al.* Cell-geometry-dependent changes in plasma membrane order direct stem cell signalling and fate. *Nature Mater* **17**, 237–242 (2018).

34. Jaye, D. L., Bray, R. A., Gebel, H. M., Harris, W. A. C. & Waller, E. K. Translational Applications of Flow Cytometry in Clinical Practice. *J.I.* **188**, 4715–4719 (2012).

35. Holzner, G. *et al.* High-throughput multiparametric imaging flow cytometry: toward diffraction-limited sub-cellular detection and monitoring of sub-cellular processes. *Cell Reports* **34**, 108824 (2021).

36. Stubbington, M. J. T., Rozenblatt-Rosen, O., Regev, A. & Teichmann, S. A. Single-cell transcriptomics to explore the immune system in health and disease. *Science* **358**, 58–63 (2017).

37. Chattopadhyay, P. K., Gierahn, T. M., Roederer, M. & Love, J. C. Single-cell technologies for monitoring immune systems. *Nat Immunol* **15**, 128–135 (2014).

38. Zheng, G. X. Y. *et al.* Massively parallel digital transcriptional profiling of single cells. *Nat Commun* **8**, 14049 (2017).

39. Caicedo, J. C. *et al.* Data-analysis strategies for image-based cell profiling. *Nat Methods* **14**, 849–863 (2017).

40. Hu, P., Zhang, W., Xin, H. & Deng, G. Single Cell Isolation and Analysis. *Front. Cell Dev. Biol.* **4**, (2016).

41. Su Lim, C. *et al.* Measurement of the Nucleus Area and Nucleus/Cytoplasm and Mitochondria/Nucleus Ratios in Human Colon Tissues by Dual-Colour Two-Photon Microscopy Imaging. *Sci Rep* **5**, 18521 (2015).

42. Hung, M.-C. & Link, W. Protein localization in disease and therapy. *Journal of Cell Science* **124**, 3381–3392 (2011).

43. Lee, K., Kim, S.-E., Doh, J., Kim, K. & Chung, W. K. User-friendly image-activated microfluidic cell sorting technique using an optimized, fast deep learning algorithm. *Lab Chip* **21**, 1798–1810 (2021).

44. Nitta, N. *et al.* Intelligent Image-Activated Cell Sorting. *Cell* (2018) doi:10.1016/j.cell.2018.08.028.

45. Isozaki, A. *et al.* Intelligent image-activated cell sorting 2.0. *Lab Chip* **20**, 2263–2273 (2020).

46. Nawaz, A. A. *et al.* Intelligent image-based deformation-assisted cell sorting with molecular specificity. *Nat Methods* **17**, 595–599 (2020).

47. Choi, G., Nouri, R., Zarzar, L. & Guan, W. Microfluidic deformability-activated sorting of single particles. *Microsyst Nanoeng* **6**, 11 (2020).

48. Nitta, N. *et al.* Raman image-activated cell sorting. *Nat Commun* **11**, 3452 (2020).

49. Blasi, T. *et al.* Label-free cell cycle analysis for high-throughput imaging flow cytometry. *Nat Commun* **7**, 10256 (2016).

50. Schraivogel, D. *et al.* High-speed fluorescence image–enabled cell sorting. *Science* **375**, 315–320 (2022).

51. LaBelle, C. A., Massaro, A., Cortés-Llanos, B., Sims, C. E. & Allbritton, N. L. Image-Based Live Cell Sorting. *Trends in Biotechnology* **39**, 613–623 (2021).

52. Godino, N. *et al.* Combining dielectrophoresis and computer vision for precise and fully automated single-cell handling and analysis. *Lab Chip* **19**, 4016–4020 (2019).

53. Thomas, R. S. W., Mitchell, P. D., Oreffo, R. O. C., Morgan, H. & Green, N. G. Image-based sorting and negative dielectrophoresis for high purity cell and particle separation. *ELECTROPHORESIS* **00**, 1–10 (2019).

54. Lee, D., Hwang, B. & Kim, B. The potential of a dielectrophoresis activated cell sorter (DACS) as a next generation cell sorter. *Micro and Nano Syst Lett* **4**, 2 (2016).

55. Schnelle, T., Müller, T., Gradl, G., Shirley, S. G. & Fuhr, G. Paired microelectrode system: dielectrophoretic particle sorting and force calibration. *Journal of Electrostatics* **47**, 121–132 (1999).

56. Duschl, C. *et al.* Versatile chip-based tool for the controlled manipulation of microparticles in biology using high Frequency Electromagnetic Fields. in *Lab-on-Chips for Cellomics* 83–122 (Springer, 2004).

57. Dharmasiri, U., Witek, M. A., Adams, A. A. & Soper, S. A. Microsystems for the Capture of Low-Abundance Cells. *Annual Rev. Anal. Chem.* **3**, 409–431 (2010).

58. Cai, L., Friedman, N. & Xie, X. S. Stochastic protein expression in individual cells at the single molecule level. *Nature* **440**, 358–362 (2006).

59. Taniguchi, K., Kajiyama, T. & Kambara, H. Quantitative analysis of gene expression in a single cell by qPCR. *Nat Methods* **6**, 503–506 (2009).

60. Corrsin, S. Turbulent Flow. *American Scientist* **49**, 300–325 (1961).

61. Mathieu, J. & Scott, J. *An introduction to turbulent flow*. (Cambridge University Press, 2000).

62. Squires, T. M. & Quake, S. R. Microfluidics: Fluid physics at the nanoliter scale. *Rev. Mod. Phys.* **77**, 977–1026 (2005).

63. Bruus, H. Acoustofluidics 1: Governing equations in microfluidics. *Lab Chip* **11**, 3742 (2011).

64. Spiga, M. & Morino, G. L. A symmetric solution for velocity profile in laminar flow through rectangular ducts. *International Communications in Heat and Mass Transfer* **21**, 469–475 (1994).

65. Stigler, J. Analytical velocity profile in tube for laminar and turbulent flow. *Engineering Mechanics* **21**, 371–379 (2014).

66. Cengel, Y. & Cimbala, J. *Fluid Mechanics Fundamentals and Applications (SI units)*. (McGraw-Hill Education, 2013).

67. Amini, H., Lee, W. & Di Carlo, D. Inertial microfluidic physics. *Lab on a Chip* **14**, 2739–2761 (2014).

68. Tanyeri, M., Ranka, M., Sittipolkul, N. & Schroeder, C. M. A microfluidic-based hydrodynamic trap: Design and implementation. 7 (2011).

69. Beebe, D. J., Mensing, G. A. & Walker, G. M. Physics and Applications of Microfluidics in Biology. *Annu. Rev. Biomed. Eng.* **4**, 261–286 (2002).

70. Rotta, J. Experimenteller Beitrag zur Entstehung turbulenter Strömung im Rohr. *Ingenieur-Archiv* **24**, 258–281 (1956).

71. Chen, P. Microfluidic chips for cell sorting. *Front Biosci* **13**, 2464 (2008).

72. Zhao, Y., Li, Q. & Hu, X. Universally applicable three-dimensional hydrodynamic focusing in a single-layer channel for single cell analysis. *Anal. Methods* **10**, 3489–3497 (2018).

73. Martel, J. M. & Toner, M. Inertial Focusing in Microfluidics. *Annu. Rev. Biomed. Eng.* **16**, 371–396 (2014).

74. Liu, C., Hu, G., Jiang, X. & Sun, J. Inertial focusing of spherical particles in rectangular microchannels over a wide range of Reynolds numbers. *Lab Chip* **15**, 1168–1177 (2015).

75. Matas, Jp., Morris, Jf. & Guazzelli, E. Lateral Forces on a Sphere. *Oil & Gas Science and Technology - Rev. IFP* **59**, 59–70 (2004).

76. Saffman, P. G. The lift on a small sphere in a slow shear flow. *J. Fluid Mech.* **22**, 385–400 (1965).

77. Zhang, J. *et al.* Fundamentals and applications of inertial microfluidics: a review. *Lab on a Chip* **16**, 10–34 (2016).

78. Ryan, K., Rose, R. E., Jones, D. R. & Lopez, P. A. Sheath fluid impacts the depletion of cellular metabolites in cells afflicted by sorting induced cellular stress (SICS). *Cytometry* **99**, 921–929 (2021).

79. Pohl, H. A. The Motion and Precipitation of Suspensoids in Divergent Electric Fields. *Journal of Applied Physics* **22**, 869–871 (1951).

80. Pohl, H. A., Pollock, K. & Crane, J. S. Dielectrophoretic force: A comparison of theory and experiment. *J Biol Phys* **6**, 133–160 (1978).

81. Müller, T. *et al.* The potential of dielectrophoresis for single-cell experiments. *IEEE Eng. Med. Biol. Mag.* **22**, 51–61 (2003).

82. Schnelle, T., Müller, T., Fiedler, S. & Fuhr, G. The influence of higher moments on particle behaviour in dielectrophoretic field cages. *Journal of Electrostatics* **46**, 13–28 (1999).

83. Jäger, M. Über die Manipulation biogener und artifizieller Mikro- und Nanoobjekte in Mikroelektrodensystemen. (2005).

84. Gimsa, J., Marszalek, P., Loewe, U. & Tsong, T. Y. Dielectrophoresis and electrorotation of neurospora slime and murine myeloma cells. *Biophysical Journal* **60**, 749–760 (1991).

85. Pethig, R. Review Article—Dielectrophoresis: Status of the theory, technology, and applications. *Biomicrofluidics* **4**, 022811 (2010).

86. Voldman, J. Electrical forces for microscale cell manipulation. *Annu. Rev. Biomed. Eng.* **8**, 425–454 (2006).

87. Čemažar, J., Miklavčič, D. & Kotnik, T. Microfluidic devices for manipulation, modification and characterization of biological cells in electric fields – a review. **43**, 20 (2013).

88. Jäger, M. S., Uhlig, K., Schnelle, T. & Müller, T. Contact-free single-cell cultivation by negative dielectrophoresis. *J. Phys. D: Appl. Phys.* **41**, 175502 (2008).

89. Glasser, H. & Fuhr, G. Cultivation of cells under strong ac-electric field—differentiation between heating and trans-membrane potential effects. *Bioelectrochemistry and Bioenergetics* **47**, 301–310 (1998).

90. Kirschbaum, M. A microfluidic approach for the initiation and investigation of surface-mediated signal transduction processes on a single-cell level. (Universität Potsdam, 2009).

91. Kentsch, J. *et al.* Microdevices for separation, accumulation, and analysis of biological micro- and nanoparticles. *IEE Proc., Nanobiotechnol.* **150**, 82 (2003).

92. Cheng, I.-F., Chang, H.-C., Hou, D. & Chang, H.-C. An integrated dielectrophoretic chip for continuous bioparticle filtering, focusing, sorting, trapping, and detecting. *Biomicrofluidics* **1**, 021503 (2007).

93. Müller, T., Schnelle, T., Gradl, G., Shirley, S. G. & Fuhr, G. Microdevice for cell and particle separation usind dielectrophoretic field-flow fractionation. *Journal of Liquid Chromatography & Related Technologies* **23**, 47–59 (2000).

94. Fiedler, S., Shirley, S. G., Schnelle, T. & Fuhr, G. Dielectrophoretic sorting of particles and cells in a microsystem. *Analytical chemistry* **70**, 1909–1915 (1998).

95. Bezanilla, F. How membrane proteins sense voltage. *Nature Reviews Molecular Cell Biology* **9**, 323–332 (2008).

96. Maswiwat, K., Wachner, D. & Gimsa, J. Effects of cell orientation and electric field frequency on the transmembrane potential induced in ellipsoidal cells. *Bioelectrochemistry* **74**, 130–141 (2008).

97. Pakhomova, O. N., Gregory, B. W., Semenov, I. & Pakhomov, A. G. Two Modes of Cell Death Caused by Exposure to Nanosecond Pulsed Electric Field. *PLoS ONE* **8**, e70278 (2013).

98. Blank, M. & Goodman, R. Electromagnetic fields stress living cells. *Pathophysiology* **16**, 71–78 (2009).

99. Winslow, M. M. & Crabtree, G. R. Decoding Calcium Signaling. *Science* **307**, 56–57 (2005).

100. Glaser, R. *Biophysics*. (Springer Berlin Heidelberg, 2012). doi:10.1007/978-3-642-25212-9.

101. Maschio, M. dal, Canato, M. & Pigozzo, F. M. Biophysical effects of high frequency electrical field (4-64 MHz) on muscle fibers in culture. in (2008).

102. Gehl, J. Electroporation: theory and methods, perspectives for drug delivery, gene therapy and research. *Acta Physiologica Scandinavica* **177**, 437–447 (2003).

103. Chen, C., Smye, S. W., Robinson, M. P. & Evans, J. A. Membrane electroporation theories: a review. *Med Bio Eng Comput* **44**, 5–14 (2006).

104. De Maio, A. Heat shock proteins: facts, thoughts, and dreams. *Shock* **11**, 1–12 (1999).

105. Lindquist, S. The heat-shock response. *Annu Rev Biochem* **55**, 1151–1191 (1986).

106. Pegg, D. E. Viability assays for preserved cells, tissues, and organs. *Cryobiology* **26**, 212–231 (1989).

107. Louis, K. S. & Siegel, A. C. Cell Viability Analysis Using Trypan Blue: Manual and Automated Methods. in *Mammalian Cell Viability: Methods and Protocols* (ed. Stoddart, M. J.) (Humana Press, 2011). doi:10.1007/978-1-61779-108-6_2.

108. Absher, M. Chapter 1 - Hemocytometer Counting. in *Tissue Culture* (eds. KRUSE, P. F. & PATTERSON, M. K.) 395–397 (Academic Press, 1973). doi:10.1016/B978-0-12-427150-0.50098-X.

109. Stoddart, M. J. Cell Viability Assays: Introduction. in *Mammalian Cell Viability: Methods and Protocols* (ed. Stoddart, M. J.) (Humana Press, 2011). doi:10.1007/978-1-61779-108-6_1.

110. Kamiloglu, S., Sari, G., Ozdal, T. & Capanoglu, E. Guidelines for cell viability assays. *Food Frontiers* **1**, 332–349 (2020).

111. Aslantürk, Ö. S. In Vitro Cytotoxicity and Cell Viability Assays: Principles, Advantages, and Disadvantages. in *Genotoxicity - A Predictable Risk to Our Actual World* (eds. Larramendy, M. L. & Soloneski, S.) (InTech, 2018). doi:10.5772/intechopen.71923.

112. Agteresch, H. J., Dagnelie, P. C., van den Berg, J. W. & Wilson, J. H. Adenosine Triphosphate: Established and Potential Clinical Applications. *Drugs* **58**, 211–232 (1999).

113. Lundin, A. Use of firefly luciferase in atp-related assays of biomass, enzymes, and metabolites. in *Methods in Enzymology* vol. 305 346–370 (Academic Press, 2000).

114. Präbst, K., Engelhardt, H., Ringgeler, S. & Hübner, H. Basic Colorimetric Proliferation Assays: MTT, WST, and Resazurin. in *Cell Viability Assays: Methods and Protocols* (eds. Gilbert, D. F. & Friedrich, O.) 1–17 (Springer New York, 2017). doi:10.1007/978-1-4939-6960-9_1.

115. Stockert, J. C., Horobin, R. W., Colombo, L. L. & Blázquez-Castro, A. Tetrazolium salts and formazan products in Cell Biology: Viability assessment, fluorescence imaging, and labeling perspectives. *Acta Histochemica* **120**, 159–167 (2018).

116. van Tonder, A., Joubert, A. M. & Cromarty, A. D. Limitations of the 3-(4,5-dimethylthiazol-2-yl)-2,5-diphenyl-2H-tetrazolium bromide (MTT) assay when compared to three commonly used cell enumeration assays. *BMC Res Notes* **8**, 47 (2015).

117. Ishiyama, M. A highly water-soluble disulfonated tetrazolium salt as a chromogenic indicator for NADH as well as cell viability. *Talanta* **44**, 1299–1305 (1997).

118. Tominaga, H. *et al.* A water-soluble tetrazolium salt useful for colorimetric cell viability assay. *Anal. Commun.* **36**, 47–50 (1999).

119. Witek, M. A., Freed, I. M. & Soper, S. A. Cell Separations and Sorting. *Anal. Chem.* **92**, 105–131 (2020).

120. Ashcroft, R. G. & Lopez, P. A. Commercial high speed machines open new opportunities in high throughput flow cytometry (HTFC). *Journal of Immunological Methods* **243**, 13–24 (2000).

121. Herbig, M. *et al.* Best practices for reporting throughput in biomedical research. *Nat Methods* **19**, 633–634 (2022).

122. Collins, D. J., Neild, A., deMello, A., Liu, A.-Q. & Ai, Y. The Poisson distribution and beyond: methods for microfluidic droplet production and single cell encapsulation. *Lab Chip* **15**, 3439–3459 (2015).

123. Brakke, M. K. Density Gradient Centrifugation: A New Separation Technique. *J. Am. Chem. Soc.* **73**, 1847–1848 (1951).

124. Gertler, R. *et al.* Detection of Circulating Tumor Cells in Blood Using an Optimized Density Gradient Centrifugation. in *Molecular Staging of Cancer* (eds. Allgayer, H., Heiss, M. M. & Schildberg, F. W.) 149–155 (Springer Berlin Heidelberg, 2003).

125. Timonen, T. & Saksela, E. Isolation of human NK cells by density gradient centrifugation. *Journal of Immunological Methods* **36**, 285–291 (1980).

126. Wortham, S. T., Ortolano, G. A. & Wenz, B. A brief history of blood filtration: clot screens, microaggregate removal, and leukocyte reduction. *Transfusion Medicine Reviews* **17**, 216–222 (2003).

127. Dzik, S. Leukodepletion Blood Filters: Filter Design and Mechanisms of Leukocyte Removal. *Transfusion Medicine Reviews* **7**, 65–77 (1993).

128. Park, J.-S., Song, S.-H. & Jung, H.-I. Continuous focusing of microparticles using inertial lift force and vorticity via multi-orifice microfluidic channels. *Lab Chip* **9**, 939–948 (2009).

129. Yun, H., Kim, K. & Lee, W. G. Cell manipulation in microfluidics. *Biofabrication* **5**, 022001 (2013).

130. Beech, J. P., Holm, S. H., Adolfsson, K. & Tegenfeldt, J. O. Sorting cells by size, shape and deformability. *Lab Chip* **12**, 1048 (2012).

131. Huang, L. R., Cox, E. C., Austin, R. H. & Sturm, J. C. Continuous Particle Separation Through Deterministic Lateral Displacement. *Science* **304**, 987–990 (2004).

132. Goddard, G., Martin, J. C., Graves, S. W. & Kaduchak, G. Ultrasonic particle-concentration for sheathless focusing of particles for analysis in a flow cytometer. *Cytometry* **69A**, 66–74 (2006).

133. Lin, S.-C. S., Mao, X. & Huang, T. J. Surface acoustic wave (SAW) acoustophoresis: now and beyond. *Lab Chip* **12**, 2766 (2012).

134. Yasukawa, T., Suzuki, M., Shiku, H. & Matsue, T. Control of the microparticle position in the channel based on dielectrophoresis. *Sensors and Actuators B: Chemical* **142**, 400–403 (2009).

135. Čemažar, J., Vrtačnik, D., Amon, S. & Kotnik, T. Dielectrophoretic Field-Flow Microchamber for Separation of Biological Cells Based on Their Electrical Properties. *IEEE Transactions on NanoBioscience* **10**, 36–43 (2011).

136. Gascoyne, P. R. C., Noshari, J., Anderson, T. J. & Becker, F. F. Isolation of rare cells from cell mixtures by dielectrophoresis. *ELECTROPHORESIS* **30**, 1388–1398 (2009).

137. Song, H. *et al.* Continuous-flow sorting of stem cells and differentiation products based on dielectrophoresis. *Lab Chip* **15**, 1320–1328 (2015).

138. Baret, J.-C. *et al.* Fluorescence-activated droplet sorting (FADS): efficient microfluidic cell sorting based on enzymatic activity. *Lab Chip* **9**, 1850 (2009).

139. Loo, M. H., Nakagawa, Y., Kim, S. H., Isozaki, A. & Goda, K. High-throughput sorting of nanoliter droplets enabled by a sequentially addressable dielectrophoretic array. *Electrophoresis* **43**, 477–486 (2022).

140. Franke, T., Braunmüller, S., Schmid, L., Wixforth, A. & Weitz, D. A. Surface acoustic wave actuated cell sorting (SAWACS). *Lab Chip* **10**, 789 (2010).

141. Wang, M. M. *et al.* Microfluidic sorting of mammalian cells by optical force switching. *Nat Biotechnol* **23**, 83–87 (2005).

142. Wang, X. *et al.* Enhanced cell sorting and manipulation with combined optical tweezer and microfluidic chip technologies. *Lab Chip* **11**, 3656 (2011).

143. Adan, A., Alizada, G., Kiraz, Y., Baran, Y. & Nalbant, A. Flow cytometry: basic principles and applications. *Critical Reviews in Biotechnology* **37**, 163–176 (2017).

144. Ravi, D. *et al.* Deep Learning for Health Informatics. *IEEE J. Biomed. Health Inform.* **21**, 4–21 (2017).

145. Mikami, H. *et al.* Virtual-freezing fluorescence imaging flow cytometry. *Nat Commun* **11**, 1162 (2020).

146. Diebold, E. D., Buckley, B. W., Gossett, D. R. & Jalali, B. Digitally synthesized beat frequency multiplexing for sub-millisecond fluorescence microscopy. *Nature Photonics* **7**, 806–810 (2013).

147. Dürr, M., Kentsch, J., Müller, T., Schnelle, T. & Stelzle, M. Microdevices for manipulation and accumulation of micro- and nanoparticles by dielectrophoresis. (2003).

148. Dudaie, M. *et al.* Label-free discrimination and selection of cancer cells from blood during flow using holography-induced dielectrophoresis. *J. Biophotonics* **13**, (2020).

149. Isozaki, A. *et al.* Sequentially addressable dielectrophoretic array for high-throughput sorting of large-volume biological compartments. *Sci. Adv.* **6**, eaba6712 (2020).

150. Fu, A. Y., Spence, C., Scherer, A., Arnold, F. H. & Quake, S. R. A microfabricated fluorescence-activated cell sorter. *Nat Biotechnol* **17**, 1109–1111 (1999).

151. Dittrich, P. S. & Schwille, P. An Integrated Microfluidic System for Reaction, High-Sensitivity Detection, and Sorting of Fluorescent Cells and Particles. *Anal. Chem.* **75**, 5767–5774 (2003).

152. Zhu, L. *et al.* Cell loss in integrated microfluidic device. *Biomed Microdevices* **9**, 745–750 (2007).

153. Paiè, P., Bragheri, F., Bassi, A. & Osellame, R. Selective plane illumination microscopy on a chip. *Lab Chip* **16**, 1556–1560 (2016).

154. Deschout, H. *et al.* On-chip light sheet illumination enables diagnostic size and concentration measurements of membrane vesicles in biofluids. *Nanoscale* **6**, 1741–1747 (2014).

155. Amann, R., Fuchs, B. M. & Behrens, S. The identification of microorganisms by fluorescence in situ hybridisation. *Current Opinion in Biotechnology* **12**, 231–236 (2001).

156. Zwirglmaier, K. Fluorescence in situ hybridisation (FISH) – the next generation. *FEMS Microbiology Letters* **246**, 151–158 (2005).

157. Kortmann, H., Blank, L. M. & Schmid, A. A rapid, reliable, and automatable lab-on-a-chip interface. *Lab on a Chip* **9**, 1455 (2009).

158. Fritzsch, F. S. O., Kortmann, H., Lonzynski, J., Blank, L. M. & Schmid, A. Pressure-resistant and reversible on-tube-sealing for microfluidics. *Microfluidics and Nanofluidics* **10**, 679–684 (2011).

159. Morbioli, G. G., Speller, N. C. & Stockton, A. M. A practical guide to rapid-prototyping of PDMS-based microfluidic devices: A tutorial. *Analytica Chimica Acta* **1135**, 150–174 (2020).

160. Ongaro, A. E. *et al.* Engineering a sustainable future for point-of-care diagnostics and single-use microfluidic devices. *Lab Chip* **22**, 3122–3137 (2022).

List of materials and devices

Hardware

Microscopy setup I (Sorting)

Microscope	IX71	Olympus, Germany
CMOS camera	edge 5.5	PCO, Germany
Mercury vapour lamp	USH-103D	Ushio, USA
4x air objective	UPlanFL 4x	Olympus, Germany
60x oil immersion objective	PlanApo N 60x Oil	Olympus, Germany
Filter cubes	F56-024	AHF, Germany
	MWIG2	Olympus, Germany
Computer	T3610	Dell Technologies, USA
GPU	Quadro P400	Nvidia, USA

Microscopy setup 2 (preliminary experiments)

Microscope	IX71	Olympus, Germany
CCD camera	ORCA-ER	Hamamatsu, Japan
Mercury vapour lamp	USH-103D	Ushio, USA
10x air objective	UPlanFL N 10x	Olympus, Germany
20x air objective	UplanFL N 20x	Olympus, Germany
Filter cube	Olympus MWIG2	Olympus, Germany
Computer	CELSIUS W580power	Fujitsu, Japan

Microscopy setup 3 (automated live cell imaging system)

Microscope	IXplore Live	Olympus, Germany
CMOS camera	ORCA-Flash 4.0	Hamamatsu, Japan
Light source	Spectra X	Lumencor, USA
4x air objective	UplanFL N 4x	Olympus, Germany
Filter cubes	F66-031_OE, F66-040_OE	AHF, Germany
Computer	Z4 G4	HP, USA

Hardware (continued)

DEP Chips	CeProm Series	GeSiM, Germany
	DFC Series	GeSiM, Germany
	In-house Series	Fraunhofer IZI-BB
FEP-Tubing	1527	IDEX, USA
PEEK-Tubing	1561, 1576	IDEX, USA
Microfluidic accessories	XP-230x, XP-286x, XP-200x, F-247, A-327	IDEX, USA
Microfluidic Pumps	NemeSYS series	Cetoni, Germany
	SP 230IWZ	WPI, USA
	FlowEZ series	Fluigent, Germany
	Flow sensors S & M	Fluigent, Germany
Syringes	3010236, 3010235, 3010177	SETonic, Germany
DEP-Signal Generators	proprietary development	AK Moduls-Bus, Germany
Ultrasonic bath	Sonorex Super 10 P	Bandelin, Germany
Centrifuges	Multifuge 3 S-R	Heraeus, Germany
	5415 D	Eppendorf, Germany
Photometer	EnVision 2105	Perkin Elmer, USA
Ultrapure water system	arium® pro VF TOC	Sartorius, Germany
Plasma cleaner	PDC-002	Harrick, USA
Metal evaporation system	Auto 500	BOC Edwards, UK
Spin coater	EL S 200 TT	solar-semi, Germany
Hotplate	QS H 200 TT	solar-semi, Germany
Laser exposer	µPG 101	Heidelberg, Germany
Cutting plotter	Craft ROBO Pro	Graphtec, Japan
Drill	MF 70	Proxxon, Germany
Milling machine	M8Cube	Datron, Germany
UV lamp	Bluepoint LED	Hönle, Germany

Cell Culture

Jurkat T-cells	clone E6-1	ATCC, USA
RPMI 1640	P04-18000	PAN-Biotech, Germany
Fetal bovine serum	P30-3031	PAN-Biotech, Germany
L-glutamine	P04-82100	PAN-Biotech, Germany
Penicillin-streptomycin	P06-07100	PAN-Biotech, Germany
Sodium pyruvate	L0642-100	Biowest, France

Consumables

Cell culture flasks	83.3910.002	Sarstedt, Germany
	83.3911.002	Sarstedt, Germany
96-well plates	83.3924500	Sarstedt, Germany
Cell counting slides	L12001	Logos, South Korea
Centrifuge tubes	62.554.502	Sarstedt, Germany
	62.547.254	Sarstedt, Germany
	S1615-5550	Starlab, Germany
Microscope slides	2947-75x38, 2947-75x75	Corning, USA
Chromium 99,98%	009541	ChemPur, Germany
Gold 99,99%	10000025	ESG, Germany
Photoresist	AZ 1514 H	Microchemicals, Germany
Developer	AZ 400 K	Microchemicals, Germany
Chromium Etch	TechniEtch Cr01	Technic, France
Gold Etch	TechniEtch ACl2	Technic, France
Biocompatible Adhesive	9965	3M, USA
	ArCare 92712	Adhesives Research, USA
Angled pin bar	000733919-81	Conrad, Germany
Silver conductive paint	000241319-81	Conrad, Germany
UV adhesive	Vitralit 4731	Panacol-Elosol, Germany

Other

Fluorescent dyes

Calcein red-orange	C34851	ThermoFisher, USA
Calcein AM	C3100MP	ThermoFisher, USA
Nuc-Blue	R37605	ThermoFisher, USA
Octadecyl-rhodamine	O246	ThermoFisher, USA
Dimehyl sulfoxide	D8418-100ML	Sigma-Aldrich, USA
Nycodenz	31000.01	Serva, Germany
WST-8 cell proliferation kit	CK04	Dojindo, Japan
Cleaning reagent	Hellmanex III	Hellma, Germany
Ethanol	1.11727.2500	Merck, Germany

Software

Windows 10	Microsoft, USA
All-in-One microfluidic flow control	Fluigent, Germany
Python	PSF, USA
Matlab	MathWorks, USA
Excel	Microsoft, USA
Word	Microsoft, USA
ImageJ	NIH, USA
OriginPro	OriginLab, USA
CorelDRAW	Corel, Canada
HCImage	Hamamatsu, Japan

List of figures

List of tables

List of abbreviations

20x	20-fold
40x	40-fold
60x	60-fold
2D	two-dimensional
A	cross-sectional area
AOD	acousto-optic deflector
ATP	adenosine 5'-triphosphate
CAD	computer-aided design
CAR	chimeric antigen receptor
CCD	charge-coupled device
CMOS	complementary metal-oxide-semiconductor
CTC	circulating tumor cell
d	characteristic channel length
DEP	dielectrophoresis
DLD	deterministic lateral displacement
DMSO	Dimethyl sulfoxide
e	Euler's number
E1-E5	electrode numbers of the PROC2 microchip
FACS	Fluorescence activated cell sorting
F_B	buoyancy force
f_{CM}	Clausius-Mossotti factor
FEP	fluorinated ethylene propylene
F_{DEP}	dielectrophoretic force
F_{DRAG}	hydrodynamic drag force
F_G	gravitational force
FIRE	Fluorescence imaging using radiofrequency-tagged emission
FISH	fluorescence in situ hybridisation
FSC	forward scattered light
GPU	graphics processing unit
h	linear distance from the channel centre
H	½ channel height
ICS	Image-enabled cell sorter
ID	inner diameter, identification number
iIACS	Intelligent image-activated cell sorting
k	number of cells located within the sorting window
L	perimeter
MACS	Magnetic activated cell sorting
NA	numerical aperture
NADPH	nicotinamide adenine dinucleotide phosphate
OD	outer diameter
P	probability
PCB	printed circuit board
PD	photodiode
PDMS	Polydimethylsiloxane

PEEK	Polyether ether ketone
PMMA	Poly(methyl methacrylate)
PMT	photomultiplier tube
PSA	pressure sensitive adhesive
PTFE	Polytetrafluoroethylene
q	dipole moment
r	radial distance from the channel centre, particle radius
R	radius
R18	Octadecyl-rhodamine
Re	Reynolds number
ROI	region of interest
SAW	standing acoustic wave
SAWACS	Surface acoustic wave actuated cell sorting
SSC	side scattered light
UV	ultraviolet
v	flow velocity
v_{av}	average flow velocity
v_{max}	maximum flow velocity
WBC	white blood cell
WST-8	2-(2-methoxy-4-nitrophenyl)-3-(4-nitrophenyl)-5-(2,4-disulfophenyl)-2H tetrazolium, mono-sodium salt
α	electrode angle (relative to the channel wall)
ε_0	dielectric natural constant
ε_M	permittivity (medium)
ε_P	permittivity (particle)
η	dynamic viscosity
μ	mean expected number of cells in the sorting window
ν	kinematic viscosity
ρ	fluid density
σ_M	electric conductivity (medium)
σ_P	electric conductivity (particle)
∇E	electric field gradient

Appendix

Estimation of the achievable purity based on Poisson statistics

A critical feature for the performance of any cell sorting method is the achievable purity of the sorting result and the yield of target cells as a function of sample throughput. In microfluidic sorting, where cells are driven through a microchannel in a pearl chain configuration and are deflected vertical to the flow direction over a certain distance (i.e.,, the sorting window) in course of their selection, the performance is closely related to the effective length of this window. In an ideal system, the target and non-target cells that pass through the channel are totally uncorrelated and thus their occurrence in the sorting window follows a Poisson distribution with k the number of occurrences and μ the mean expected number of cells in the sorting window at any given time.

$$P_\mu(k) = \frac{\mu^k}{k!} e^{-\mu} \tag{A1}$$

Accordingly, it cannot be ruled out that multiple cells appear in the sorting window at the same time (e.g., a target and a non-target cell), which cannot be processed independently of each other.

In terms of purity and yield, this problem can be addressed in two ways. Either discard both cells to maximise the purity of the sorting result at the expense of yield ("purity sort"), or sort the target cell together with the non-target cell according to the opposite motivation ("yield sort"). In case of a "yield sort", where all target cells are sorted independently of the neighbouring non-target cells, the theoretical yield is by definition 100 %.[26]

The purity p achieved at a given throughput can now be used to characterise the performance of the system. It is calculated from the ratio of target cells (N_T) to the total number of target and non-target (N_{nT}) cells sorted out.

$$p = \frac{N_T}{N_T + N_{nT}} \tag{A2}$$

Let x be the percentage of target cells in the sample. Then the mean expected number of target (μ_T) and non-target cells (μ_{nT}) in the sorting window at any given time point calculates to $x\mu$ and $(1-x)\mu$, respectively. Accordingly, each time a target cell is sorted in the sorting window, on average there are also μ_{nT} non-target cells in the sorting window, which are sorted out together with the target cell. According to this, the purity of the sorting result calculates to

$$p = \frac{N_T}{N_T + N_{sort} * \mu_{nT}} \tag{A3}$$

with N_{sort} = total number of sorting events necessary for sorting N_T target cells. It is important to note that fewer than N_T sorting events are required to sort out N_T target cells from the sample, as more than one target cell appear in the sorting window in certain cases due to the Poisson statistics described above. As can be easily seen, this value is a function of the expected number of target cells in the sorting window μ_T.

In a stochastic sorting procedure, one would expect N_T target cells after N_T/μ_T sorting operations. In a reactive, targeted sorting procedure, however, a sorting process is only triggered if there is actually at least one target cell in the sorting window, hence

$$N_{sort} = \frac{N_T}{\mu_T}\left(1 - P_{\mu_T}(0)\right) \tag{A4}$$

$$= \frac{N_T}{\mu_T}(1 - e^{-\mu_T}) \tag{A5}$$

The purity p of the sorted cell fraction is therefore

$$p = \frac{N_T}{N_T + \frac{N_T}{\mu_T}(1 - e^{-\mu_T})\,\mu_{nT}} \tag{A6}$$

Since $\mu_T = x\mu$ and $\mu_{nT} = (1-x)\mu$, the purity can be expressed as

$$p = \frac{1}{1 + \frac{(1-x)}{x}(1 - e^{-x\mu})} \tag{A7}$$

Moreover, μ can be expressed as the ratio between the width of the sorting window d and the average cell distance, while the average cell distance in turn is the ratio of mean velocity of the cells v and throughput θ. For a given x, d and v (here: 580 µm s^{-1}) the maximum achievable purity of a yield sort can be expressed as a function of θ (see Figure A1):

$$p = \frac{1}{1 + \frac{(1-x)}{x}\left(1 - e^{-\frac{xd\theta}{v}}\right)} \tag{A8}$$
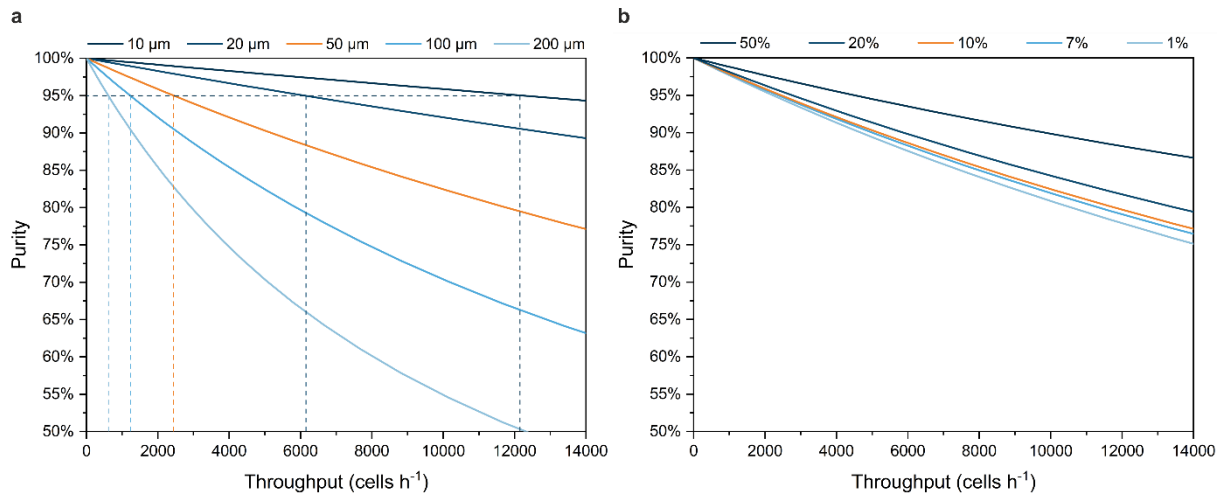
Figure A1: Maximum achievable purity of a yield sort at a mean cell velocity of 580 µm s^{-1} and either (**a**) constant target cell concentration of 10% and variable sorting window width or (**b**) constant window width of 50 µm and variable target cell concentration. While the width of the sorting window has a significant impact on the achievable purity or throughput of a sorting process, the target cell concentration in the lower range of up to 20 % is of rather minor importance. Conditions reflecting the experimental situation in this work are marked in orange.

Lebenslauf

PERSÖNLICHE DATEN

Name	Marten Tobias Gerling
Geburtsdatum	21. September 1992
Geburtsort	Düsseldorf
Staatsangehörigkeit	deutsch

AUSBILDUNG

2018	Beginn der Promotionsarbeit im Bereich Bioanalytik Universität Potsdam / Fraunhofer Institut für Zelltherapie und Immunologie, Institutsteil Bioanalytik und Bioprozesse IZI-BB, Potsdam Titel der Arbeit: *A Microfluidic System for High-Precision Image-Based Live Cell Sorting Using Dielectrophoretic Forces*
2015 – 2017	Master of Science in Nanowissenschaften Universität Hamburg, Hamburg Titel der Abschlussarbeit: *Kapton®-based Microfluidic Continuous-flow Devices for Temperature-controlled Nanoparticle Studies via Time-resolved X-ray Scattering*
2011 – 2015	Bachelor of Science in Nanowissenschaften Universität Hamburg, Hamburg Titel der Abschlussarbeit: *Shape controlled Synthesis of TiO_2- and TiO_2-SiO_2 Core-Shell Nanoparticles*
2011	Abitur Gymnasium am Heimgarten, Ahrensburg

BESCHÄFTIGUNGSVERHÄLTNISSE

seit 2018	Wissenschaftlicher Mitarbeiter am Fraunhofer Institut für Zelltherapie und Immunologie, Institutsteil Bioanalytik und Bioprozesse IZI-BB, Potsdam

Publikationen und Patente

PUBLIKATIONEN

T. Gerling, N. Godino, F. Pfisterer, N. Hupf and M. Kirschbaum: *High-precision, high-quality microscopy-based live-cell sorting*, submitted 2022

M. Dudaie, N. Nissim, I. Barnea, T. Gerling, C. Duschl, M. Kirschbaum and N. T. Shaked: *Label-free discrimination and selection of cancer cells from blood during flow using holography-induced dielectrophoresis*, J. Biophotonics, 2020, 13:e202000151

N. Godino, F. Pfisterer, T. Gerling, C. Guernth-Marschner, C. Duschl and M. Kirschbaum: *Combining dielectrophoresis and computer vision for precise and fully automated single-cell handling and analysis*, Lab Chip, 2019, 19, 4016-4020

PATENTE

M. Kirschbaum, T. Gerling and N. Godino: *Method and fluidic system for the dielectrophoretic manipulation of suspended particles*, Patent Nr. WO 2022/029036

N. T. Shaked, I. Barnea, M. Dudaie, N. Nissim, M. Kirschbaum and T. Gerling: *A system and method thereof for real-time automatic label-free-holography-activated sorting of cells*, Patent Nr. WO 2022/018730

Danksagung